The Aetiology of Mesothelioma: Morphological and Chemical Analyses of Asbestos Ferruginous Bodies

Avramescu Maya-Liliana

Doctoral Thesis

Department of Analytical Planetary Chemistry

Okayama University

Abstract

Asbestos is a fibrous silicate material widely used in many industries in the past, such as shipbuilding and insulation, due to its favourable characteristics. However, it was extensively banned in the 1990s due to causing an aggressive type of cancer known as malignant mesothelioma (MM). The main physical features associated with MM are asbestos fibres coated with a Fe-rich material mainly composed of ferrihydrite (Fh), the final product being termed "asbestos ferruginous bodies" (AFB). Despite the asbestos ban, MM has a long latency period (20-40 yrs.) which will lead to high mortality rates by 2025. As of today, the processes governing the formation of AFBs and the role they play in MM are not well understood. In particular, the internal morphology and chemistry of AFBs, which should yield clues to their formation and evolution over time, have not been investigated.

Currently, one major theory for the development of cancer relies on reactive oxygen species (ROS), which can damage cells and the DNA within them. Therefore, most studies investigating the role of AFBs in MM are focused on investigating how reactive oxygen species (ROS) may be formed from the Fe present within the AFBs. However, inflammation resulting from the presence of the asbestos fibres within the lung environment, and the subsequent damage they inflict, has also been proposed as a potential mechanism for the onset of MM. Another recent theory invokes ionising radiation from Ra present within AFBs, which is known to damage DNA.

Accordingly, the aim of this study was to provide new insights into the role of AFBs in MM by the description of their internal characteristics and determination of the elemental composition of AFBs, both bulk and in-situ. The bulk major, minor, and trace elements of MM lung tissue samples were previously obtained via inductively coupled plasma mass spectrometry (ICP-MS) for which reproducibility was tested. The internal morphological and chemical characteristics of the AFBs were observed using scanning electron microscopy (SEM) and transmission electron microscopy (TEM) equipped with energy-dispersive X-ray spectroscopy (EDS). Meanwhile, the characterisation of Ra in the internal portions of the AFBs was performed by secondary ion mass spectrometry (SIMS).

The morphological and chemical compositions of the external surface of AFBs were determined by SEM analysis. SEM analysis was followed by cutting the observed AFBs with a focused ion beam, set on a TEM grid, and analysed by TEM with EDS and selective area electron diffraction (SAED). Through TEM-EDS and SAED, information regarding the internal morphology, chemical composition and crystallography were obtained. Based on these observations, an accretion model for AFB formation was developed from a smoker vs non-smoker perspective.

Reproducibility of the ICP-MS analysis revealed a sample bias among aliquots taken from the lung samples due to the heterogeneous number of AFBs and lung remnants in each aliquot. Therefore, in-situ analysis was necessary for precise detection of elemental concentrations, especially Ra, in AFBs, without contribution from other lung components.

For investigation of the Ra source in the ICP-MS data, Ra analysis in SIMS of the interior portions of individual AFBs was undertaken. However, before SIMS analysis could be undertaken, it was necessary to synthesise standards of the same composition as the AFBs (Fh) with specific elemental concentrations (Ra Fh standard series). Subsequently, it was necessary to develop an AFB sample preparation procedure for SIMS. With the techniques, protocols and SIMS analytical set-up developed here, $^{226}Ra^+$ ion signals were detected in the AFBs. Finally, the concentration of Ra was estimated using calibration curves established from the Ra Fh standard series and an AFB Ra hotspot model was drawn.

Acknowledgements

Table of contents

Aims and objectives

The aim of this study is the elucidation of the aetiology and carcinogenesis of asbestos-related malignant mesothelioma (MM). Currently, there are multiple theories surrounding the onset of MM, with reactive oxygen species (ROS) being the most accepted. However, high trace element and ^{226}Ra concentrations were previously found in the bulk lung samples of MM patients by Nakamura et al., 2009[1] and so the current thesis explores this theory through new analytical observations and interpretations and compares it to other conventional theories for the onset of MM.

^{226}Ra, known as the bone-seeking radionuclide due to its similar behaviours with Ca, causes bone sarcoma featuring radiation hotspots and diffuse radioactivity. Considering that bone and lung cells are equally sensitive to prolonged radiation exposure and ^{226}Ra and Ca behave similarly, the lungs may experience the same radiation events as the bones, namely hotspots and diffuse radiation. However, studies related to ^{226}Ra in lung cancer induction[2] are severely limited and no evidence has been drawn.

Nevertheless, Nakamura et al., 2009[1] proposed that ionising radiation from ^{226}Ra through the emission of α-particles may cause the induction of MM. However, the lung samples from the aforementioned study contained not only AFBs but also proteins from the lung environment. Therefore, the current study found it necessary to perform in situ analyses of AFBs using techniques that probe the micron to sub-micron scale in order to confirm their toxicity and role in cancer progression. Below the objectives that were undertaken to meet the primary aim of this study are outlined:

- Firstly, the external and internal morphology and chemical composition of AFBs were observed to gain insight into AFB formation and the distribution of Fe among smoking patients and non-smoking patients. Cigarette smoke is known to increase Fe concentrations; therefore, it was expected that higher Fe concentrations would be detected in smoking patients. Accordingly, if higher Fe concentrations are present, then they should adsorb more Ra since Fe is present as ferrihydrite in AFBs, which is known for its adsorption properties for Ra. As such, it was predicted that smoking patients may have higher Ra present in their AFBs than non-smokers and this hypothesis was tested.

- Secondly, Nakamura et al., 2009[1] detected trace elements and Ra abundances within AFBs using ICP-MS and this study was reproduced in order to test the reproducibility of the data. It was hypothesised that the sampling method for AFBs may lead to discrepancies in the number of AFBs and the amount of remnant lung material between aliquots used for analysis.

- Thirdly, for the determination of the Ra concentrations in the AFBs, Fh standards with Ra needed to be synthesised and AFBs required a mounting protocol for in-situ analysis. Subsequently, Ra was measured in AFBs, quantified and a hotspot model was devised for the onset of MM, which involved asbestos fibres, AFBs, and Ra.

1. CHAPTER 1 – Review of asbestos ferruginous bodies and mesothelioma

1.1 Asbestos fibres

The fibrous minerals, collectively termed asbestos, are a group of silicate minerals known for their prolonged commercial use. Asbestos displays advantageous properties, such as chemical and thermal resistance, high flexibility and tensile strength, high absorbency and low electrical conductivity[3]. For decades, asbestos was used as a "miracle" mineral. However, in the 1990s, evidence was amassed concerning it causing a rare and aggressive type of cancer known as malignant mesothelioma (MM), which led to its widespread ban. Nevertheless, because MM has a dormant stage of 20-30 years, it is expected that cases will reach high numbers in less than 10 years[4–6].

Asbestos fibres are divided into two mineral groups, amphibole, and serpentine asbestos. The serpentine group consists of only one mineral, chrysotile, a sheet silicate. Chrysotile is composed of a repeating unit in which an octahedral brucite layer is intercalated between two tetrahedral silicate layers. The amphibole group consists of actinolite, anthophyllite, tremolite, amosite (brown asbestos) and crocidolite (blue asbestos)[7]. The latter two minerals have been widely commercialised. Amosite ($Fe^{2+}_7(Si_8O_{22})(OH)_2$) and crocidolite ($Na_2(Fe^{2+}_3Fe^{3+})(Si_8O_{22})(OH)_2$) are hydrated silicates, distinguished by the number of Na, Fe, Ca, and Mg cations within their chemical formula. It is important to note that amphiboles have the highest amount of Fe out of all asbestos, crocidolite and amosite having up to 27 wt.% Fe. Amosite primarily contains Fe^{2+}, while crocidolite has both Fe^{2+} and Fe^{3+} in its crystal structure[5,6,8–10].

Asbestos occurs as two different varieties known as fibrous (asbestiform) and massive (nonasbestiform). Regarding amphiboles, amosite and crocidolite have nonasbestiform counterparts known as cummingtonite-grunerite and riebeckite, respectively. Mineral crushing displays the characteristic acicular morphology of amphiboles dictated by their distinctive cleavage. Amosite and crocidolite are categorised as "asbestos" when they take on an asbestiform (referring to the morphology of crystallising as polyfilamentous fibre bundles) or develop into fibres. Chrysotile is always in asbestiform, its fibres composed of tightly rolled up chrysotile sheets. Amphiboles are chain silicates in which tetrahedral silica groups are arranged into double chains. Octahedrally coordinated cations are wedged in between two of the double chains; the cations and silica are coordinated by oxygen[5,6,8,9,11–13].

1.2 Progression of asbestos bodies in the respiratory tract

Asbestos fibres enter the body through inhalation[14]. The asbestos fibres must first bypass the upper respiratory tract's defences (the nasal cavity, paranasal sinuses, and the pharynx) before reaching the lower respiratory tract (consisting of the trachea, bronchi, bronchioles, and the lungs). Constant asbestos exposure causes excessive inhalation of very long and thin fibres, leading to the bypass of the upper respiratory tract defences and the ciliated trachea, reaching the lungs and pleura, a pathway which has not been entirely elucidated[4,12]. Subsequently, the asbestos fibres trigger an inflammatory response which prompts detection by the alveolar macrophages (AM), recognising the fibres as foreign particles and attempting to phagocytose them. Due to the large length and insolubility of the asbestos fibres, they

cannot be phagocytosed by the AM. As a result, the AM break down by plasma membrane rupture due to the needle-like nature of the asbestos fibres. Consequently, a process called 'frustrated phagocytosis' occurs[3,15], in which the macrophages release cytotoxic chemicals, causing chronic inflammation and their death on the fibres, which marks the onset of asbestos ferruginous body formation[16].

1.3 Asbestos ferruginous bodies

Fe is the most abundant metal in the Earth's crust and is implicated in several key cellular functions in the human body, such as oxygen transport and DNA synthesis. Also, Fe is involved in the function of several essential enzymes, such as those involved in antioxidant processes and mitochondrial enzymes involved in cellular energy production. Fe also has the ability to generate reactive oxygen species (ROS) that can lead to biological macromolecular damage. In order to limit ROS in the human body, Fe is converted from Fe^{2+} to Fe^{3+}, followed by internalisation and sequestration into a storage protein called ferritin. Fe metabolism deregulation leads to Fe overload, which promotes the generation of ROS via the Fenton reaction. ROS production is known to be associated with cancer initiation and progression through oxidative DNA damage[5,9,17,18].

Ferritin is a Fe storage protein shaped like an empty shell, consisting of 24 subunits. The subunits can be further divided into the light chain and heavy chain types, the latter possessing the ferroxidase activity necessary for Fe sequestration[19]. Within the ferritin core, which contains up to 4,500 Fe atoms[20], Fe^{3+} clusters form a crystalline solid called ferrihydrite (Fh), together with trace amounts of inorganic phosphate. When Fe is in excess amounts, some of it is stored in haemosiderin, another Fe storage protein. Using x-ray diffraction peaks, Fh can be classified into two types, one small less-ordered 2-line (2L) variety and a larger, more crystalline 6-line (6L) form[17,18,21–28].

Asbestos fibres can gain ferritin from frustrated phagocytosis and adsorb Fe within the lung environment. Within the alveolar spaces, a complex mixture of phospholipids and proteins, known as lung surfactant, reduces surface tension within the alveoli while breathing. The lung surfactant proteins and phospholipids, and acid mucopolysaccharides are also adsorbed onto the fibres and mucopolysaccharides, in particular, are thought to help increase Fe adsorption[4,5,29–35].

"Frustrated phagocytosis" enables long Fe-containing asbestos fibres to adsorb large amounts of Fe onto their surface in the form of the Fe transport proteins, ferritin and haemosiderin. Additionally, cigarette smoke has been found to complex Fe and thus improve its availability in the lung environment. However, the accumulation of carcinogenic substances from sources such as smoking has been found to be associated with these proteins[36,37]. The Fe accumulation results in forming the AFBs, which consist of a thick golden-brown coat surrounding the asbestos fibre[5,20,29,33,38]. The AFB coat is either cylindrical, elliptical, apical, fragmented into rectangular or spherical units as a beaded aspect or with knobbed ends. Moreover, asbestos fibres are thought to adsorb haemoglobin, a Fe protein from red blood cells, originating from blood vessels injured by the fibres[39]. Nevertheless, there is little evidence concerning the source of the Fe and the mechanism of adsorption onto asbestos fibres and AFBs.

The primary model regarding MM progression is the oxidative stress-induced MM model,

proposed by Chew and Toyokuni, 2015[40]. There are two ways to induce oxidative stress onto the mesothelial cells. The first one involves catalysis, through the Fenton reaction, of the Fe from haemoglobin adsorbed on the asbestos fibre surface or the Fe directly from the fibre to generate hydroxyl radicals which induce oxidative stress. The second way of inducing oxidative stress is through the production of ROS species, which result from the 'frustrated phagocytosis' of macrophages. Moreover, mesothelial cells can endocytose asbestos fibres which once in the cells can cause DNA double-strand breaks and mitotic spindle disruptions, resulting in chromosomal aberrations. Also, the Fe from the fibres can further strengthen oxidative stress in the cells.

Another model for MM progression is related to the radioactive element ^{226}Ra, which was detected using ICP-MS by Nakamura et al., 2009[1] for bulk lung samples that contained AFBs. The result led to the development of the AFB formation and radium accumulation model for MM. ^{226}Ra causes ionising radiation through the emission of α-particles, which, if ingested, become highly genotoxic and cause lung cancer. Thus, ^{226}Ra may have a role in MM progression.

Pascolo et al. 2016, 2016[41,42] utilised X-ray fluorescence (XRF) to detect asbestos fibres and AFBs in tissue instead of using the conventional histochemical procedure, and to investigate Fe and calcium (Ca) deposition on the fibres. Pascolo et al., 2016[41] suggested that the asbestos fibres disrupted the Fe and Ca homeostasis, leading to their deposition on the fibres. The absorbed Fe was reported to be in the form of misfolded ferritin proteins. It was speculated that the release of cytosolic Ca and its adsorption onto the fibre induced the misfolding of ferritin, leading to loss of function and the release of Fe and ROS production.

Bardelli et al., 2017[20] utilised XRF and scanning electron microscopy (SEM) to observe AFBs. It was proposed that AFBs are richer in Fe internally than externally, due to overloaded ferritin changing into hemosiderin, despite difficulties distinguishing between ferritin and hemosiderin. Alternatively, it was proposed that Fe is released from the fibre, which gradually spreads within the AFB.

Di Giuseppe et al., 2019[16] utilised transmission electron microscopy (TEM), energy dispersive X-ray spectrometry (EDS) and selected area diffraction (SAED) to observe the exterior of AFBs. The SAED patterns identified not only Fh but also goethite, which is explained by the ferritin shell degrading and exposing the Fh from within the ferritin, leading to Fh altering into goethite and ROS production.

While the study of Bardelli et al., 2017[20] attempted to deduce chemical information about the interior of AFBs, no study has investigated the internal morphology or in-situ internal chemical characteristics of AFBs. As such, essential clues concerning the development of AFBs and their potential for inducing MM via known mechanisms have likely been missed.

1.4 Fe and smoking

Cigarette smoking is a particle-related exposure, containing over 5000 chemical species, including free radicals and Fe, which accumulate in the smoker's lungs, the lower lung region having the highest cigarette smoke (CS) particle deposition [37,43]. The amount of Fe in the tobacco of an average cigarette is 0.5 mg/g, of which 0.06% is transferred in the CS. This means that the daily inhaled Fe per one pack of 20 cigarettes is around 6 µg which can accumulate over years and decades[39]. The amount of inhaled Fe per cigarette pack is only

about 1/100 of the Fe content of the lung, which is 0.4-0.9 mg/g[39]. Active cigarette smoking dramatically increases the amount of CS particles in AM, described as humic-like substances (HULIS) and having red, brown, orange, and black colouration. About 7-10% of the CS particles consist of HULIS which complex organic compounds containing various oxygen-containing functional groups. The functional groups aid in the formation of metal cation complexes, especially with Fe. As intracellular Fe levels are low, the CS particles compete for the host Fe used by cells for critical roles, resulting in an iron deficiency for these cells[37]. As a result, CS particles in the lower respiratory tract contribute to the accumulation of host Fe in the AM and the deregulation of Fe homeostasis[39,43–45]. Following the Fe deficiency in the cells, Fe can either be imported in greater quantities, which if successful enables the cells to continue their roles. If insufficient Fe is imported into the cells or if the CS particles complex too much host Fe, the cell will not be able to fulfil its role, leading to cell death[37].

Furthermore, as the AM possess a central function in Fe recycling, the accumulation of Fe complexed by CS would thus increase the amount of Fe available during frustrated phagocytosis and likely contribute to the formation of AFBs.

CS is also known to have a synergetic effect on asbestos fibres, which amplifies cancer progression. Markowitz, 2015[36] reported that the death rate ratio of never-smoking insulators was 5.2 compared to the never-smoker control group. The lung cancer death rate ratio of the smoker and no asbestos exposure control group was 10.9, while the death ratio of smoker insulators was 53. The higher death ratio for smoker insulators demonstrated that cigarette smoke and asbestos fibres have a synergetic effect on cancer progression.

While a synergetic effect between inhalation of asbestos and smoking was found for lung cancer, no such relationship was reported for MM. Such an observation is interesting and needs further exploration. As such, the effects of smoking on AFB development will be investigated here[46].

1.5   Cancer and mesothelioma

The term cancer relates to a group of diseases defined by abnormal cell growth, which have the potential to spread throughout the body. The abnormalities within processes related to the growth and division of cells are known as the hallmarks of cancer. Such abnormalities facilitate tumour production and metastasis and are as follows: deregulation of growth factors leading to constant proliferation, evasion of tumour suppressors through disruption of the pRB (retinoblastoma protein) pathway, resisting apoptosis (programmed cell death) through the inactivation of the p53 tumour protein, achieving replicative immortality through the upregulated expression of telomerase, and promoting angiogenesis through the permanent activation of an "angiogenic switch". The hallmarks of cancer may culminate in a local invasion, leading to metastasis [47].

Malignant mesothelioma (MM) is a rare, aggressive cancer of the pleural, pericardial, or peritoneal cavities. MM targets mesothelial cells, which cover the internal organ surfaces and body cavities. The role of mesothelial cells is to prevent friction between organs, fulfilled by peristaltic and pulsating movements with secreted hyaluronic acid. About 70% to 80% of reported MM cases occur in the pleural cavity, known as malignant pleural mesothelioma [7].

MM is almost always associated with prolonged asbestos exposure; thus, asbestos-related

MM will be referred to as simply MM throughout the remainder of this thesis. MM has a long latency period, which starts on the first exposure and ends with MM development, with a median of about 39 years[48]. Amphiboles are more carcinogenic than chrysotile fibres, the latter having a greater solubility than the former and is thus more easily cleared by macrophages[10]. Nevertheless, before macrophages target the asbestos fibres, the fibres may be phagocytosed by the mesothelial cells, resulting in DNA strand breaks[40].

Incidence in 2010 for states within the U.S.A. with extensive asbestos usage was around 10-15 million, and those with minimal exposure were 1-2 million. These numbers are expected to rise due to the long latency period. In Japan, 100,000 cases are expected in the next 40 years[5,7,10,40,49,50]. As such, many people will develop mesothelioma over the coming decades. Therefore, an effective treatment should be developed to treat MM.

However, before a treatment can be devised, it is paramount that the factors relating to the initiation and development of the disease are elucidated. At current, the only known physical features associated with MM are AFBs. Therefore, further information concerning the growth of AFBs and how they are related to MM is required.

1.6   Ferrihydrite and asbestos fibre adsorption properties

Asbestos fibres contain rare earth elements (REE), which can contribute to the fibre's ability to induce lung cancer and MM. However, investigation of REE toxicity in the lungs is mainly constricted to La, Ce and Gd. The trace elements can co-precipitate with phosphate groups, one of the main components of ferritin, resulting in their crystallisation and injuries within the lung parenchyma. When the AFBs start to form and accumulate ferrihydrite (Fh) from ferritin, the trace elements from the fibres may partition into the AFBs, amplified by the REE's affinity to precipitate with phosphate[51–56].

Fh has been shown to adsorb toxic elements, such as Pb[57], Cd[58], and Cu[57], while ferritin is known to adsorb U[59], Be[60], Cd[58] and Zn[61]. Moreover, Nakamura et al.,2009[1] detected high concentrations of these elements and also radioactive ^{226}Ra in the MM samples, which contained both AFBs and remnants of lung-populating proteins. ^{226}Ra is also known to be absorbed by Fe oxyhydroxides such as Fh[62,63]. ^{226}Ra may induce deregulations within the DNA through ionising radiation. As such, ^{226}Ra and Ba will likely behave similarly in the lung environment. Therefore, Ba found in higher concentrations than ^{226}Ra within bulk lung samples should act as a tracer for ^{226}Ra within AFBs[59,62,64,65].

1.7   Radioactive Ra in the human skeleton: a case study for Ra in the lungs

^{226}Ra is an α emitter with a half-life of 1600 years and the 5th radionuclide daughter in the ^{238}U- ^{206}Pb decay series[66]. Furthermore, Ra is an alkaline earth metal and is expected to have similar chemical behaviours with the other alkaline earth elements from the same chemical group of the period table, especially Ba and Ca[67]. As the ionic radii of Ra and Ba have similar ranges, Ba is often used as a chemical analogue for Ra behaviour prediction when there are no Ra data available[67,68].

Blood clearance of ^{226}Ra leads to its deposition mainly in the skeleton while a fraction is deposited in tissues such as the lungs and a large fraction is quickly excreted. ^{226}Ra is known

as the bone-seeking radionuclide, its chemical similarity to Ca is used for the determination of its behaviour in the body[69]. The mean ^{226}Ra activity deposited in bone was estimated at 0.31 Bq/kg dry bone while in other tissues such as in the lungs the ^{226}Ra activity was around 0.005 Bq/kg[66]. As the ^{226}Ra irradiates the bones it will lead to bone sarcomas.

The bones of the skeleton present nonuniform distributions of Ra that are also observed at a microscopic level. When a person is irradiated, the high activity of ^{226}Ra in the blood deposits in great amounts during the mineralisation of several units of bone formation, resulting in a hot spot. During hotspot formation, when the bone apposition adsorbs a single dose of Ra, it will result in a gradual reduction of the dose rate to neighbouring bone surface tissues. The reduced dose rate is below the maximum dose of the hot spot, concluding that the hot spot accumulated dose would be slightly higher than the diffuse component dose. Average hotspot concentrations are about an order of magnitude higher than average diffuse concentrations[70].

The hotspot survival for the irradiated cells would be 0.09% so the cell survival chance around the hotspot is close to zero resulting in their death due to high amounts of radiation. Therefore diffuse radioactivity might be the main cause of inducing cancer among patients where bone cancer was developed[70].

In addition, the amount of cell death around the hotspot in comparison to the cell death around the diffuse radioactivity, and the diffuse concentration elevations in comparison to the hotspot concentrations which occur during prolonged exposure led to the conclusion that the endosteal dose caused by diffuse radioactivity is the main cause of osteosarcoma induction[70].

Previously[1], ^{226}Ra was detected within the bulk lung samples of MM patients which concluded that AFBs contain radioactive ^{226}Ra which can cause DNA strand breaks through ionising radiation. Therefore, the main radioactive nuclide investigated in AFBs is ^{226}Ra.

Ra is present in the air in resuspended soil particles. A dust concentration of 50 µg/m^3 is often assumed for the inhalation pathway evaluation. The worldwide concentration of 32 Bq/kg for Ra in the soil is used for the estimation of 1.5 µBq/m^3.

Information regarding lung cancer is currently ambiguous although there might be a connection between lung cancer incidence and Ra intake or period of exposure. No conclusions have been drawn[66].

Both lung and bone cells are almost equally sensitive to prolonged exposure to radiation resulting in bone sarcoma initiation and lung carcinoma initiation[71]. Therefore, in the investigation of AFBs with Ra in the lungs, it is assumed that ionising radiation in the lower lungs behaves similarly as it does in the skeleton, especially in the case of hotspots and diffuse radioactivity[70].

1.8   Radioactive Ra sources to the lungs

Asbestos fibres have the ability to emit low-level α radiation which can irradiate the lung for long periods of time knowing that the fibres are quite immobile in the lower lung. The highest Ra activity among several types of asbestos fibres was detected in amosite fibres (0.044 Bq/g). Meanwhile, for crocidolite fibres, the highest Ra activity was half of the amosite fibres (0.023 Bq/g)[72]. Besides the Ra concentration of the asbestos fibres, their ability to penetrate the lung and to persist at a critical site, such as the mesothelium, is also an important ability for dose delivery. Normal dust particles are quite mobile, have no accumulation mechanisms and are quickly cleared from the lung, in comparison to asbestos fibres which are immobile in the lung and their lung clearance is much slower[72]. Accordingly, the α radiation of asbestos fibres should be taken into consideration regarding the incidence of MM and AFB formation.

Fe oxyhydroxides have been found to adsorb Ra[67]. Therefore, the main component of AFBs, namely Fh, may be the main reservoir of Ra adsorption. Furthermore, soil fractions were separated through a selective chemical extraction, revealing that the organic (humic) matter fraction was enriched in Ra, which indicates great Ra uptake by vegetation[73].

The main sources of radionuclide transfer to humans are food and water ingestion. Therefore various foodstuffs and drinking waters have been a subject of research regarding their radium isotope concentrations[67]. For foodstuffs, the transfer factors (TF) between the soil and plants were evaluated, which is the ratio of activity concentration in a plant to activity concentration in the soil[74].

The Ra concentrations of rice paddy field soils were determined using Ba as a yield tracer, since Ra has no stable isotopes, and Ba and Ra are in the same periodic table group. The Ra concentration in the soil was higher in SW Japan than in NE Japan, the SW Japan soil having a geometric mean was 40.4 Bq/kg dry, while the NE Japan soil had a geometric mean of 27.8 Bq/kg dry[74]. Uchida and Tagami[75] evaluated the TFs of various crops in Japan in which leafy vegetables had the highest TF of 1.2×10^{-2}. Furthermore, the TFs of Ra correlated with the TFs of Ba, suggesting that the TFs of Ba could act as an analogue for the TFs of Ra. Nevertheless, the TFs of Ba had a wider range than the TFs of Ra[75].

Netten et al., 2000[76] detected traces of ^{226}Ra in 2 seaweed products from Japan of 58-206 Bq/kg, while Ota et al., 2009[77] detected ^{226}Ra concentration in green tea leaves and eggs of 1.9 Bq/kg fresh weight and 0.26 Bq/kg fresh weight, respectively. In addition, they also determined the range of 226Ra concentrations in daily foods from Japan to be between 0 and 3.9 Bq/kg, the highest being in algae, cereals, seasoning and beverages, and nuts and seeds. Therefore, the typical diet of a Japanese person may supply large amounts of Ra which accumulate on the AFBs over years and decades.

Cigarette manufacturing includes the use of tobacco leaves which contain radioactive elements that are present in the soil due to the Earth's crust containing several radioactive elements including uranium and radium. Higher concentrations of uranium in the tobacco fields might lead to a large amount of ^{210}Po and ^{210}Pb since they belong to the uranium-radium decay series[78,79]. The soils are often excessively fertilised, for greater profits, with phosphate fertilisers that are rich in uranium and its decay products. Phosphate fertilisers are enriched in uranium decay products due to being extracted from the rock mineral "apatite" known for its high levels of Ra and ^{210}Po and ^{210}Pb. Accordingly, the tobacco plant roots uptake the radionuclides from the soil and concentrate these radionuclides in the tobacco plants[78,80]. About 25% of the radionuclide activity of the CS remains in the cigarette ash and filter while 75% is inhaled and deposited in the lungs.

Accordingly, Boumala et al., 2019[80] detected Ra in tobacco at an average of 8.17 Bq/kg which may suggest that constant smoking continuously supplies Ra to the lungs, thus increasing the carcinogenicity of AFBs and potentially leading to MM initiation.

2. CHAPTER 2 – Morphological and chemical characterisation of AFB

2.1 Summary

The chemical and morphological characteristics of AFBs from smoking and non-smoking patients, respectively, were investigated for a preliminary understanding of the formation and composition of the AFBs from a smoking vs non-smoking perspective. Previously, the chemical and morphological characteristics of AFBs were most often obtained using optical and electron microscopy[16,81]. Due to the small size of AFBs, secondary electron microscopy (SEM) and transmission electron microscopy (TEM) were found to be more favourable for morphological description. SEM and TEM include an essential component known as energy dispersive X-ray spectroscopy (EDS), which was used to obtain information regarding the chemical composition of AFBs. SEM enabled external morphological and chemical observations, while TEM allowed internal morphological and chemical observations. Internal observations of the AFBs allowed more insight into AFB formation. In addition, selected area diffraction (SAED) patterns were obtained in TEM which revealed crystallographic information concerning the samples analysed. Furthermore, for the preparation of TEM-appropriate samples, thin samples of under 150 nm thickness were cut using a focused ion beam scanning electron microscope (FIB-SEM) system[8,14,82].

Based on the internal morphology and chemical composition observations in TEM, an AFB formation model was drawn where the AFBs of smoking patients were more Fe-rich and denser than that of non-smoking patients. The AFBs of smoking patients might adsorb more Ra due to a larger volume of Fe.

Furthermore, SAED of AFBs from all patients revealed only ferrihydrite (Fh) which is evidence for the fact that the ferritin shells remained intact which prevented the Fh to alter and create reactive oxygen species (ROS). Therefore, oxidative stress-based malignant mesothelioma (MM) is not possible due to the lack of ROS, so another mechanism might be responsible for MM, such as ionising radiation.

2.2 Materials and Methods

2.2.1 Lung samples

For this project, lung samples from six patients with MM were acquired. The lung samples were previously digested and quantified at Yamaguchi Ube Medical Center, and permission to conduct research on these human samples was obtained from the Review Board of the Yamaguchi Ube Medical Centre. The procedures are described in Nakamura et al., 2009[1] as follows: 5g of lung tissue obtained from each patient were weighed, minced, dried and re-weighed. The resulting lung tissue was transferred to a 50 ml centrifuge tube to which 40 ml of bleach containing 20 % NaOCl and 5% KOH were added. The tissue was left to digest for 24-48 hours, followed by centrifugation at 3000 rpm for 30 min and its supernatant aspirated, leaving 1 ml of liquid above the pellet. This step was followed by the resuspension of the pellet in 50 ml of deionised milli-Q pure water and thoroughly mixed. The centrifugation, aspiration, resuspension, and mixing steps were repeated thrice, resulting in a processed lung tissue suspended in milli-Q pure water. For a smoker vs non-smoker comparison, two smoking patients (H and A, noted as S1 and S2) and two non-smoking patients (E and K, noted as N1 and N2) were selected for a comprehensive TEM analysis, whose characteristics and AFB quantification data are described in Table 1.

2.2.2 Machines and techniques

An optical microscope, operated in plain polarised light mode, uses light photons for visualisation, which have a wavelength of about 400-700 nm. In order to use larger magnifications than the optical microscope and to see finer details, particles with a shorter wavelength than photons were utilised. In the current study, electrons with a wavelength of 1.23 nm were used. Electron microscopy was initially developed due to the need for observations at smaller scales than was possible with photons.

SEM is a microscope based on an electron beam that interacts with the surface of a sample under high vacuum conditions. The electron beam penetrates the surface in a teardrop shape, with the size being dictated by the electron beam's energy, the angle at which it hits the sample, and the atomic masses of the elements present within the sample. This interaction leads to the emission of various particles, such as secondary electrons, backscattered electrons, and X-rays, which are detected to obtain information regarding the sample. The shallowest signal comes from secondary electrons, knocked out by an incident electron from the orbits around the atom. The secondary electrons supply the highest spatial resolution images and topographic information. Incident electrons that reach close to the atom's nucleus and scatter at a large angle are called backscattered electrons and provide compositional information. For backscattered electrons, the higher the atomic mass of the element, the brighter the contrast[83].

Characteristic X-rays concern the electrons from the most inner electron shells, K, L and M shells, K being the closest to the nucleus. The L shell has three subshells, while the M shell has five subshells. The ionisation energy decreases from the innermost shell to the outermost, with the K shell having the highest one. Thus, electron removal from the K shell requires more energy than other shells. To obtain characteristic X-rays, an incident electron knocks out an electron from the inner shells, resulting in the ionisation and destabilisation of the atom. Subsequently, the inner shell vacancy is replaced with an electron from an outer shell, resulting in atom stabilisation and emission of X-ray photons. The emitted X-ray energy is the difference between the ionisation energies of the electrons implicated in the transition. The characteristic X-ray lines follow the Siegbahn notation, which first shows the name of the element measured, followed by the ionised electron shell involved in the X-ray production. The notation ending with either α, the most intense, β or γ, reflects the relative intensity of the line from each shell. For instance, the K line family consists of K_α and K_β X-ray lines. The EDS detector obtains a spectrum based on the intensities of these characteristic x-rays in the form of X-ray counts (counts per second), from which chemical composition is obtained. One limitation regarding EDS is that light elements ($Z<11$) cannot be identified because their energies are too low[84].

The SEM analysis of the current study was performed using the JSM-7001F field emission SEM (FE-SEM) at an accelerating voltage of 15 kV. The SEM was equipped with an Oxford INCAx-act EDS system.

Table 1: Mesothelioma patient details from which lung tissue samples were obtained.

Patient	A	E	H	I	K	M
Age	65	65	63	59	51	61
Gender	M	F	M	M	F	M
Type of MM	Biphasic	Biphasic	Biphasic	Other	Epithelioid	Biphasic
Initial Symptom	Cough	Chest pain	Cough	Pleural thickness	Chest pain	Chest pain
Occupation	Quarrying industry	Insulation industry	Asbestos scrapper	Railway carriage builder	Post office	School teacher
Smoking experience (year)	35	None	40	None	None	10
	Quit 6 months before operation		Quit 1 year before operation			Quit 30 years before operation
Surgery	Left extrapleural pneumonectomy	Left extrapleural pneumonectomy	Autopsy	Left extrapleural pneumonectomy	Left extrapleural pneumonectomy	Left extrapleural pneumonectomy
Surgery Date	October 2007	July 2007	December 2003	September 2006	November 2007	March 2008
AFB per dry lung (fibres/g)	7.9×10^3	4.4×10^5	3.2×10^5	1.7×10^4	4.0×10^3	7.1×10^2
Weight of one AFB (µg)	1.5	85	61	3.2	0.77	0.14

The SEM-FIB system JEOL JIB-4500 was used for cutting and preparing the TEM samples. FIB uses a focused ion gun based on a gallium ion beam, while SEM uses an electron beam, as stated previously. In both SEM and FIB, the image of the sample is formed based on the secondary electrons' intensities created at every raster location. FIB uses gallium as a liquid metal ion source, kept in a reservoir close to a sharp tungsten needle through which it is pulled by a high extraction field into a sharp cone. The advantages of using gallium include the ability to form a very fine beam size and its low melting point, being in the liquid state at room temperature[85].

The accelerating voltage of FIB was 30 kV, while that of SEM was 20 kV. At a tilt of 0º, the SEM is perpendicular to the sample, while at a tilt of 52º, the FIB is perpendicular to the sample.

TEM also utilises an electron beam under a high vacuum. The electrons are transmitted through the ultra-thin sample, forming an image under it. The image is then magnified and focused on an imaging device such as a fluorescent screen. TEM provides information regarding microstructure, crystallography through SAED patterns, and chemical composition through EDS. There are two different imaging modes when using only one beam to visualise the sample, known as bright field and dark field (DF). The bright field is characterised by using the direct beam to form an image from the unscattered electrons. Areas that are thicker or contain higher atomic number elements appear darker, while areas with no sample appear brighter. DF uses the diffracted beam to form an image from the scattered electrons, for which the sample needs to be tilted so that these electrons move along the optic axis. Where there is no sample, the areas appear black, while bright areas are denoted by thicker areas in the sample and elements of high atomic numbers[86].

When a crystalline structure is hit by an electron beam, diffraction occurs, leading to SAED patterns as a result of the electron wavelength and atom arrangement in the crystal, which are explained by Bragg's law: $n\lambda = 2d\sin\theta$. N is an integer, λ is the electron wavelength, d is the spacing of the diffracting planes, and θ is the angle between the electron beam and the planes. If λ of the incident beam is known and θ can be measured experimentally, the interplanar spacings in the crystal can be determined. The ability to obtain crystallographic information is the most important aspect of TEM. When obtaining SAED patterns, the region of interest is delimited by the SAED aperture. Subsequently, the crystalline sample produces diffracted beams, forming an image under the sample in a region called the back focal plane. The image can be represented as an array of dots or a ring pattern. Polycrystalline samples yield sharp ring patterns, while amorphous ones yield diffused ring patterns[86].

2.2.3 Sample preparation for SEM

In order to mount the digested lung tissue from the previously described patients, a clean glass slide for each patient was prepared. The glass slides were first marked, sonicated in ethanol for 5 minutes, followed by sonication in Milli-Q pure water for 5 minutes and wiped. Subsequently, 100 µl of the digested lung tissue of each patient were pipetted onto each respective glass slide and left to dry overnight at room temperature. After completely drying the samples, the glass slides with the dried samples were carbon coated and placed onto an SEM sample holder. Carbon tape was used over the glass slide and the sample holder to reduce the sample's charging. The samples were then loaded into the SEM for observation and analysis.

2.2.4 FIB processing for TEM analysis

For TEM analysis, samples were sliced to a thickness of under 150 nm, using FIB coupled with SEM. TEM requires nanometre thick samples so that the electrons are able to pass through the samples and allow successful observations and analyses. The sliced samples were placed on a 3 mm diameter copper TEM grid.

The sample was titled at 52º so that the FIB was perpendicular to the sample. Figure 1 shows the steps of cutting an AFB. Firstly, the asbestos of interest was located and set to the desired position and cut location (Fig. 1a). Subsequently, the region of interest was coated with gallium to prevent any damage during sample cutting. Within 100-200 µm from the sample, a needle injected gas onto the surface. The gas was decomposed by the rastering of the gallium beam, leaving a metal deposited layer, its by-product being ejected through the vacuum system (Fig. 1b, c). Afterwards, two large trenches were drilled with the coarsest beam along the longer sides of the selected area to facilitate the subsequent picking up of the body (Fig. 1d, e). A finer and smaller beam was used to cut an appropriate width of the body on each long side so that there was enough sample for fine cutting (Fig. 1j, k). The fine beam was utilised to cut underneath the body while tilted at 0º in preparation for the lift-off of the final product (Fig. 1j, k). Subsequently, a finer beam was used to polish the longer ends of the AFB. Once a thickness of less than 150 nm was achieved, the AFB was cut out at its shorter sides until it was loose enough to be able to be picked out (Fig 1l, m)[85].

After cutting the AFBs with the FIB, the AFBs were picked up under an optical microscope using a sharp glass needle and set onto a biofilm on a 3 mm diameter TEM grid. The lifting out was possible due to electrostatic forces. Afterwards, the AFBs were mounted and loaded into the TEM and analysed.

2.2.5 TEM analysis

JEM-2100F (JEOL) was used for TEM analysis at an accelerating voltage of 200 kV. The AFB slices were visualised using DF imaging, and their chemical composition was quantitatively determined by EDS. In addition, the crystal stoichiometry of the asbestos fibre from each AFB was determined by EDS analysis and their chemical formulas were estimated[87].

For better elemental distribution observations, EDS analysis was done at a magnification of 80,000x. The large magnification of 80,000x meant that most AFBs could not fit into one image and required multiple line analyses to produce an entire transect across a given AFB. As such, there were gaps between each line analysis on a single sample, which were between 100-240 µm. EDS analysis data was normalized to 100%.

The crystal structure of the phases within the AFB was determined through SAED. The SAED patterns featured ring patterns or an array of dots, which are the result of diffracting beams from the crystalline samples. The SAED patterns were then compared to the literature to identify the specific phases present.

2.3 Results
2.3.1 External morphology

SEM analysis was undertaken in order to identify AFBs within the dried lung samples, map their location and describe their morphology. AFBs have non-uniform Fe-rich coats enclosing the fibre and their extremities exposed. The AFB coats are either whole or divided into spherical or cubical fragments, having the profile of a string of pearls. The observed AFB morphologies here were spherical (Fig. 2b), cylindrical (Fig.2b), elliptical (Fig. 2c), carrot-shaped (Fig. 2d), dumbbell-shaped (Fig. 2e) and apical (Fig. 2a). The AFB nomenclature was taken from Giuseppe et al., 2019[16]. Table 2 shows the number of identified AFBs in SEM along with their length and width ranges. The AFBs of patient N1 had thicker and longer AFBs than the rest of the patients, and the non-smoking patients had wider AFBs than the smoking patients. SEM images of the selected AFBs for TEM analysis are shown in figures 2 and 3.

The exterior of the AFBs and fibres featured several round inclusions (0.05-0.17 µm) (Fig. 1b, d), which were also present on the naked asbestos fibres. The round inclusions were also present in the internal part of the AFBs, which suggests their involvement in the initial AFB formation. However, their distribution within the body seemed random, being more evident towards the exterior of the body.

2.3.2 Internal morphology

DF imaging was used to observe the AFBs (Fig. 4 and figs. A1-A16 in the appendix). The white wavy lines occurring on the AFBs are due to the adherence of the bodies to the TEM copper grid. The white circles over some AFBs, such as AFB 2 of smoking patient S1, are a result of EDS analysis damage.

The AFBs of all patients featured several concentric layers with variable widths and shading. Porous layers were the layers that had small holes present within them, which gave them a darker appearance. Dense layers were the layers that had no or almost no small holes and thus had a brighter appearance. Most of the AFBs from the smoking patients featured a porous halo-ring around the fibre or several layers from the fibre. The AFBs of the non-smoking patients had more concentric layers than the AFBs of the smoking patients. Thus, based on the external widths and the longest and shortest diameter measurements in table 2 and figure 5, the AFB diameters of the non-smoking patients were found to be larger than those of the smoking patients.
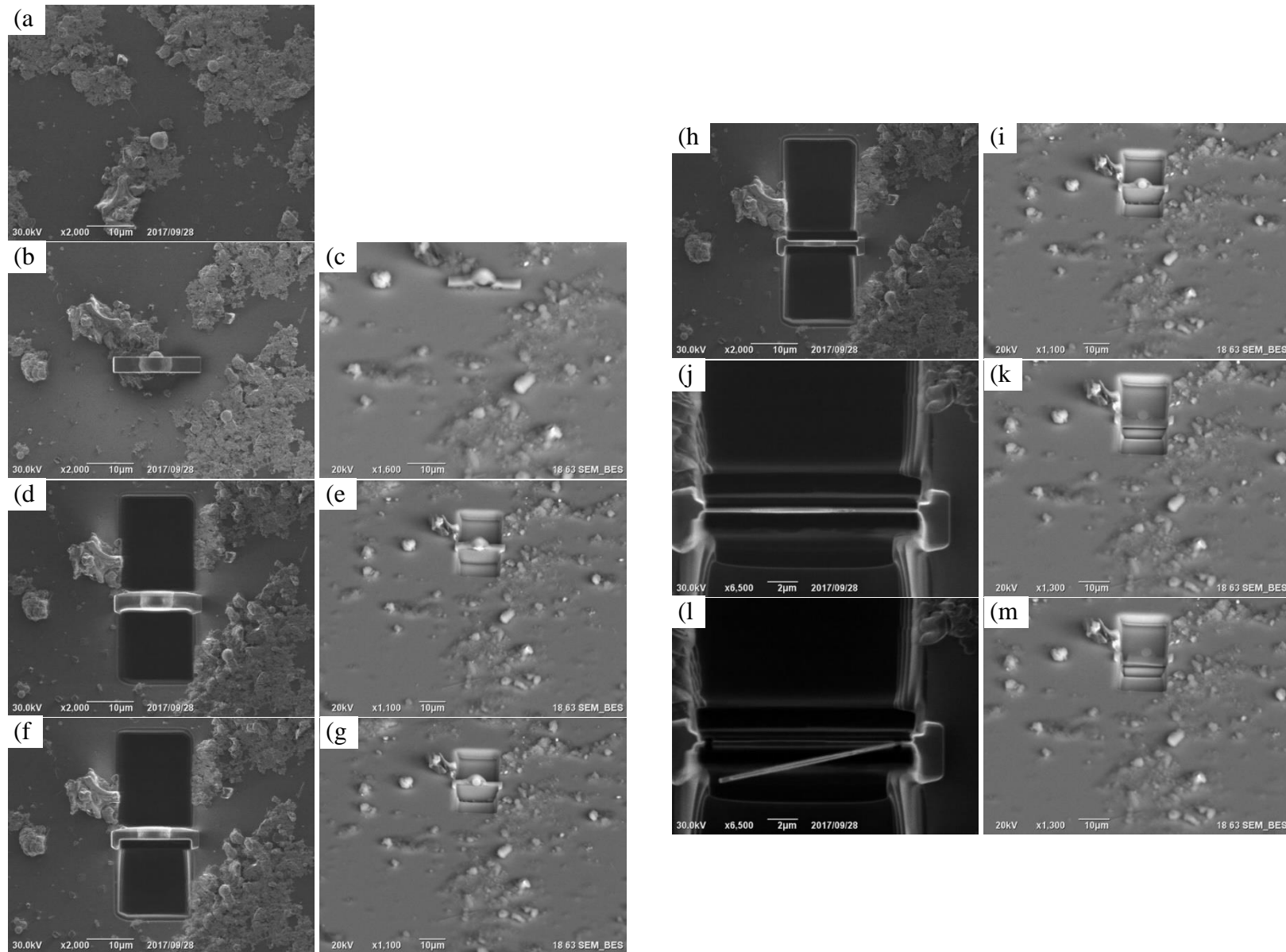
Figure 1: The sample preparation procedure to slice an AFB (patient S1: AFB2) for TEM analysis. (a) The positioning, (b, c) deposition, and (d, e) thetrench milling of an AFB of interest. (f, g, h, i) The fine cutting, (j, k) the undercutting, and (l, m) the final side cutting of the AFB of interest.
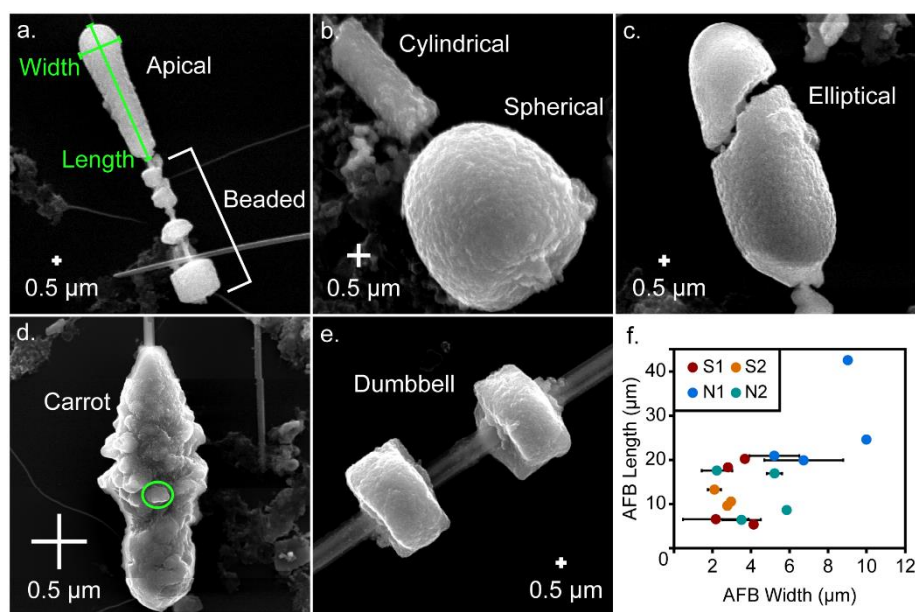
21

Figure 2. SEM images of the external morphology of different AFBs analysed by the current study: **a**. an apical form and beaded AFB from patient N1, **b**. cylindrical and spherical forms from an AFB from patient S1, **c**. an elliptical form from an AFB from patient N1, **d**. a carrot form from an AFB from patient N1, **e**. a dumbbell form from an AFB from patient S1 and **f**. a plot of average AFB form width against AFB length. A typical length and width measurement are shown in f., with the width and length being taken along the longest dimensions. The circle in d. highlights the sphere or elliptical-like components that form the AFB coats, with this particular component being 120 nm by 220 nm in diameter. N1 and N2 are non-smoking patient N1 and N2 and S1 and S2 are smoking patient S1 and S2, respectively.
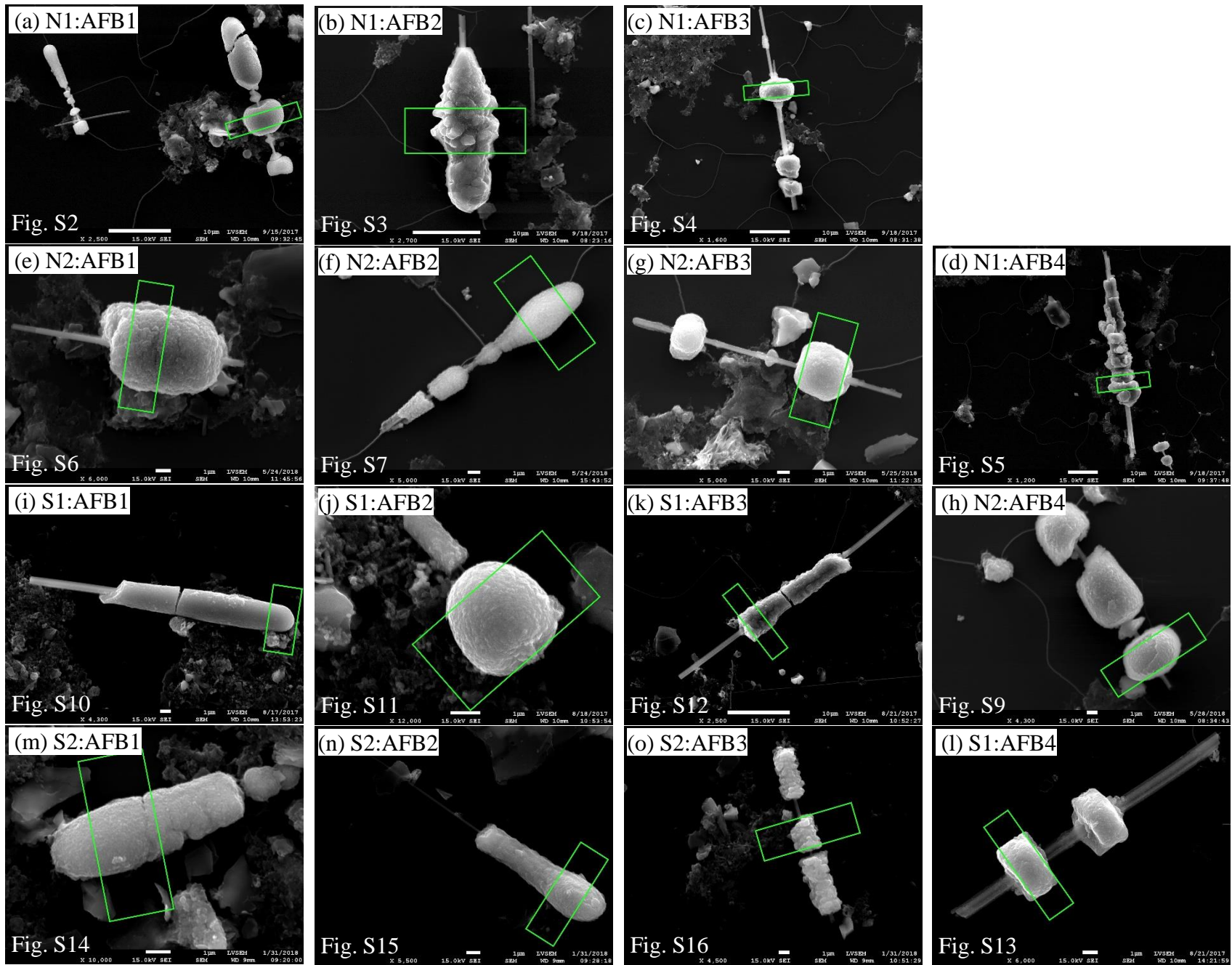
Figure 3: External morphology of AFBs observed by SEM from the non-smoking patient (a–d) N1 and (e–h) N2, and smoking patient (i–l) S1 and(m–o) S2, prior to cutting by FIB for TEM analysis. The area of interest is shown by a green rectangle in each image.

Table 2: Information regarding asbestos fibres and AFBs, including the external lengths, widths and type of the AFB fibres and bodies, and internal diameters of the fibres and bodies, all in µm.

Patient	AFB	Fibre			Body		Fibre-1 Diameter		Fibre-2 Diameter		Fibre-3 Diameter		Body Diameter	
		length	width	Type	length	width	long	short	long	short	long	short	long	short
N1	1	26.67	0.37	Grunerite	20.88	5.21 ± 1.29	0.86	0.32	-	-	-	-	6.22	6.22
	2	29.39	1.07	Grunerite	24.59	10.00	0.97	0.56	-	-	-	-	8.43	7.39
	3	51.80	0.83	Grunerite	16.94	6.73 ± 2.05	0.80	0.54	0.49	0.33	-	-	8.05	-
	4	71.10	1.71	Grunerite	42.55	9.03	1.62	1.10	0.48	0.28	-	-	7.72	-
	Average	44.74±20.87	1.00 ±0.56		26.24±11.31	7.74 ±2.18	1.06 ±0.38	0.63 ± 0.33	0.49±0.01	0.31 ±0.04	-	-	7.61 ±0.97	6.81 ±0.83
N2	1	15.89	0.42	Riebeckite	8.59	5.86	0.63	0.42	-	-	-	-	5.45	4.93
	2	19.90	0.42	Riebeckite	17.53	2.24 ± 0.79	0.42	0.35	-	-	-	-	3.11	3.09
	3	22.19	0.40	Grunerite	6.40	3.51 ± 1.00	0.45	0.33	-	-	-	-	4.52	3.98
	4	20.28	0.39	Riebeckite	16.92	5.22 ± 0.4	0.49	0.13	-	-	-	-	5.54	5.21
	Average	19.57 ±2.65	0.41 ±0.02		12.36±5.69	4.21 ±1.65	0.50 ±0.09	0.31 ± 0.12	-	-	-	-	4.66 ±1.13	4.30 ±0.96
S1	1	24.87	0.70	Grunerite	18.30	2.81	0.92	0.32	-	-	-	-	2.56	2.01
	2	7.01	0.14	-	6.54	2.18 ± 1.7	0.27	0.06	-	-	-	-	3.29	3.20
	3	48.29	0.89	Grunerite	20.22	3.69	0.88	0.26	-	-	-	-	4.51	3.00
	4	21.18	1.02	Grunerite	5.32	4.15 ± 0.16	1.00	0.26	-	-	-	-	3.94	3.75
	Average	25.34±17.13	0.69 ±0.39		12.6 ± 7.75	3.21 ±0.88	0.77 ±0.34	0.22 ± 0.11	-	-	-	-	3.58 ±0.84	2.99 ±0.73
S2	1	9.92	0.32	Riebeckite	9.55	2.78	0.32	0.19	-	-	-	-	2.29	2.12
	2	22.91	0.19	-	10.57	2.96	-	-	-	-	-	-	2.69	2.59
	3	16.41	0.24	Riebeckite	13.25	2.10 ± 0.35	0.26	0.06	0.18	0.08	0.19	0.07	2.07	1.61
	Average	16.41 ± 6.5	0.25 ± 0.07		11.12±1.91	2.61 ± 0.45	0.29 ± 0.04	0.13 ± 0.09					2.35 ±0.31	2.11 ±0.49

Non-smoking patient N1

AFB 2 (Figure A2 of the appendix) had several denser layers than the other AFBs, which were denoted as dense layer outliers. Most porous layers were towards the exterior of the AFBs, with a few near the asbestos fibres.

The asbestos fibres had long diameters between 0.48 and 1.62 µm and short diameters between 0.28 and 1.10 µm. The AFB bodies had long diameters between 6.22 and 8.43 µm and short diameters between 6.22 and 7.39 µm. AFBs 3 and 4 (Figures A3 and A4 of the appendix) had two asbestos fibres, their smallest fibres having the smallest long diameters among all the non-smoking patient E AFBs. The biggest fibres of AFBs 3 and 4 had the fourth, and first longest fibre diameters of all the studied AFBs. The AFBs 2 and 3 had the longest diameters, between 8.43 and 8.05 µm, respectively. The AFBs 3 and 4 also featured porous halo-like layers around their fibres, with the halo being darker in AFB 4. Furthermore, AFB 1 had a porous layer around its fibre, while AFB 2 had dense layers around its fibre. The asbestos fibre and AFB diameters are shown in table 2.

Non-smoking patient N2

Only AFB 2 (Figure A6 of the appendix) had a porous layer surrounding its fibre, while the rest of the porous layers were spread out throughout the AFB. The long diameters of the fibres (0.42-0.63 µm) were larger than the smoking patient S2 but smaller than the rest of the patients. The short diameters of the fibres were between 0.13 and 0.42 µm. The AFBs bodies had long diameters between 3.11 and 5.54 µm and short diameters between 3.09 and 5.21 µm. There appeared to be fewer layers in the AFBs of non-smoking patient N2 than in non-smoking patient N1 but more layers than in the smoking patients.

Smoking patient S1

The AFBs of smoking patient S1 were smaller (long diameters of 2.56-4.51 µm and short diameters of 2.01-3.75 µm) and denser than those of the non-smoking patients. AFB 2 (Figure A10 of the appendix) had a set of dense layers surrounding its fibre, followed by a porous halo-like ring and another set of dense layers towards the exterior of the AFB. The rest of the AFBs had an initial porous ring or area around their fibres, followed by dense layers, having fibres with long diameters between 0.27 and 1.00 µm and short diameters between 0.06 and 0.32 µm.
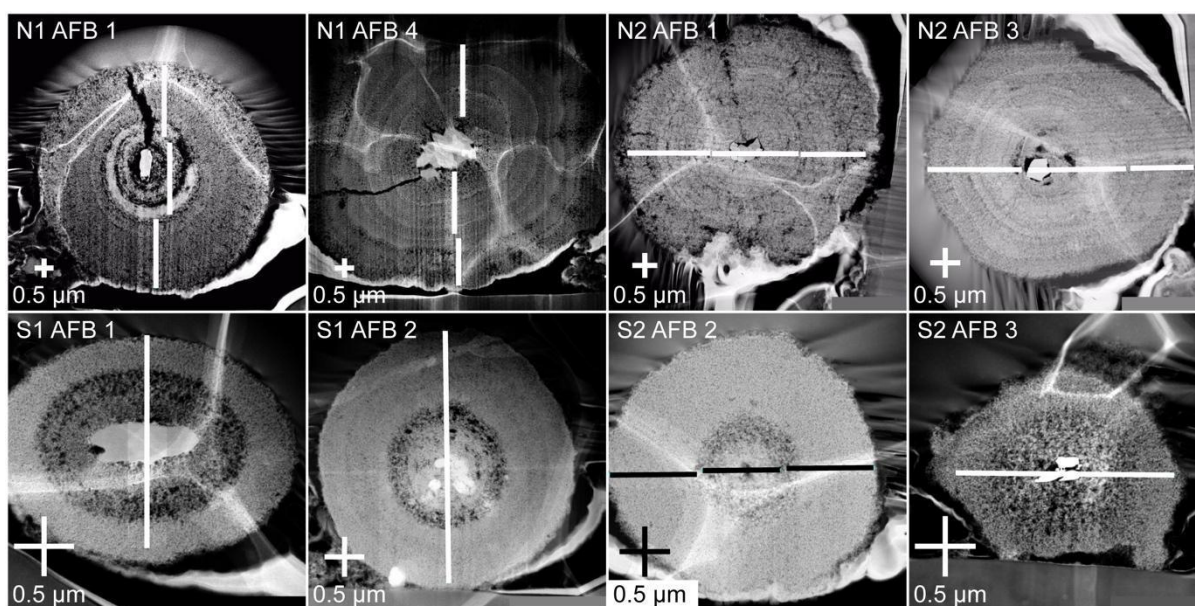
Figure 4. TEM dark-field images of cross-sectional views from AFBs of each patient. Two AFBs were selected from each patient; the patient and AFB numbers are indicated in the top left-hand corner of each panel. The white or black lines indicate the transects along which the EDS data was taken. Note that the wavy white discolouration on the surface of the AFBs is from the copper biofilm used to fix the AFBs in place. N1 and N2 are non-smoking patient N1 and N2 and S1 and S2 are smoking patient S1 and S2, respectively. Note that the EDS line analyses of AFBs from patient N1 did not pass through the fibres.
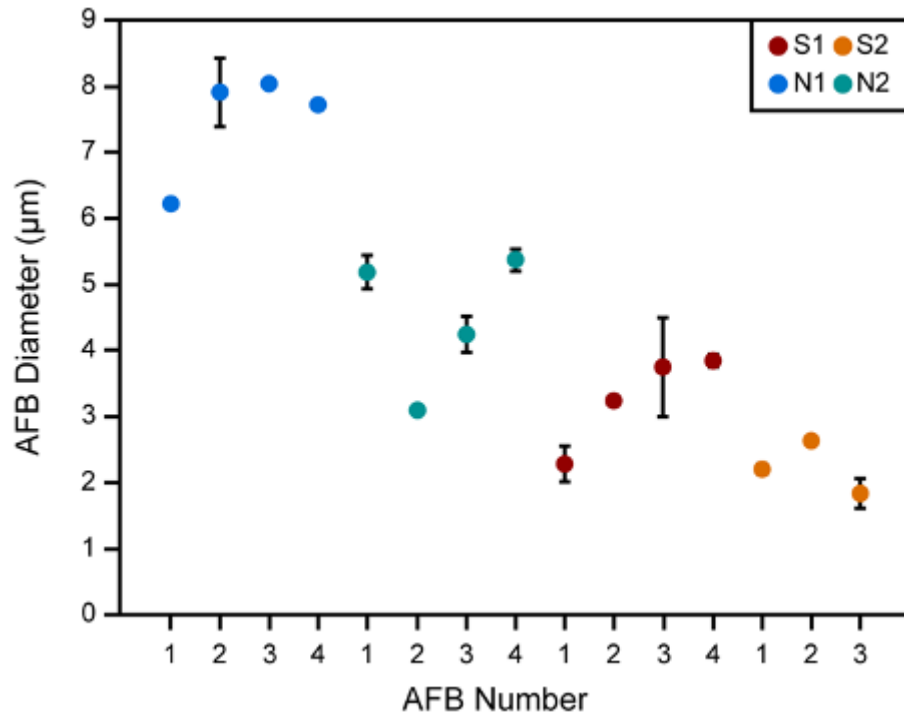
Figure 5. A representation of the diameters of AFBs from all patients analysed here. The spot represents the average value calculated from two measurements, one of the longest diameter and one of the shortest diameter, while the ends of the error bar indicate the highest and lowest diameter values. Note that for AFBs that were almost perfectly circular, error bars are not present. The values were measured using the TEM DF images shown in Fig. 2 and the supplementary materials. N1 and N2 are non-smoking patient N1 and N2 and S1 and S2 are smoking patient S1 and S2, respectively. AFB number refers to the number used to identify the AFB that is used throughout the thesis.

Smoking patient S2

AFB 1 (Figure A13 of the appendix) had a fibre with a long diameter of 0.32 µm and a short diameter of 0.19 µm, AFB 2 (Figure A14 of the appendix) had no fibre, which had possibly been dislodged during the FIB processing, and AFB 3 (Figure A15 of the appendix) presented 3 fibres with long diameters between 0.18 and 0.26 µm and short diameters between 0.06 and 0.07 µm. AFB 1 had an initial dense layer surrounding its fibre, followed by several porous layers. AFB2 had an initial dense layer around the area where the fibre would have been, after which a porous halo-like ring was present, followed by a series of dense layers. AFB 3 had a porous layer surrounding its fibres, followed by a dense layer. The AFBs had long diameters between 2.07 and 2.69 µm and short diameters between 1.61 and 2.59 µm.

2.3.3 Fibre stoichiometry

The mineral composition of each asbestos fibre from all AFBs studied here was determined through fibre stoichiometry calculations[87]. Table 2 shows that grunerite (amosite) with the formula $Fe^{2+}_7(Si_8O_{22})(OH)_2$ was determined in all AFBs of non-smoking patient N1 and smoking patient S1 and in one AFB from non-smoking patient N2. The rest of the fibres of the AFBs from the non-smoking patient N2 and all fibres of the AFBs from smoking patient S2 were riebeckite (crocidolite) asbestos, with the formula $Na_2Fe^{2+}_3Fe^{3+}_2(Si_8O_{22})(OH)_2$. The stoichiometry results from the analysed asbestos fibres were compared with asbestos fibre from the literature[88–93] in order to confirm their mineral nature.

2.3.4 TEM-EDS analysis

Table 3 shows the results of the semi-quantitative chemical analyses of the AFBs of non-smoking patient N1 and the AFBs and fibres of non-smoking patient N2 and smoking patients S1 and S2. Figure 6 shows the chemical distribution of Fe in each AFB from all patients. Plots for the rest of the analysed elements are shown in figures A1-A15 of the appendix. Note that the EDS analytical software automatically normalises the analysis results to 100%, meaning that the data is semi-quantitative.

The AFBs had higher abundances of Fe, P and Ca than the asbestos fibres, while the asbestos fibres had higher Si abundances than the AFBs. Moreover, the averages of Fe and Si in the AFBs were anti-correlated, with smoking patients having lower abundances of Si and higher abundances of Fe than non-smoking patients (Fig. 7). The AFBs sometimes showed a correlation between Fe and P, as it was often the case that when Fe was low, P was low as well. This might have been a consequence of probing a porous area, resulting in low elemental concentrations. However, the average values of Fe and P in the AFBs showed no correlation, the only relationship being the higher Fe concentrations in the AFBs of smoking patients compared to those of non-smoking patients.

Table 3: EDS elemental quantification (wt. %) of NS-AFB (AFBs of non-smoking patients N1 and N2), S-AFB (AFBs of smoking patients S1 and S2) and S-fibre (asbestos fibres of AFBs of non-smoking patient N2 and smoking patients S1 and S2).

|		O	Mg	Al	Si	P	Ca	Mn	Fe
N1-AFB	Mean (n=4)	28.8 ± 1.88	0.76 ± 0.25	1.49 ± 0.39	6.18 ± 2.97	1.73 ± 0.35	1.79 ± 0.38	0.11 ± 0.11	59.14 ± 4.82
	Min	25.49	0.19	0.4	1.37	0.94	0.91	0	34.06
	Max	38.67	1.63	3.58	22.41	2.69	3.70	0.45	67.96
N2-AFB	Mean (n=4)	28.70 ± 3.04	0.73 ± 0.23	1.41 ± 0.4	6.37 ± 4.75	1.53 ± 0.34	1.58 ± 1.19	0.48 ± 0.16	59.20 ± 7.96
	Min	25.47	0.00	0.27	1.16	0.09	0.49	0.00	5.01
	Max	50.82	1.72	4.90	41.45	2.70	14.97	1.20	67.84
S1-AFB	Mean (n=4)	27.08 ± 1.6	0.58 ± 0.36	1.03 ± 0.34	4.19 ± 3.51	1.76 ± 0.34	1.99 ± 0.59	0.08 ± 0.1	63.13 ± 5.45
	Min	25.36	0.17	0.03	1.48	0	0.14	0	31.14
	Max	40.19	2.83	3.61	26.07	2.25	3.93	0.65	67.75
S2-AFB	Mean (n=3)	27.23 ± 1.28	0.64 ± 0.24	1.30 ± 0.53	4.16 ± 1.7	1.64 ± 0.31	1.50 ± 0.55	0.10 ± 0.08	63.43 ± 3.47
	Min	25.58	0.34	0.68	2.31	1.03	0.63	0	51.04
	Max	30.87	1.95	4.21	9.07	2.38	3.28	0.32	68.14
N2-Fibre	Mean (n=4)	41.68 ± 2.46	1.27 ± 0.54	0.09 ± 0.08	28.51 ± 3.95	0.06 ± 0.15	0.66 ± 0.79	0.10 ± 0.10	27.63 ± 5.74
	Min	39.48	0.37	0.00	24.12	0.00	0.08	0.00	11.87
	Max	48.35	2.24	0.32	38.94	0.69	3.59	0.45	33.09
S1-Fibre	Mean (n=4)	37.57 ± 3.55	1.94 ± 0.8	0.2 ± 0.34	21.74 ± 6.07	0.26 ± 0.55	0.45 ± 0.6	0.31 ± 0.22	37.54 ± 8.86
	Min	27.05	0.34	0.00	3.70	0.00	0.06	0.00	22.05
	Max	44.24	2.92	1.11	32.58	2.12	2.56	0.71	64.87
S2-Fibre	Mean (n=3)	41.12 ± 1.88	0.78 ± 0.20	0.13 ± 0.20	27.92 ± 2.66	0.03 ± 0.07	0.28 ± 0.36	0.05 ± 0.04	29.68 ± 4.96
	Min	39.58	0.54	0.02	25.69	0	0.03	0	21.85
	Max	44.02	1.05	0.48	31.93	0.16	0.91	0.09	33.64
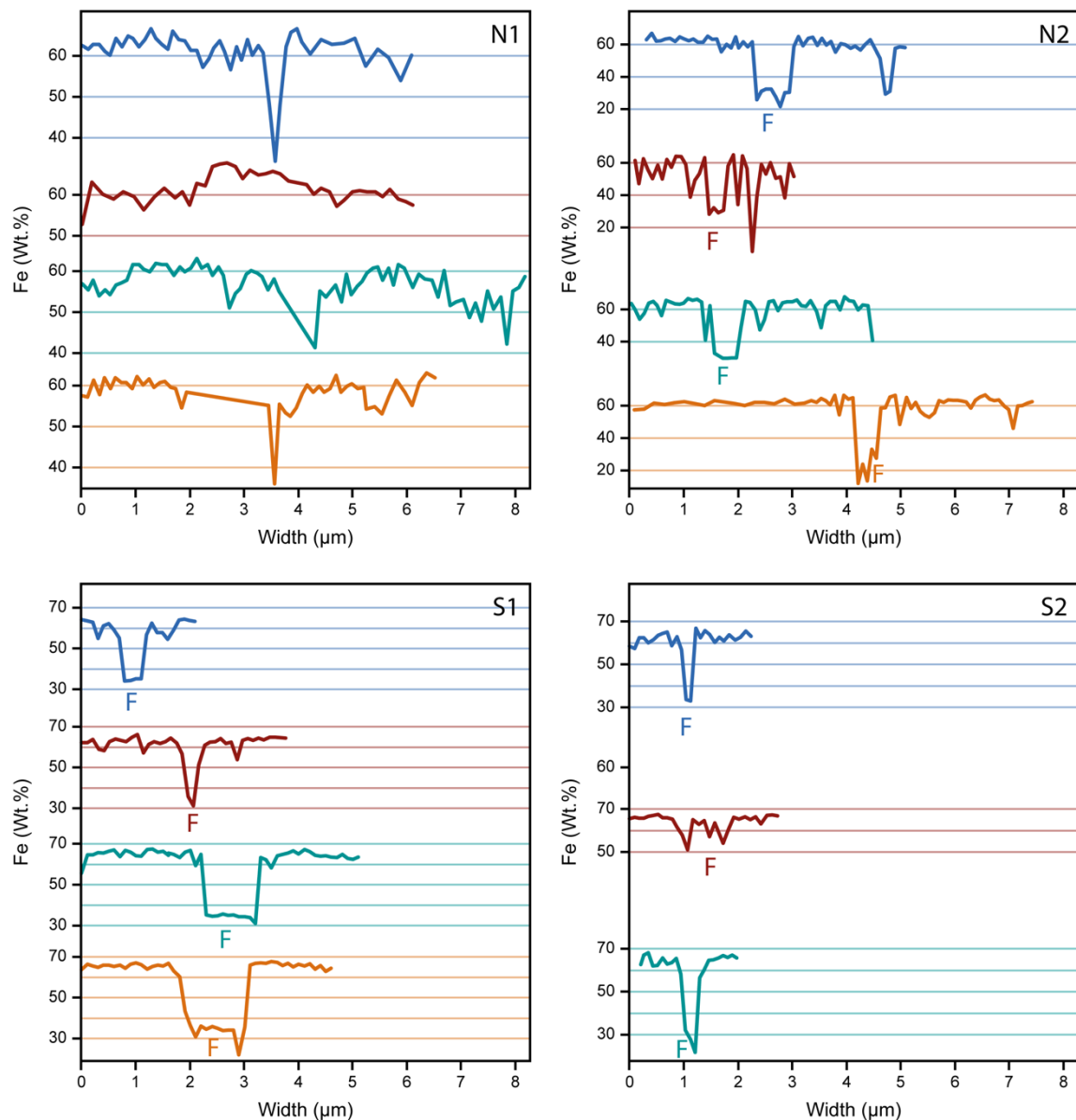
Figure 6. Plots of the Fe concentration from EDS against AFB size for the AFBs from each patient analysed here. F denotes the position of the fibre in each EDS transect. Note that the EDS line analyses of AFBs from patient N1 did not pass through the fibres. N1 and N2 are non-smoking patient N1 and N2 and S1 and S2 are smoking patient S1 and S2, respectively.
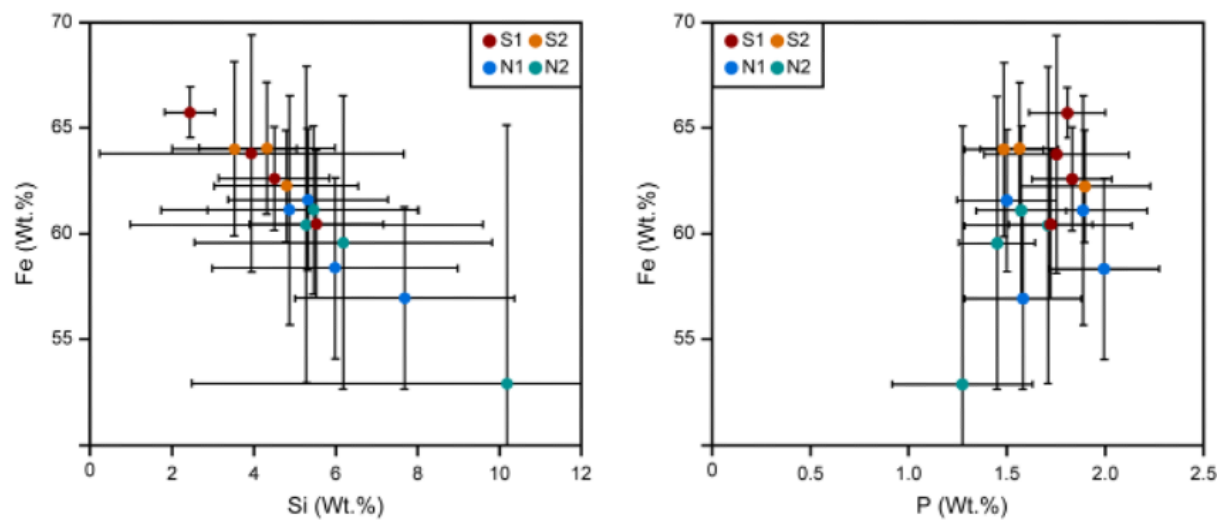
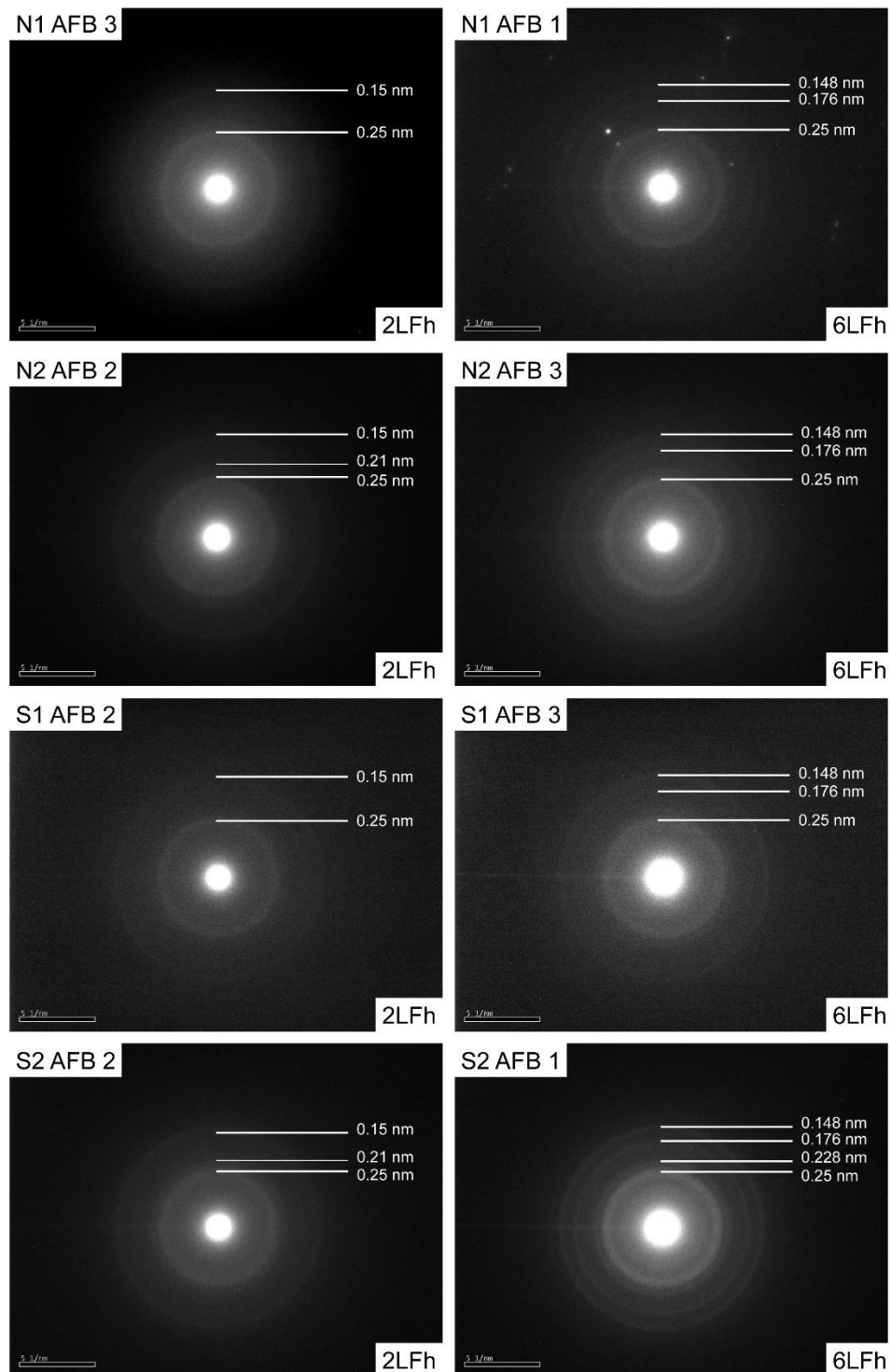Figure 7. Plots of the Si and P concentration against Fe concentration for the AFBs (excluding the fibre) analysed here. N1 and N2 are non-smoking patient N1 and N2 and S1 and S2 are smoking patient S1 and S2, respectively.

Figure 8. Representative SAED patterns for 2LFh and 6LFh from each patient: The white lines with numbers indicate the position of the scattering bands (thick lines) and shoulders (thin lines) in the SAED patterns. N1 and N2 are non-smoking patient 1 and 2 and S1 and S2 are smoking patient 1 and 2, respectively. Note that the 6LFh may be some intermediate phase between 2LFh and 6LFh, due to the lack of 6 strong lines.

2.3.5 SAED patterns of AFB

The observed x-ray diffraction patterns for Fh can be of 2 types depending on the number of visible peaks: one small and less ordered 2LFh and a more crystalline 6LFh[28]. Representative SAED patterns for each patient are shown in figure 8.

SAED patterns were obtained from each layer of each analysed AFB from all four patients. All four patients presented both the characteristic pattern of 2LFh and 6LFh, having no tendencies for either of them. The 2LFh is characterised by two bright rings with d-values of 0.15 nm and 0.25 nm. Some of the SAED patterns had shoulders on both sides or just one side of each ring, such as those indicated by Janney, 2000[28]. While the 2 rings of 2LFh were observed, 6LFh did not have all its characteristic 6 rings. Therefore, some SAED patterns may represent a transition phase between 2LFh and 6LFh. Although AFB 2 of patient S2 had a SAED pattern with 5 clear rings, most likely being 6LFh.

2.4 Discussion

Externally, the AFBs studied showed a texture that resembled an aggregation of several spherical components (Fig. 2d). Following the AFB dissection, the spherical components were also observed within the internal cross-section. The spherical components could not be unaltered macrophages due to their small diameters of 50-170 nm. Koerten et al., 1990[94] observed macrophages with Fe-micelles in the peritoneal cavity of mice previously injected with a suspension of crocidolite fibres. The identified spherical components in this study are within the size range of the Fe-rich inclusions observed by Koerten et al.,1990[94] (~6 nm ->100 nm). As a result, the observed spherical components may be the Fe-rich inclusions from within the macrophages which went through frustrated phagocytosis.

The AFBs studied here had an internal morphology consisting of a series of Fe-rich concentric layers surrounding the asbestos fibres, which varied in density/porosity. The smoking patients had smaller AFBs than the non-smoking patients. The AFBs of the smoking patients were also denser and richer in Fe than the AFBs of the non-smoking patients. Thus, the non-smoking patients had larger and more porous AFBs than the smoking patients. The mean Fe abundance of the AFBs of the smoking patients was 6.5 % higher than that of the AFBs of non-smoking patients. The observations of a previous study align with the aforementioned findings, in which there were higher Fe concentrations for the dry lung tissue of smoking patients (containing AFBs) than that of non-smoking patients[1]. Cigarette smoke (CS) is known for the complexation of Fe, which is deposited as Fh in ferritin[39,43–45].

Fe complexation by CS leads to the increase of Fe availability which explains the denser and richer in Fe AFBs of the smoking patients compared to non-smoking patients. Meanwhile, an overall lower Fe availability during the growth of the AFBs from non-smoking patients might have led to larger and more porous AFBs with a lower overall Fe abundance than AFBs from smoking patients. Furthermore, the AFBs of non-smoking patients were likely formed in an environment that varied in Fe availability over time, due to the presence of many contrasting porous and dense layers, compared to those of smoking patients.

Within ferritin, Fe^{3+} is known to form Fh with minor amounts of Phosphate and Fh is also known to associate with phosphates[95,96]. As such, the presence of P in the AFBs is expected

and is what was observed here. Additionally, phagocytosis by alveolar macrophages (AM) likely causes calcifications[97], which explains the presence of Ca in AFBs. Di Giuseppe et al., 2019[16] conducted TEM analyses on the exterior of AFBs but showed lower Fe concentrations and higher P and Si concentrations than analyses undertaken here. However, due to the lack of any internal investigation, it is impossible to understand whether the AFBs of Di Giuseppe et al., 2019[16] are unique in terms of the overall composition or contain higher amounts of P and Si that have adsorbed to the outside of the AFBs.

The SAED patterns for the studied AFBs were either 2LFh or 6LFh, or possibly an intermediate Fh phase. An amorphous Fh crystal yielded more diffuse rings, while a polycrystalline sample yielded sharper rings. All AFBs had their Fe in the form of Fh, and no other Fe minerals were identified, such as goethite reported by Giuseppe et al., 2019[16], suggesting that the ferritin shell remained intact. Ferritin misfolding leads to the exposure of Fh to the surface, leading to its phase change and contribution to ROS production[16,42]. Having detected only Fh in the AFBs studied here, these events have not occurred.

Aside from ROS, alternative mechanisms, such as inflammation[9,98] or radiation-induced DNA damage[1], can initiate the onset of lung cancer or MM. For the latter hypothesis, AFB bulk analyses have detected Ra concentrations of >1 million times than that of seawater. Fh can adsorb traces of inhaled Ra, accumulating high concentrations within the lung environment over time. The result is the production of Ra hotspots that persist throughout a patient's life. Thus, a patient could have been exposed to large doses of ionising radiation over many years.

Prior to proposing an AFB accretion model, it is important to mention the following information concerning the initial conditions that asbestos fibres are exposed to upon entering the body. Once asbestos fibres are inhaled and deposited in the lungs, AM attempt to phagocytose them, but due to the long length of the fibres and their insoluble nature, the AM fail and allow the fibres to persist within the lungs[7,9,40,98]. The fibres then interact with the lung surfactant, a complex mixture of proteins, phospholipids and mucopolysaccharides with the role of reducing surface tension in the alveoli during breathing. Finally, the fibres and macrophage remnants become coated in the acid mucopolysaccharides, and because acid mucopolysaccharides have an affinity to Fe, association with ferritin and other Fe sources occurs [4,5,7,30–35].

Considering the literature and the presented observations, the following AFB formation accretion model is proposed (Fig. 9). The inhaled asbestos fibres are phagocytosed by AM, as they are recognised as foreign pathogens (Fig. 9a-b). Failure of phagocytosis due to the long length and the insoluble nature of the fibres leads to frustrated phagocytosis[7,98] (Fig. 9c). Following the death of AM on the fibres, AM lose their membrane integrity and release their internal components onto the surface of the fibres which include sequestered ferritin with scavenged Fe[9,29,37,98] (may be Fe inclusions[94]). The persistence of the fibres in the lung environment leads to their coating with lung surfactant phospholipids and proteins, and acid mucopolysaccharides[4,5,29–35] (Fig. 9d-e). The latter are known for their Fe affinity, thus, they mobilise and accrete ferritin and Fe on the fibre surface (Fig. 9f-g), leading to the irritant factors being masked and halting membrane damage[34,97,99]. Therefore, due to the initial immune response, porous layers immediately form around the fibres, initiating AFB formation. The damage caused by the fibre within the lung environment may influence the size of the initial porous layer, as well as specific features of a given patient's immune system, which dictate the initial severity of the immune response.

After the formation of the initial porous layers in the non-smoking patients, AM with ferritin and scavenged Fe and lung surfactants, including mucopolysaccharides, accrete on the asbestos fibres and act to mask them. Fe accretion from the neighbouring lung environment is increased by the acid mucopolysaccharides. As a result, the fibre is masked by the accretion of dense layers, resulting in avoidance of the immune system and a diminished immune response. Nonetheless, the AFB growth continues, attracting AM and Fe-rich lung components (Fig. 9h-i). The Fe concentration at that time determines whether a subsequent accreted layer is porous or dense (Fig. 9j). Moreover, initiation of a further immune response could occur due to lung tissue damage caused by fibre movement within the lung environment, resulting in further porous layers.

A more pronounced Fe mobilisation[37,39,43–45] in smoking patients is achieved through the Fe complexation of CS, resulting in a continuous source of Fe for the AFBs. Therefore, smoking patients undergo the formation of denser layers within their AFBs and have smaller AFB diameters (Fig. 9k) compared to non-smoking patients. Furthermore, the presence of more porous layers in the non-smoking patients (Fig. 9l) yields larger AFBs than those of the smoking patients because the presence of porosity results in a greater volume for a similar amount of accreted material.

Based on the reported findings, AFBs develop differently in smoking and non-smoking patients. It is not yet understood how these differences impact the initiation of cancer and MM. However, if denser AFBs occur more often in smoking patients than in non-smoking patients, the larger amounts of Fe could lead to an increase in ROS production and, consequently, the risk of developing cancer. On the other hand, the dense layers rich in Fh could provide a larger surface area for Ra adsorption and thus elevated radiation levels for smoking patients in comparison to non-smoking patients, as in the radiation-induced DNA damage[1] hypothesis. While CS has not been proved to be a factor in the development of asbestos-related MM, in patients exposed to asbestos and CS had a multiplicative effect in terms of the risk of developing lung cancer. Since the onset of lung cancer could be affected by differences in the AFB morphology between smoking and non-smoking patients, an unknown factor could also influence MM, such as a short latency period, which should be further investigated.

2.5   Conclusion

Several AFBs from 2 smokers and 2 non-smokers were investigated regarding their external and internal morphology. Previous studies showed similar external morphological features. However, internal morphology revealed differences between the AFBs of smokers and non-smokers. The AFBs of smokers were denser and more Fe-rich than those of non-smokers.

The study suggested a Fe-poor porous layer containing lung components accreted due to an initial immune response. During frustrated phagocytosis, macrophages containing ferritin and Fe-rich inclusion created as a result of asbestos inhalation were deposited on the fibre. Following the initial immune response in smokers, the fibres were at least partially masked from the immune system, leading to a more stable accretion of Fe due to complexation by CS and mucopolysaccharides. However, the Fe-rich inclusions were still present, indicating that the fibres were not fully masked from the immune system, so frustrated phagocytosis was also a continuous Fe supplier to the AFBs. Regarding non-smokers, Fe concentration and availability varied over time, resulting in less-Fe rich, dense and porous layers, and larger

AFBs.

SAED data of the internal areas of the AFBs revealed only 2LFh and 6LFh. No other phases were observed, as was the case in previous studies, which analysed only the exterior of the AFBs. If other Fe phases were present, this would have suggested that the ferritin shell was not intact, and the protein had become misfolded. As such, the Fh could have been exposed to the lung environment. Meanwhile, an intact ferritin shell should have prevented Fh from interacting with the lung environment and forming ROS. Therefore, another mechanism for MM might be more plausible, such as DNA damage due to ionising radiation from adsorbed Ra.

The AFBs of smokers were found to be more Fe-rich than non-smokers and thus may have adsorbed higher amounts of Ra, leading to a higher radiation dose. While no previous studies found a relationship between smoking and asbestos-related MM development risks, there have been observations regarding a relationship between smoking and asbestos inhalation in lung cancer development. Such an observation is difficult to explain and requires further investigation. It may be the case that smoking influences MM in some manner, which has yet to be determined.
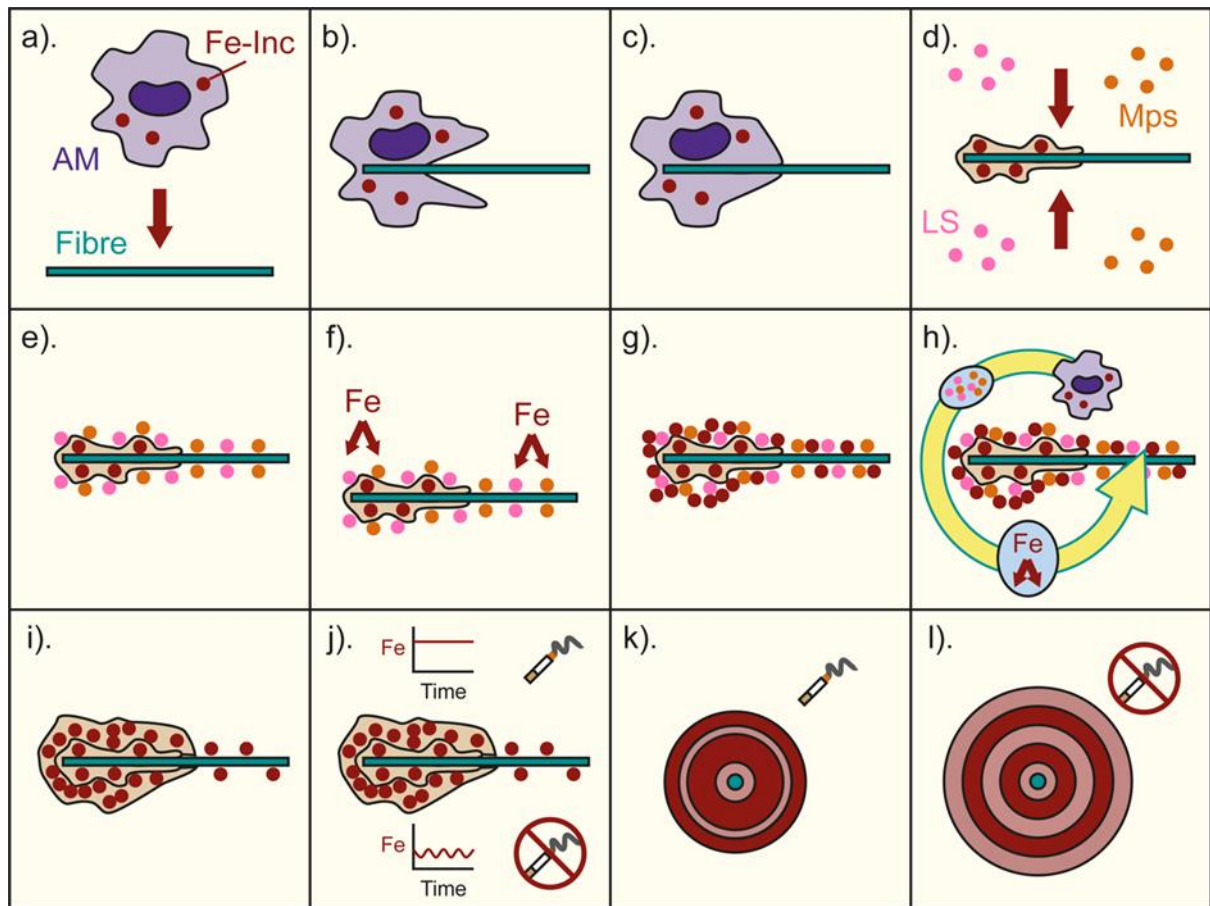
Figure 9. An illustration of the AFB formation model is described here. **A**. asbestos fibres are introduced into the lung environment, and AM containing Fe-rich inclusions respond as part of the body's immune response. **B**. the AM attempt to engulf the asbestos fibre. **C**. the AM cannot fully engulf or break down the asbestos fibre, undergo frustrated phagocytosis, and die. **D**. the Fe-rich inclusions and other AM material (including ferritin) are deposited on the fibre's surface, initiating AFB formation. However, the number of Fe-rich inclusions is limited, and other sources of Fe are not yet available, resulting in an initial porous layer. Subsequently, the asbestos fibre and deposited AM material are exposed to lung surfactants (LS) and acid mucopolysaccharides (Mps). **E**. the lung surfactants and acid mucopolysaccharides coat the fibre and AM material. **F**. Fe from the lung environment is attracted to the acid mucopolysaccharides on the fibre. **G**. the Fe is adsorbed onto the surface of the asbestos fibre and AM material, Initiating the formation of a dense layer surrounding the initial porous layer. **h**. repeated cycles of AM frustrated phagocytosis and Fe accumulation through adsorption result in the growth of the AFB. **i**. an example of an AFB consisting of the initial porous layer and subsequent denser layer. **j**. After continued growth, the AFBs of smokers and non-smokers differentiate due to the smoker receiving a higher and more stable supply of Fe and the non-smoker receiving a variable and, on average, a lower supply of Fe. **k**. an example of a cross-sectional view of a smoker's AFB, with darker red indicating a dense layer and light red a porous layer. **l**. an example of a cross-sectional view of a non-smoker's AFB, with dark red indicating a dense layer and light red a porous layer.

37

3. CHAPTER 3 – ICP-MS analysis of MM samples

3.1 Summary

Previously, inductively coupled plasma mass spectrometry (ICP-MS) was used to quantitatively measure the elemental concentrations of major and minor elements, rare earth elements (REE) and ^{226}Ra[1]. The phosphate groups within ferritin are able to co-precipitate with elements such as Cd, and REE such as La and Ce which are genotoxic for the lungs. The aim was to reveal possible factors contributing to asbestos toxicity and cancer progression.

While Nakamura et al., 2009[1] quantitatively measured the elemental abundances of 6 lung samples (Fig. 11), the analysis has not been reproduced since. Therefore, the ICP-MS analyses were repeated to evaluate the reproducibility and investigate the possibility of a sample bias in the procedure. As seen in figures 11 and 12, the analyses of Nakamura et al., 2009[1] and the current study differed especially in the number of lung samples where Ra was detected, the former detecting Ra in 6 out of 6 samples, while the latter detecting Ra in 2 out of 6 lung samples. The 2 lung samples in which Ra was detected were of smoking patients, suggesting significant enrichment of Ra associated with smoking. The discrepancies between the past study and the current study were found likely to be the result of sampling bias caused by the heterogeneity in the ratio of AFBs to lung remnants within the sample aliquots.

3.2 Materials and Methods

3.2.1 Machines

ICP-MS utilises a high-temperature plasma, which generates, and discharges positively charged ions. The high-temperature plasma represents a chemically inert environment, which is present during ionisation. As such, the formation of oxides is prevented, and the analytes are efficiently ionised.

The sample for the ICP-MS analysis must be in a liquid state. Firstly, in the ICP-MS machine, the liquid is pumped by a peristaltic pump into a nebuliser, where it is nebulised by argon gas. The nebulisation results in a fine aerosol which is separated from larger droplets in the spray chamber and then transferred through a sample injector within the plasma torch. In the plasma torch, argon gas continuously flows, which is ionised by a spark from a magnetic field generated by a radio-frequency coil. The spark leads to a very high-temperature plasma (~6000°K), which remains constant for the duration of the analysis[100,101].

The fine aerosol is atomised upon entry into the high-temperature plasma, through drying into solid particles, followed by sublimation as a result of the heat. The resulting atoms are ionised by releasing an electron as they travel through the plasma. Following ion production, the ions are guided towards the MS by an interface region, which connects the ICP and MS. The interface region consists of a sampler and skimmer cones that suitably adjust the pressure and temperature of the ionic gas for MS analysis.

Afterwards, the ions are filtered according to mass either in a quadrupole (iCAP TQ), passing through its charged metallic cylinders or by a magnet (Element XR) where the ion path

curves as it passes through it based on its mass to charge ratio and magnetic field strength. Ions of the mass-to-charge ratio of interest are kept from diverging, while any unnecessary ions are filtered out. Finally, the ions reach the detector, the most common detector being a dynode detector of 26 dynodes. When ions strike the active surface of the first dynode, an electron is released for each ion struck. Subsequently, the electron strikes the second dynode, and more electrons are released, leading to a cascade of electrons as more dynodes are struck until it results in a measurable electronic signal at the last dynode. The signal is processed by the data handling system and converted into concentration through the use of calibration standards[100,102,103]. The ICP-MS machines used for analysis in the current study are the Element XR High resolution ICP-MS (HR-ICP-MS) and the iCAP triple quadrupole (TQ) ICP-MS.

3.2.2 Sample preparation

The lung sample aliquots utilised for ICP-MS analysis were from the same bulk lung samples as those used in SEM and TEM analyses. For drying the sample, 1 ml of the sample was pipetted into a quartz glass crucible, then covered with a quartz glass lid and introduced into a furnace at $110°C$ for 2 hours. Subsequently, ashing was undertaken of the proteins within the final product (residue) at $500°C$ for 3 hours.

The next step involved double leaching of the sample in order to split loosely fixed elements from strongly integrated ones within proteins without causing asbestos decomposition. First, the ashed sample was transferred to a tube with 3 ml of 0.06 M HCl and put into an ultrasonication bath for agitation (20 minutes). Following ultrasonication and centrifugation at 4,500 rpm for 20 minutes, the supernatant, labelled as leachate 1 (L-1), was collected. To the remaining residue, 3 ml of 1M HCl were added, and the same procedure as before was followed. The resulting supernatant was removed and labelled as leachate 2 (L-2), while the solid material left in the final tube from which the supernatant was extracted was labelled as residue. Finally, 0.6 ml of HF and 0.3 ml of $HClO_4$ were added to the two leachates and residue, followed by agitation in an ultrasonic bath for 24 hours. A schematic diagram of the leaching process is shown in figure 10.

The sample was then submitted to acid digestion using a modified version of method C by Yokoyama et al. 1999[104] involving 3 stages: 1. Acid addition with HF and $HClO_4$, heating and 3 drying steps, 2. Acid addition of $HClO_4$, heating and 3 drying steps, and 3. Acid addition of HCl and drying. Following acid digestion, the samples were dissolved in 3 ml of HNO3 and subjected to an isotope dilution-internal standardisation method (ID-IS) using ICP-MS[105]. The method involved adding a spike enriched in ^{149}Sm. ID was used to determine the Sm concentration, while the trace element concentrations were calculated using the ^{149}Sm intensity as an internal standard. Finally, the major and minor element concentrations were calculated using Sr as an internal standard, previously determined with the trace elements.

3.2.3 ICP-MS analytical procedures

As in Nakamura et al., 2009[1], 4 analytical sessions were devised for the current study and these were based on element groupings: trace elements A (Li, Be, Rb, Sr, Y, Ba, La, Ce, Pr, Nd, Sm, Eu, Gd, Tb, Dy, Ho, Er, Tm, Yb, Lu, Pb, Th and U), trace elements B (Cd, In, Tl and Bi), major and minor elements (Na, Mg, Al, P, K, Ca, Sc, V, Mn, Fe, Co, Ni, Cu, Zn and Ga) and ^{226}Ra. The iCAP TQ ICP-MS was used to simultaneously determine trace elements

A and B. For trace elements B, a solution rich in Mo was also analysed in order to reduce the interference of MoO over Cd, using the method described in Makishima et al., 2011[106]. Afterwards, Element XR HR ICP-MS coupled to an Aridus, a desolvating nebuliser system, was used to determine ^{226}Ra together with a diluted solution of the National Institute for Standard and Technology (NIST) 4966 ^{226}Ra solution as the standard. Also, Element XR HR ICP-MS was used to determine major and minor elements. A medium mass resolution (m/Δm=3000) was used for Na, Mg, Al, P Ca, V, Mn Fe and Co and a high mass resolution (m/Δm =7500) was used for K, Sc, Ni, Cu, Zn and Ga. The standard used for these analyses was JB-3, the concentrations for which are available in Makishima and Nakamura,2006[105].
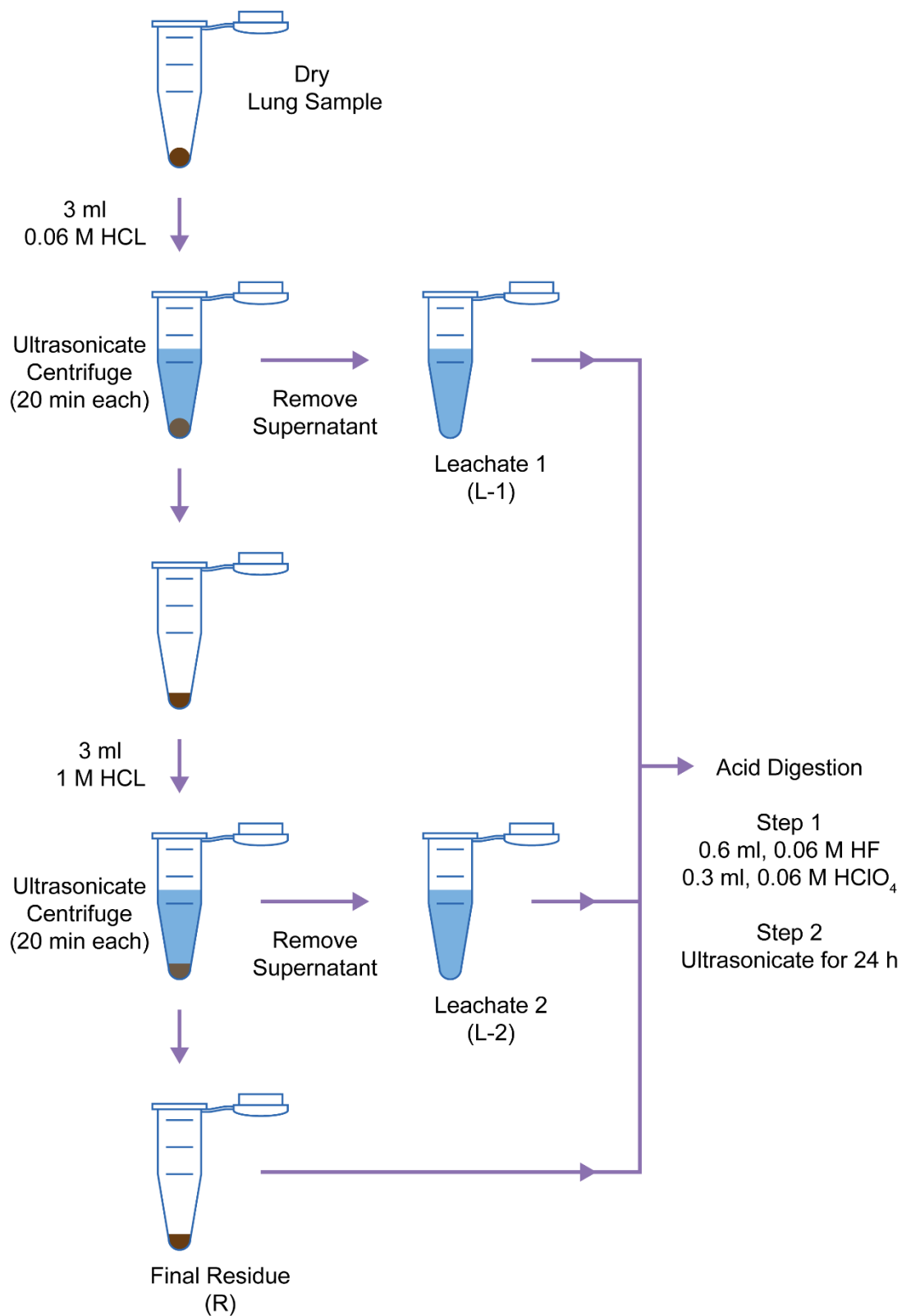
Figure 10. Acid leaching procedure prior to acid digestion for ICP-MS analysis

3.3 Results

Six bulk lung samples containing AFBs and fibre-free ferruginous proteins were analysed for 44 elements. Fe and P were included which are known to be major components of AFBs. For better concentration estimations, the results from L-1, L-2, and bulk (L-1+ L-2+ residue) were normalised to 60 wt. % Fe concentration which was previously determined during TEM analysis in AFBs. Furthermore, the results were normalised once to the elemental abundances of the hypothetical Earth's primitive mantle[107], which is the whole silicate Earth composition after core formation (PM-normalised), in order to facilitate concentration comparisons. Figures 11 and 12 show trace elements and overall elemental abundance patterns of all 6 patients for L-1, L-2, and bulk, done by Nakamura et al., 2009[1] and by this current study, respectively.

The PM-normalised patterns showed high abundances of Ra, Ba, U, Pb, P, Cd and Zn, while REE abundances showed a pattern of decreasing abundances, similar to Nakamura et al., 2009[1]. The highest abundances are for light REE, followed by middle REE. The high abundances persist throughout all patterns, with the highest abundances present in L-1, which can be explained by a higher amount of leached protein material than L-2. There is some variability among patients in L-2, which can be explained by different fractions of ferritin and haemosiderin proteins leached from the samples. Bulk elemental abundances resemble those of L-1. An extremely high abundance of Gd was observed in patient K due to an anomaly caused by a Gd-rich contrasting agent used in the magnetic resonance imaging system.

3.4 Discussion

The most important finding is the detection of ^{226}Ra within 2 out of the 6 lung samples analysed in this study (0.24-3.60 ppb) (Fig. 12). These 2 samples are from smoking patients, which might indicate a significant enrichment of Ra associated with smoking. Previously, Nakamura et al., 2009[1] found ^{226}Ra within 6 out 6 lung samples from the same patients (Fig. 11). The reason for the discrepancy in the results reported here and those reported previously may relate to a sampling bias due to how the samples were stored and how the aliquots were obtained. The lung tissue was dried and suspended in a liquid, meaning that each aliquot taken from the suspension can record slightly different compositions, depending on the level of heterogeneity in the elemental and isotopic compositions between individual suspended particles. Furthermore, different amounts of suspended particles should have been removed with each aliquot, even though the volume of the solution removed was the same. As such, it is likely that the previous study of the 6 lung samples recorded the compositions of more ^{226}Ra enriched solid material or a more significant number of particles.

^{226}Ra is the 5th daughter nuclide of the ^{238}U- ^{206}Pb decay chain, having a half-life of 1600 years. In turn, ^{226}Ra α-decays into ^{222}Rn, emitting a high energy of 4.871 MeV, followed by α-decay to ^{218}Po and ^{214}Po, which in turn α-decays to ^{210}Pb and finally to ^{206}Pb[66]. Thus, ^{226}Ra is a radioactive element capable of causing ionising radiation through the emission of α-particles and consequently causing genotoxicity. Therefore, ^{226}Ra might have an important role in the aetiology of MM.
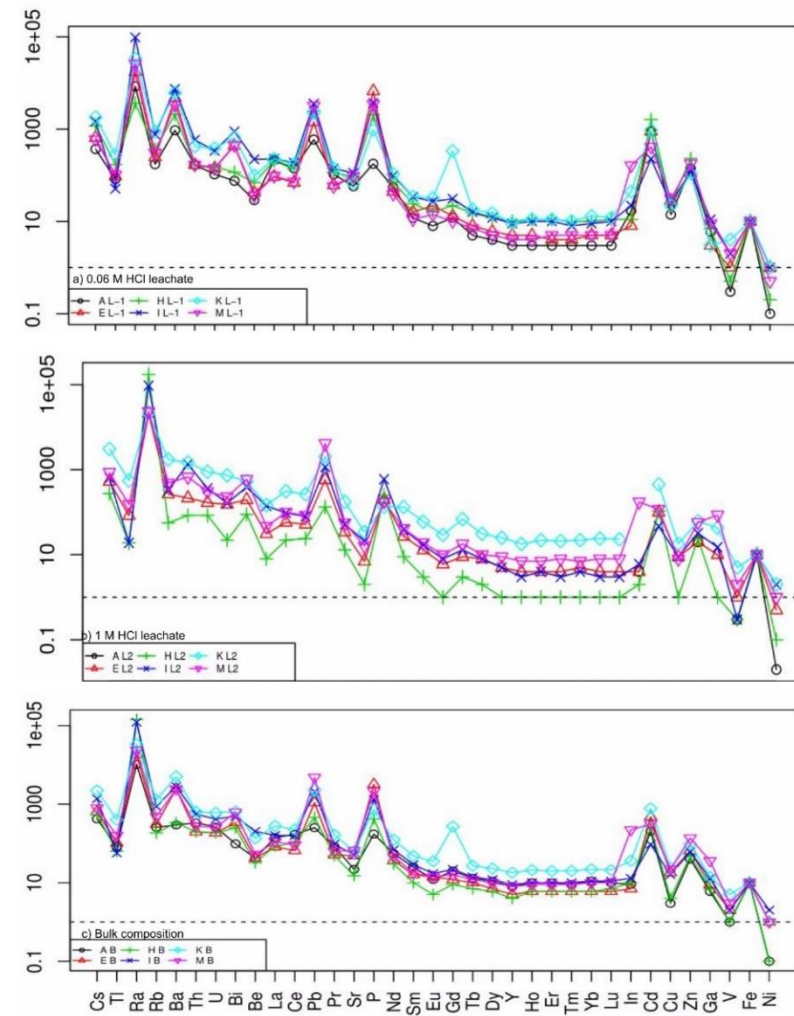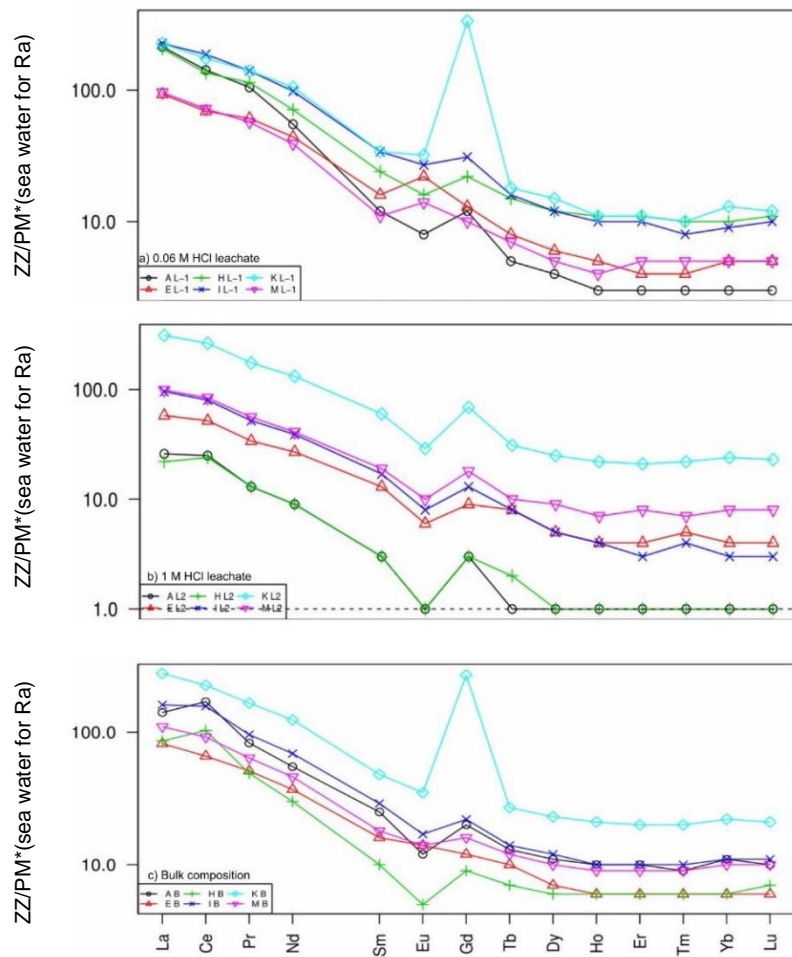
Figure 11. PM-normalised trace element patterns for 6 MM patients[1]: a. First leachate with 0.06 M HCl b. Second leachate with 1 M HCl and c. Bulk composition (a+ b+ residue). The trace elements are ordered by their incompatibility to the silicate mantle, decreasing from left to right. Prior to PM normalisation, the elemental abundances were normalised to 60 wt. % Fe concentration determined in TEM analysis of AFBs.
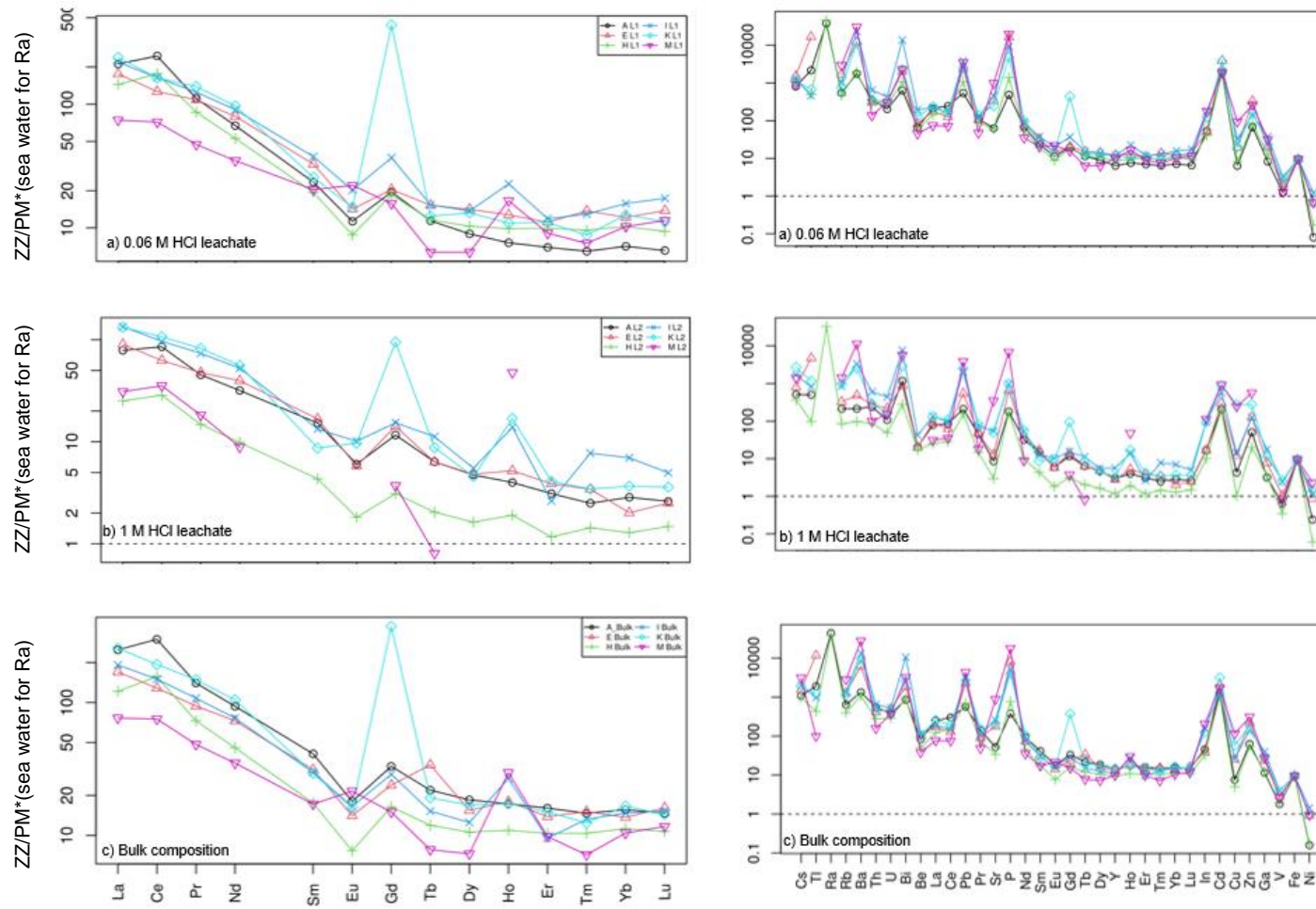
Figure 12. PM-normalised trace element patterns of this study for 6 MM patients: a. First leachate with 0.06 M HCl b. Second leachate with 1 M HCl and c. Bulk composition (a+ b+ residue). The trace elements are ordered by their incompatibility to the silicate mantle, decreasing from left to right. Prior to PM normalisation, the elemental abundances were normalised to 60 wt. % Fe concentration determined in TEM analysis of AFBs.

44

Sampling bias was further observed in the abundances and distribution of REE, as well as of Ba, U, Bi, Pb, P and Cd. As in Nakamura et al, 2009[1], an initial light REE abundance was observed in L-1. However, the heavy REE had little variation in this study than in the past study where the heavy REE variation was more significant. Interestingly, this study had higher Ba abundances than the past study, therefore it was expected to observe high Ra abundances, Ba often being treated as an analogue for Ra[108]. Nevertheless, Ra was detected in only 2 out of 6 samples and U had lower abundances, which strengthened the existence of sampling bias. Another observation possibly caused by sampling bias is an enrichment of Bi in this study, which was shown to promote oxidate stress in the lower lung regions[109].

P is known to associate with Fh[110] which explains the higher P abundances in this study than the previous study. The high P abundances might hint towards a higher enrichment in Fh and ferritin, further supported by higher enrichments of Pb, Cd and U, which are known to bind to Fh[57,61,111,112].

As previously mentioned, the higher abundances of other elements can be plausibly explained by their binding affinity to various substrates that are thought to compose the AFBs. For instance, U and Cd are known to have a high binding affinity to ferritin[58,59]. Furthermore, ferritin can form ionic and organic complexes within its cavities[113], explaining the high abundances of Cd and Zn that form such complexes[61,114]. Since Fh is present within the AFBs due to being housed within the ferritin, this Fe hydroxide can also contribute to the yield of some of the high abundances. Adsorption onto Fh was investigated and proved for Ra, Ba, Pb, Cd, and Zn[58,61,63,65,108,115]. It was found that Zn has no association with lung cancer risk[116]. However, it was found that the co-existence of P and Cd benefits the immobilisation of Cd[58,65]. As such, in addition to ^{226}Ra, some other elements are known to be toxic, such as Pb, Cd and U, are likely present within AFBs[58,59,61,64,65,113,114]. U and Ra are radioactive elements which emit α-particles that cause genotoxicity within the lungs and irreversible DNA damage[66]. Cd is a known human carcinogen which causes single-strand DNA breaks, inhibits apoptosis and DNA repair, and activates proto-oncogenes through genotoxic mechanisms, increasing lung cancer risk[116,117]. Most REE and Pb are known to have genotoxic properties through their involvement in reactive oxygen species formation[53,54,118].

3.5   Conclusion

Genotoxic elements such as Pb, REE and, most importantly, radioactive [226]Ra and U were detected in MM patients. Due to the adsorption properties of Fh, AFBs are the most likely reservoir of such elements. The detection of [226]Ra in MM patients showed that ionising radiation might be an essential factor in the development of MM. The discrepancy in results between Nakamura et al., 2009[1] and this study, such as this study detecting Ra in 2 out 6 patients, while the previous study detected Ra in all patients, might be due to heterogeneity of the lung tissue sample. However, the 2 patients were smoking patients from which Ra was detected in the current study, indicating that the significant enrichment of Ra in AFBs might be due to smoking. The lung tissue sample was suspended in liquid which meant that each aliquot could yield different ratios of AFB and lung remnants and thus different Ra concentrations. The presence of highly genotoxic and/or radioactive elements suggests that DNA damages which leads to cancer cells and tumorigenesis have a role in MM incidence. Accordingly, in situ analysis of trace elements, including [226]Ra, was necessary to assess the potential impact of these elements more definitively on the initiation of cancer and MM in particular.

4. Chapter 4 - Development of a highly sensitive Ra detection protocol

4.1 Summary

Previously, abundant elements detected in the bulk analysis, such as ^{226}Ra, rare earth elements (REE), Pb, Cd and U, are known to be toxic to the human body[58,59,61,64,65,113,114]. ^{226}Ra and U are radioactive elements which emit α-particles that cause genotoxicity within the lungs. Cd is a known human carcinogen which causes single-strand DNA breaks and inhibits apoptosis and DNA repair leading to increased lung cancer risk[116,117]. Most REE and Pb are known to have genotoxic properties through their involvement in reactive oxygen species formation[53,54,118].

However, bulk analyses of lung tissues cannot prove that AFBs are the specific source of the carcinogenic elements reported because other lung components were included. As such, in situ analysis was required, which was undertaken here using secondary ion mass spectrometry (SIMS).

A ferrihydrite (Fh) standard creation and a mounting protocol were established through which vacuum stable and homogeneous standards were created. Two Fh standard series were created, for REE and Ra analysis, respectively. With the newly created standards, the analytical conditions for REE analysis and Ra analysis were established. In addition, the background signal for the ^{226}Ra$^+$ signal was quantified.

An AFB mounting protocol was developed which was used to provide enough AFB material for SIMS analysis, on a micrometre scale. The Fh standards with Ra and the mounted AFBs were analysed using the established Ra analytical conditions, resulting in the detection of Ra in AFBs. For the ^{226}Ra$^+$ signals that were above 3σ of the previously quantified background signal, Ra concentrations were calculated. Based on the calculated Ra concentrations, localized effective doses of AFBs were estimated and a radiation hotspot model was drawn.

4.1.1 Secondary ion mass spectrometry

SIMS uses a primary ion beam to generate secondary ions from a sample. The most common primary beam species are O$^-$ and Cs$^+$, which greatly enhance the yield of electropositive and electronegative species, respectively. A typical SIMS consists of a primary beam source, several electrostatic lenses and deflectors, an electrostatic energy filter, a mass filter, and a detection system.

A sample surface held at a potential of 10 kV is hit by a primary ion beam with an impact energy of -23 keV, transferring kinetic energy to target atoms through nuclear collisions. The collisions displace the target atoms on the sample surface, which can then transfer a portion of their energy to other target atoms, a process known as the collision cascade. In order to be ejected from the sample, the target atoms need to accumulate enough momentum and kinetic energy to overcome the surface potential barrier. Since the energy is obtained from collisions, the emitted atoms have low energies of a few eV. As a result, the majority of ejected particles are neutral, and only a small fraction is in an ionised state. Furthermore, the production of secondary ions results in the sputtering of the sample, leading to a flat bottom and square-shaped sputter craters when the primary beam scans over the sample surface.

The immersion lens 5 mm from the sample extracts the secondary ions, which are then focused into a secondary beam onto the mass spectrometer slit or aperture by the transfer lens. The transfer lens also assists in projecting the secondary ions onto an image detector to visualise the sample surface. The immersion lens and transfer lens together form the Cameca ion microscope.

Subsequently, the secondary ions pass through the electrostatic energy analyser, where lower energy ions are more strongly bent than higher energy ions. The inner and outer sector electrodes of the analyser have voltages of opposite polarity to one another, their respective polarity depending on that of the secondary ion beam.

Afterwards, a mobile energy slit intercepts the high-energy polyatomic ions, denying them passage into the magnetic analyser so that only monoatomic ions are allowed to pass. In cases where the energy of polyatomic ions is high enough to be intercepted together with the monoatomic ions, the energy filtering technique is used to reduce their energy. The energy filtering technique involves lowering the accelerating voltage, known as the voltage offset, which results in reduced ion intensities for both monoatomic and polyatomic ions, the effect being stronger for polyatomic ions. Accordingly, a middle ground between a sufficient ion intensity for a monoatomic ion of interest and low enough polyatomic ion intensities, which can represent potential inferences, can be achieved.

The next step involves the ion beam passing through the mass analyser. The most commonly used mass analyser is the magnetic sector. As the ions pass through the magnetic field applied perpendicular to the direction of the motion of ions, it deflects their trajectory in the form of an arc. The radius of the arc is inversely proportional to the mass of each ion. Therefore, variation in the magnetic field strength allows focusing on ions of different masses.

The entrance and exit slits surrounding the magnetic sector allow only ions of a mass-to-charge ratio of interest to pass through. Therefore, the width of these slits determines the mass resolution power of the magnetic sector. A high mass resolution (HMR) is used to reduce mass interferences by separating signals of the same supposed mass. The mass resolution is set by decreasing the slit width, which at the same time also decreases the secondary ion transmission to the detector.

The combination of an electrostatic and magnetic sector is known as a double-focusing instrument. Such an instrument compensates for the chromatic aberrations in energy dispersion caused by the magnet that lowers mass resolution by adjusting the energy of the electrostatic sector. This way, a higher mass resolution is obtained despite the existence of the mass dispersive properties of the magnet.

After mass filtering of the secondary ions with the mass-to-charge ratio of interest, the number of delivered ions per unit time of these ions is recorded and quantified by a detector, which converts this value into an easily relayed intensity, usually of counts per second (cps). Most SIMS instruments have more than one detector, the most common being a Faraday cup (FC) and an electron multiplier (EM). In this study, only the EM detector was used.

The EM detector comprises a series of electrically isolated metallic electrodes called dynodes. When a particle hits the first dynode, it produces a few secondary electrons, which are accelerated into the second dynode, where more secondary electrons are produced. The generation of secondary electrons continues through collisions with further dynodes until a

cascade of secondary electrons occurs. The resulting current is converted into a voltage by a high impedance multiplier, which in turn is converted by a voltage/frequency converter into a signal that can be measured in cps units.

Imaging analysis with 64x64 pixel resolution and a 20x20 µm raster was used in both trace element and Ra analyses in order to observe the distribution of ions within the AFBs and disregard any possible noise[119,120].

4.1.2   Design of reference Fh materials

In order to determine the elemental abundances of a sample using SIMS analysis, a standard with the same matrix as the sample needs to be created and analysed prior to the sample. The AFBs mainly consist of Fh; thus, Fh-based standards are required for AFB analysis. Therefore, one Fh standard series was doped with a specific pattern of trace element concentrations to enable quantitative trace element analysis of AFBs, while another Fh standard series was doped with sequential Ra concentrations to allow Ra analysis. In addition, three other standards were created to investigate interference to $^{226}Ra^+$ and the background signal contributing to the $^{226}Ra^+$ mass peak. Three other standards were created: one Fh standard doped with P only, one Fh standard doped with P and Ba, and one Fh standard doped with P and Pb.

4.2   Methods
4.2.1   Synthesis and mounting of reference Fh materials

Initially, Fh standard creation consisted of four steps: 1. the creation of a 2LFh mixture with trace element or Ra concentrations based on the method of Schwertmann and Cornell, 2008[121], 2. drying an appropriate amount of the Fh mixture in an oven at over 500ºC, 3. mounting the dried Fh into an epoxy resin puck and polishing, and 4. evaluation of the standard homogeneity and determination of the trace element yields of the Fh standards by SEM and SIMS. A standard was considered to show heterogeneity when its surface demonstrated different compositional regions in SEM, indicated by the presence of more than one shade of grey during backscattered electron (BSE) imaging and varying chemical abundances during SEM-energy dispersive X-ray spectroscopy (SEM-EDS) and SIMS analysis.

In the initial stages of developing the standard creation protocol, the Fh standard was mounted in a resin puck. However, the resin puck caused poor vacuum conditions in SIMS due to devolatilization, which negatively influenced the analysis results. So, the resin puck was replaced with a 4mm diameter aluminium tube filled with resin which led to improved vacuum conditions. Furthermore, some standards were initially found to be heterogenous, so the method was adjusted to dry the Fh at lower temperatures and for a shorter time since Fh changes phases when exposed to temperatures higher than 500ºC. Accordingly, while observing the final standards by SEM, the standards showed a uniform colour on their surface, so they were deemed homogenous without any further chemical investigation. Through such improvements, the standard creation protocol described at the start of this section was improved to yield homogenous and vacuum stable Fh standards.

Accordingly, the revised protocol consisted of four modified phases: the first step remained as before since the same 2LFh mixtures were used. The second step involved drying the 2LFh mixtures in the evaporator at a lower temperature in order to prevent phase change of the Fh mineral. The Fh mixture was dried into a small solid dark red pellet. A half-drilled aluminium tube of 4 mm in diameter was prepared. For the third step, the aluminium tube was filled with epoxy resin which was left to cure until it achieved a viscous state. The previously dried Fh pellet was fixed upright in the epoxy resin.

Additionally, epoxy resin was used to cover the Fh pellet and left to cure overnight. The next day, the fourth step was undertaken, in which the surface of the mounted Fh pebble and epoxy resin was ultra-microtomed until a substantial surface of the Fh was exposed. Below a more detailed description of the four steps concerning standard creation is given.

The middle to heavy REEs have isobaric interferences. As such, it was necessary to create standards where the REE were separated to avoid these interferences and enable oxide reduction calculations. Accordingly, the ferri-7 (REE) standard series were synthesised, which included three standards (a, b, and c). For example, $^{135}BaO^+$ interferes with $^{151}Eu^+$, so Ba is present in ferri-7-a but not in ferri-7-b, while Eu is present in ferri-7-b but not in ferri-7-a. Thus, the ions detected for $^{151}Eu^+$ in ferri-7-a are that of $^{135}BaO^+$, while in ferri-7-b, they represent only $^{151}Eu^+$ ions. The primitive mantle normalised elemental abundances to have an increasing pattern resembling CI chondrites.

For Ra analysis, a series of five standards with four sequential Ra concentrations and one without Ra was created in order to yield a linear calibration curve. The standards were also doped with Pb at the concentration of patient A to reflect the Pb concentration of AFBs.

The second step involved drying the Fh, which was necessary for mounting the standard into an aluminium tube filled with epoxy resin. It is known that prolonged exposure to high temperatures leads to the phase change of Fh to haematite[122,123]. Previous attempts of drying the Fh involved high temperatures, which led to heterogeneity and other crystal phases, documented through SEM and TEM SAED patterns. Thus, a simplified drying method with limited exposure to heat was developed, as shown in figure 13a. Firstly, 100 µl of the Fh mixture was pipetted into an Eppendorf tube and centrifuged at 10,000 rpm for 1 minute, and the resulting supernatant was removed. The centrifugation and supernatant removal steps were repeated three times. Finally, the resulting Fh liquid was left to dry in the evaporator at 120°C for up to 2 hours, unsealed and covered with a larger cap until it completely dried in the shape of a small dark red pellet.

The third step involved mounting the pellet in semi-cured resin inside an aluminium tube. The semi-cured resin prevented the Fh pellet from sinking to the bottom of the aluminium tube (Fig. 13b). If the Fh pellet sank below the rim of the aluminium tube, ultra-microtoming would not be possible. Therefore, the Fh pellet was set in a position slightly elevated from the base of the aluminium tube, covered with resin, and left to cure overnight.

The fourth step involved the ultra-microtoming process, which was undertaken using a diamond knife. The speed of the knife was set to 1.5 mm/s, with a feed of 1.5 um when ultra-microtoming resin. Meanwhile, the speed was set to 1 mm/s, with a feed of 0.5-1 um when ultra-microtoming the exposed Fh surface.

Before SEM observation, the fully prepared Fh standard was coated with 300 Å of gold. Then, SEM was used to observe homogeneity in terms of morphology and chemical composition. Afterwards, the sample was transferred to SIMS, where its homogeneity, in terms of ion intensities, was observed by surveying 10 spots.

The spot survey was followed by the calculation of secondary ion yields through the division of secondary ion intensity by the elemental concentration of the element of interest obtained through ICP-MS analysis. The secondary ion yield is the number of ions produced per sputtered molecule.
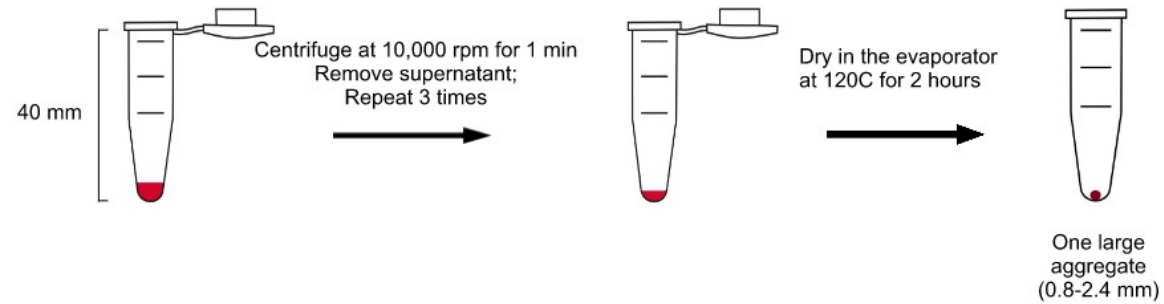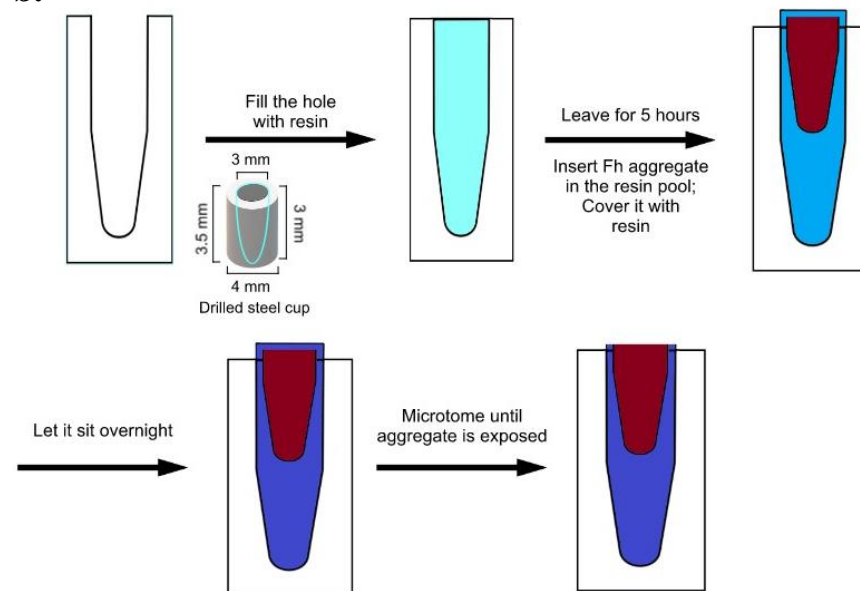
Figure 13. Creation of the Fh standard: a. drying of the Fh, b. mounting in resin and microtoming.

4.2.2 Typical analysis conditions

Analytical conditions for REE determination

Analytical conditions used in spot analysis for both standards and samples are shown in Table 4. The same analytical conditions were used for both standards and samples. The 1 nA beam was chosen for minimal damage and optimal secondary ion yields. 21 isotopes were included in the analysis, $^{30}Si^+$, $^{31}P^+$, and $^{57}Fe^+$ having a short counting time of 5 seconds due to being major elements and having high ion intensities and $^{88}Sr^+$ and $^{89}Y^+$ having a counting time of 10 seconds. The rest of the isotopes had a counting time of 20 seconds. The measurement of $^{30}Si^+$ was performed only on silicate standards to allow mass calibration and beam positioning.

Analytical conditions for $^{226}Ra^+$ determination

Analytical conditions used in spot and imaging analyses for both standards and samples are shown in table 5 and figure 14. The same analytical conditions were used for both standards and samples. In addition, a beam of 1 nA was used in order to prevent rapid erosion of the sample and ensure that enough sample was preserved for a successful analysis.

For the determination of the mass peak of $^{226}Ra^+$, a calibration curve representing atomic weight plotted against the B field value was constructed for a uraninite sample. The atomic weights and B field values of $^{206}Pb^+$, $^{207}Pb^+$, $^{208}Pb^+$, $^{234}U^+$, $^{235}U^+$ and $^{238}U^+$ were plotted in order to determine the B field value of $^{226}Ra^+$. The determined B field value for $^{226}Ra^+$ based on the atomic weight vs B field calibration curve was determined as seen in figure 15. Assuming that the uraninite had a UO_2 concentration of 100 wt. %, the Ra concentration in uraninite was determined by the equilibrium equation $^{226}Ra = \lambda_{238U}/\lambda_{226Ra}*^{238}U$, resulting in 356 ppb.

Table 4. Analytical conditions for trace element analysis

Parameter	Remark
Mass spectrometer	Cameca IMS-1280
Primary impact energy	+13keV
Gold coat	200Å
Primary beam current	~1nA
Raster area	20 μm^2
Pre-sputter duration	180s
Acquisition mode	Spot
Secondary voltage	+10kV
Energy offset	−45eV
Entrance slit width	240 μm
Contrast aperture dimension	400 μm
Field aperture dimension	8000 μm
Energy band pass width	-10 ± 40eV
Exit Slit width	600 μm
m/Δm	2000
Detector	EM
Secondary ion acquisition	(× 5cycles)
$^{30}Si^+, {}^{31}P^+, {}^{57}Fe^+$	5s
$^{88}Sr^+, {}^{89}Y^+$	10s / 40s
$^{137}Ba^+, {}^{139}La^+, {}^{140}Ce^+, {}^{141}Pr^+, {}^{146}Nd^+, {}^{147}Sm^+, {}^{151}Eu^+, {}^{159}Tb^+$	20s / 40s
$^{160}Gd^+, {}^{163}Dy^+, {}^{165}Ho^+, {}^{167}Er^+, {}^{174}Yb^+, {}^{175}Lu^+, {}^{208}Pb^+$	The 20s /40s
Total analysis time	40mins (including pre-sputter duration)
Background correction	was not applied

Table 5. Analytical conditions for $^{226}Ra^+$ and MREE interference analysis

Parameter	Remark
Mass spectrometer	Cameca IMS-1280
Primary impact energy	+13keV
Gold coat	300Å
Primary beam current	~1nA
Raster area	20 μm^2
Pre-sputter duration	50s
Acquisition mode	Spot/Imaging
Secondary voltage	+10kV
Energy offset	0eV
Entrance slit width	77 μm
Contrast aperture dimension	400 μm
Field aperture dimension	4000 μm
Energy band pass width	$-10 \pm 40eV$
Exit Slit width	150 μm
m/Δm	8000
Detector	L2-EM, axial EM/EM
Background correction	was not applied
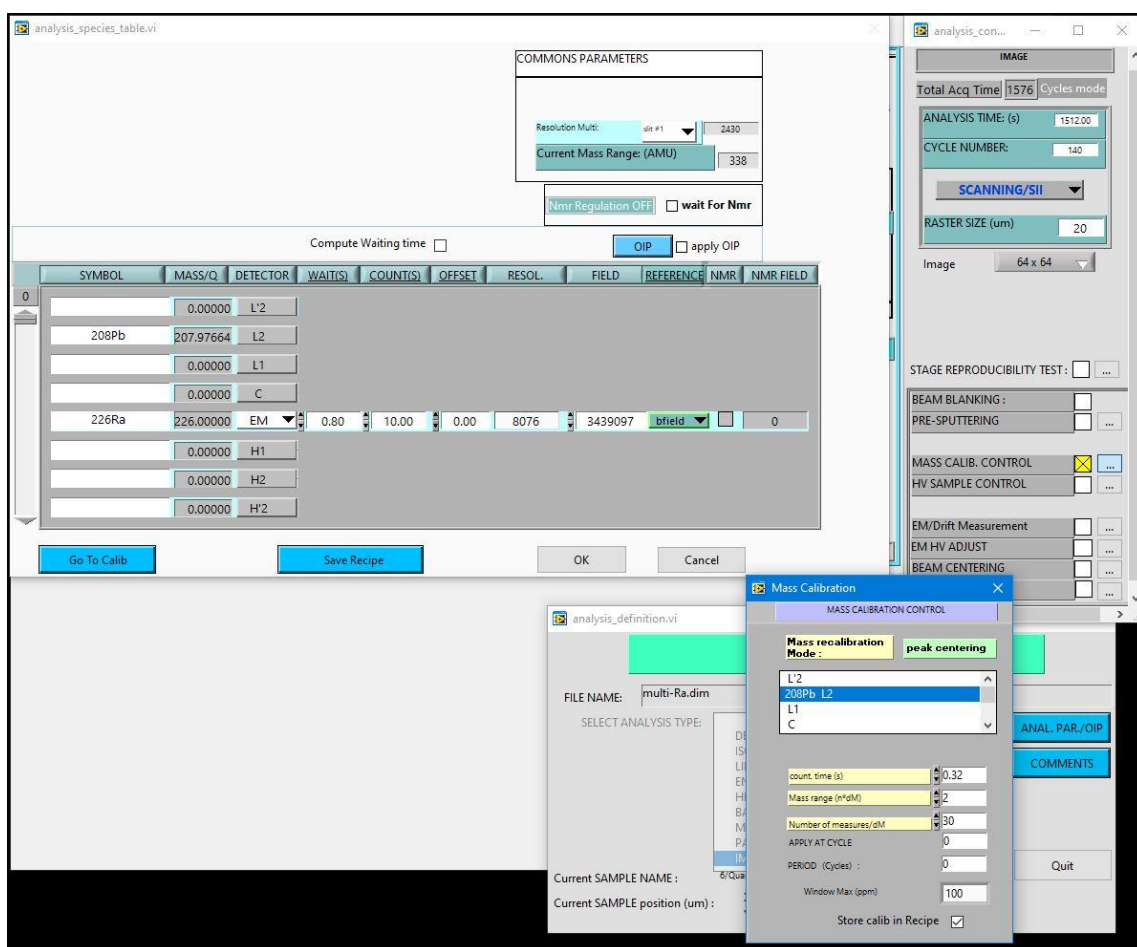
Figure 14. Analysis definition for ^{226}Ra$^+$ imaging analysis: top left. Table denoting analysed isotopes by the multi collector, specifying counting time, waiting time, and b field value; top right. Window denoting cycle number, total acquisition time and raster size of the analysed area; bottom right: Mass calibration control regarding peak centring on ^{208}Pb$^+$, counting time, mass range and the number of measurements.

$$y = -8.39388\ x^2 + 11509.2\ x + 1265710$$
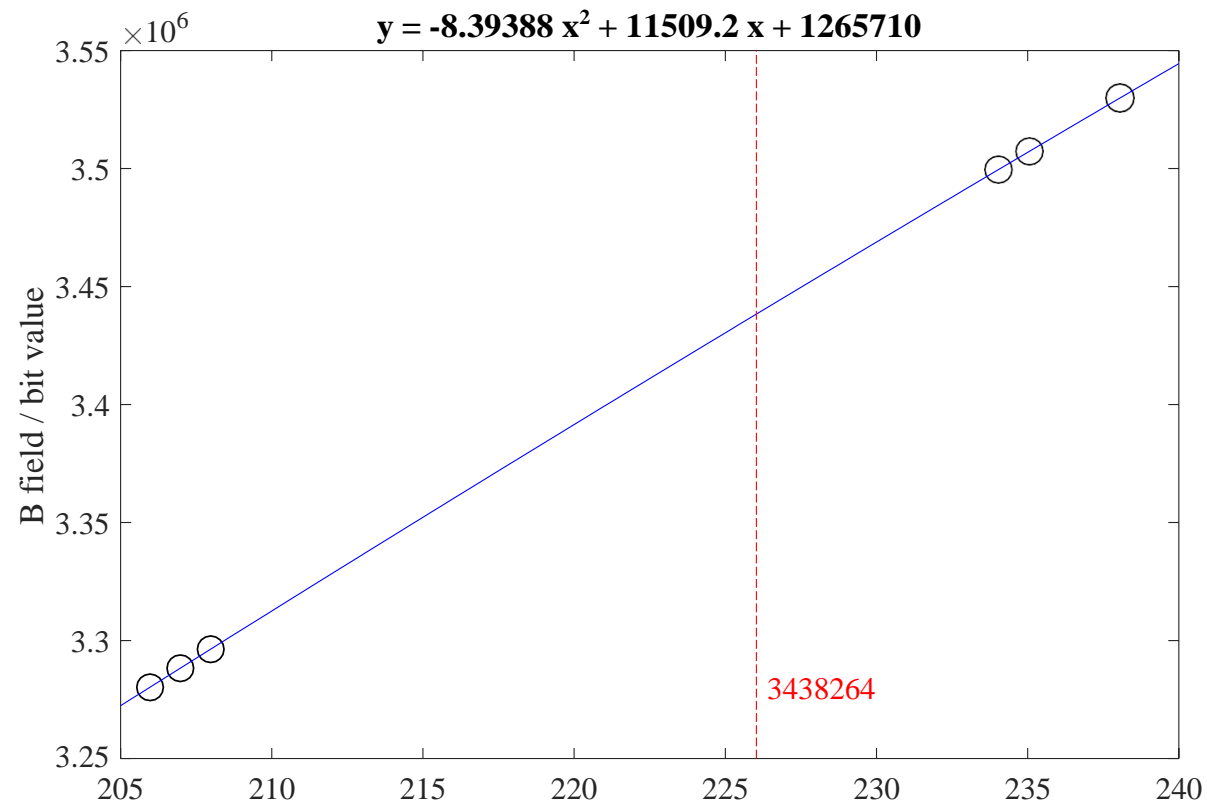
Figure 15. Calibration curve based on the atomic weight and B field values of $^{206}Pb^+$, $^{207}Pb^+$, $^{208}Pb^+$, $^{234}U^+$, $^{235}U^+$ and $^{238}U^+$ for determination of the B field value of $^{226}Ra^+$.

4.3   Results

4.3.1   The concentrations of the Fh standards

After successfully developing a procedure to make homogenous Fh standards, it was necessary to create doped Fh standards. In order to make doped standards, specific concentrations of either trace elements, Ra, P, Ba or Pb, were added to the Fh mixtures. The elemental abundances of the synthesised Fh mixtures were determined by ICP-MS analysis and are shown in Table 6 and figure 16. At this stage, the Fh mixtures were in a viscous state and constantly kept in a refrigerator.

4.3.2   Homogeneity of the Fh standards

There were several attempts to create Fh standards through different methods, eventually leading to the current method. As mentioned before, high temperatures changed the crystal phase of the Fh, leading to heterogeneity (presence of more than one phase) and the measurement of more than one type of chemical composition. The most noticeable way to observe heterogeneity within a Fh standard was different shades of colour (Fig. 17) on its surface by SEM BSE and significant differences in $^{57}Fe^+$ ion intensities between these differently shaded areas.

Based on SEM observations (Fig. 18), all standards presented a homogeneous composition as they had a uniform colour shade across their surface. The grainy texture and straight lines over the standard surface were due to the microtoming process of the diamond knife.

4.3.3   Optimization of SIMS conditions

Energy filtering for REE determination

Energy offset (for energy filtering) and HMR values were decided based on surveys fulfilled for both parameters by analysing the newly synthesised Fh standards. The offset was –45 eV while the mass resolution was m/Δm 2000. In addition, energy filtering was used to reduce the contribution of polyatomic ions to the signal of REE.

HMR for Ra detection

The mass peak of $^{226}Ra^+$ was identified based on the previously determined B field value, as seen in figure 19. An interfering peak preceded the $^{226}Ra^+$ mass peak, which prompted the evaluation of interference reduction methods, namely energy filtering and HMR, for separating the interfering peak from the $^{226}Ra^+$ and reducing the tail contribution of the interfering peak. The interfering peak has a mass of 225.95 which is consistent with $^{208}Pb^{16}OH_2$ with a mass of 225.987. Further evaluation is necessary.

The $^{226}Ra^+$ analysis acquisition and pre-sputter times were determined by analysing the same spot for 600 cycles, each cycle with a counting time of 10 seconds. As seen in figure 20, the $^{226}Ra^+$ intensity signal decreased after 150 cycles (25 minutes). Moreover, pre-sputtering was not implemented. Hence the initial signal had high intensities in both $^{208}Pb^+$ and $^{226}Ra^+$, as seen in figure 21. Therefore, the first 10 cycles (50 seconds) were removed post-analysis. The signal of $^{226}Ra^+$ was much smaller in the Fh standards, small enough to cause difficulties in the mass calibration of the $^{226}Ra^+$ mass peak. Therefore, implementing multi-collector use

was considered, in which the ^{208}Pb$^+$ mass peak was simultaneously aligned with that of ^{226}Ra$^+$. As a result, the ^{208}Pb$^+$ mass peak was detected by the L2 EM, and the ^{226}Ra$^+$ mass peak was detected by the axial EM. In other words, when the ^{226}Ra$^+$ mass peak was not visible for mass calibration, the ^{226}Ra$^+$ mass peak was centred on the visible ^{208}Pb$^+$ mass peak, knowing that they were previously centred simultaneously. Therefore, the ^{208}Pb$^+$ mass peak became a guide for centring the ^{226}Ra$^+$ mass peak in Fh standards, in which the ^{208}Pb$^+$ mass peak was visible since the Pb concentration was at ppm level. An example of a mass calibration of the ^{226}Ra$^+$ mass peak to that of the ^{208}Pb$^+$ mass peak by using a multi-collector is seen in figure 22.

Analysis of ^{226}Ra$^+$ was undertaken by imaging mode using the multi-collector, with a beam of 1 nA, HMR of m/Δm 8000 and raster area of 20 μm^2. Post analysis, a region of interest of 16 μm^2 was selected in the ion image for ion intensity quantification. A region of interest was applied due to the appearance of an ion surge border around the edge of the sputtered area, which was suspected to be due to the gold coating. Furthermore, this ion surge border appeared only when analysing ppb level isotopes, in this case, ^{226}Ra$^+$.

The appropriate interference reduction methods were determined while maintaining high transmission of the ^{226}Ra$^+$ ion signal by evaluating tail contribution and observing how the transmission was affected. Evaluation of the tail contribution on ^{226}Ra$^+$ relied on the tail contribution of ^{208}Pb$^+$. The mass difference between the interfering peak and ^{226}Ra$^+$ was measured for the determination of tail interference of ^{208}Pb$^+$ to the peak at the same distance difference between the interfering peak and ^{226}Ra$^+$ (Fig. 23 - Δm). The mass (208.047) where ^{208}Pb$^+$ interfered did not correspond to any chemical element, so measurement at this mass would reflect only the tail contribution of ^{208}Pb$^+$. Two ratios were considered for evaluation, ^{226}Ra$^+$/interfering peak and interfered peak/^{208}Pb$^+$ with the same analytical conditions as in table 5, except for varying energy offsets and HMR settings and the analysis definition in figure 24.

Before commencing spot analysis, mass spectrums were obtained for each considered energy offset value and m/Δm 8000, and each considered HMR value and 0eV offset. The same general analytical conditions were used as in table 5 and the analysis definition in figure 25.

Moreover, the possibility of MREE interference to ^{226}Ra$^+$ was investigated in a series of spot analyses with the analytical conditions in table 6, including background correction at mass 57.8 and the analysis definition in figures 26 and 27. ^{226}Ra$^+$ was present in the spot analysis of figure 27 as a tool for peak jumping in order to maintain optimum mass cycling for the mass spectrometer magnet. Analysis of ^{226}Ra$^+$ was undertaken separately in the same spot using the previously described imaging analysis protocol in table 5 and figure 14.

Table 6: Elemental abundances of reference materials. The concentrations are normalised to 60 wt% of Fe.

		ferri-7A	ferri-7B	ferri-7C	ferri-0	ferri-8	ferri-9	ferri-Ra0	ferri-Ra1	ferri-Ra2	ferri-Ra3	ferri-Ra4
Na	cg/g	BDL	BDL	BDL	BDL	BDL	BDL	BDL	BDL	BDL	BDL	BDL
Li	ug/g	BDL	BDL	BDL	BDL	BDL	BDL	BDL	BDL	BDL	BDL	BDL
Be	ug/g	BDL	BDL	BDL	BDL	BDL	BDL	BDL	BDL	BDL	BDL	BDL
Mg	ug/g	4.3	1.81	5.53	BDL	13.96	BDL	6.81	12.93	BDL	BDL	16.87
Al	ug/g	23.35	19.1	20.45	BDL	BDL	BDL	14.36	30.65	37.65	89.70	209.73
P	cg/g	3.00	3.08	3.03	3.34	3.26	3.44	3.26	3.06	3.13	3.10	3.03
K	cg/g	0.01	0.02	0.02	BDL	BDL	BDL	BDL	BDL	BDL	BDL	BDL
Ca	ug/g	BDL	37.87	BDL	BDL	BDL	113.4	46.23	BDL	62.52	10.34	28.93
Sc	cg/g	BDL	BDL	BDL	BDL	BDL	BDL	BDL	BDL	BDL	BDL	BDL
V	ug/g	BDL	BDL	BDL	BDL	BDL	BDL	BDL	BDL	0.011	BDL	0.208
Mn	ug/g	8.26	7.66	7.71	6.32	16.72	3.44	7.08	BDL	2.72	2.79	5.59
Fe	cg/g	60.00	60.00	60.00	60.00	60.00	60.00	60.00	60.00	60.00	60.00	60.00
Co	ug/g	0.68	0.58	0.87	1.79	2.02	BDL	0.58	BDL	BDL	0.43	0.48
Ni	ug/g	6.56	7.26	6.22	5.63	3.88	3.29	6.68	4.51	2.80	3.34	5.58
Cu	ug/g	BDL	1.97	1.59	1.59	1.45	1.57	1.84	1.95	1.08	1.52	1.78
Zn	ug/g	BDL	1.47	5.06	21.6	9.81	5.73	26.05	36.10	23.18	6.06	8.27
Ga	ug/g	4.1	5.18	4.07	4.3	3.66	4.32	4.62	4.34	5.22	3.88	4.45
Rb	ug/g	BDL	BDL	BDL	BDL	BDL	BDL	BDL	BDL	BDL	BDL	BDL
Sr	ug/g	203.81	461.14	838.1	BDL	BDL	BDL	BDL	BDL	BDL	BDL	BDL
Y	ug/g	46.1	92.4	181	BDL	BDL	BDL	BDL	BDL	BDL	BDL	BDL
Cd	ug/g	BDL	BDL	BDL	BDL	BDL	BDL	BDL	BDL	BDL	BDL	BDL
In	ug/g	BDL	0.00678	0.00699	BDL	BDL	0.0077	BDL	BDL	BDL	BDL	BDL
Cs	ug/g	BDL	BDL	BDL	BDL	0.0038	BDL	BDL	BDL	BDL	BDL	BDL
Ba	ug/g	1244	0.292	0.473	BDL	303.1	BDL	BDL	44.96	178.28	264.62	1116.79
La	ug/g	130	BDL	0.00483	BDL	BDL	BDL	BDL	BDL	BDL	BDL	BDL
Ce	ug/g	377	BDL	0.00435	BDL	BDL	BDL	BDL	BDL	BDL	BDL	BDL
Pr	ug/g	64.4	BDL	0.00268	BDL	BDL	BDL	BDL	BDL	BDL	BDL	BDL
Nd	ug/g	364	BDL	BDL	BDL	BDL	BDL	BDL	BDL	BDL	BDL	BDL
Sm	ug/g	131	0.00139	0.000542	BDL	BDL	BDL	BDL	BDL	BDL	BDL	BDL
Eu	ug/g	BDL	72.3	0.00327	BDL	0.042	BDL	BDL	BDL	BDL	BDL	BDL
Gd	ug/g	0.146	241	0.00797	BDL	BDL	BDL	BDL	BDL	BDL	BDL	BDL
Tb	ug/g	0.0429	63.2	0.00374	BDL	BDL	BDL	BDL	BDL	BDL	BDL	BDL
Dy	ug/g	BDL	382	376	BDL	BDL	BDL	BDL	BDL	BDL	BDL	BDL
Ho	ug/g	0.0215	105	103	BDL	BDL	BDL	BDL	BDL	BDL	BDL	BDL
Er	ug/g	0.0637	0.0367	312	BDL	BDL	BDL	BDL	BDL	BDL	BDL	BDL
Tm	ug/g	BDL	0.0101	74.9	BDL	BDL	BDL	BDL	BDL	BDL	BDL	BDL
Yb	ug/g	BDL	BDL	394	BDL	BDL	BDL	BDL	BDL	BDL	BDL	BDL
Lu	ug/g	BDL	0.00717	99.2	BDL	BDL	BDL	BDL	BDL	BDL	BDL	BDL
Tl	ug/g	BDL	BDL	BDL	BDL	BDL	BDL	BDL	BDL	BDL	BDL	BDL
Pb	ug/g	20.2	41.2	77.6	1.5	BDL	330.4	35.84	35.38	48.07	47.30	33.19
Bi	ug/g	BDL	BDL	0.00705	BDL	BDL	BDL	BDL	BDL	BDL	BDL	BDL
Th	ug/g	BDL	BDL	BDL	BDL	BDL	BDL	BDL	BDL	BDL	BDL	BDL
U	ug/g	BDL	BDL	BDL	BDL	BDL	BDL	BDL	BDL	BDL	BDL	BDL
Ra	ng/g	0.38	BDL	BDL	BDL	BDL	BDL	BDL	9.32	30.46	47.22	135.04
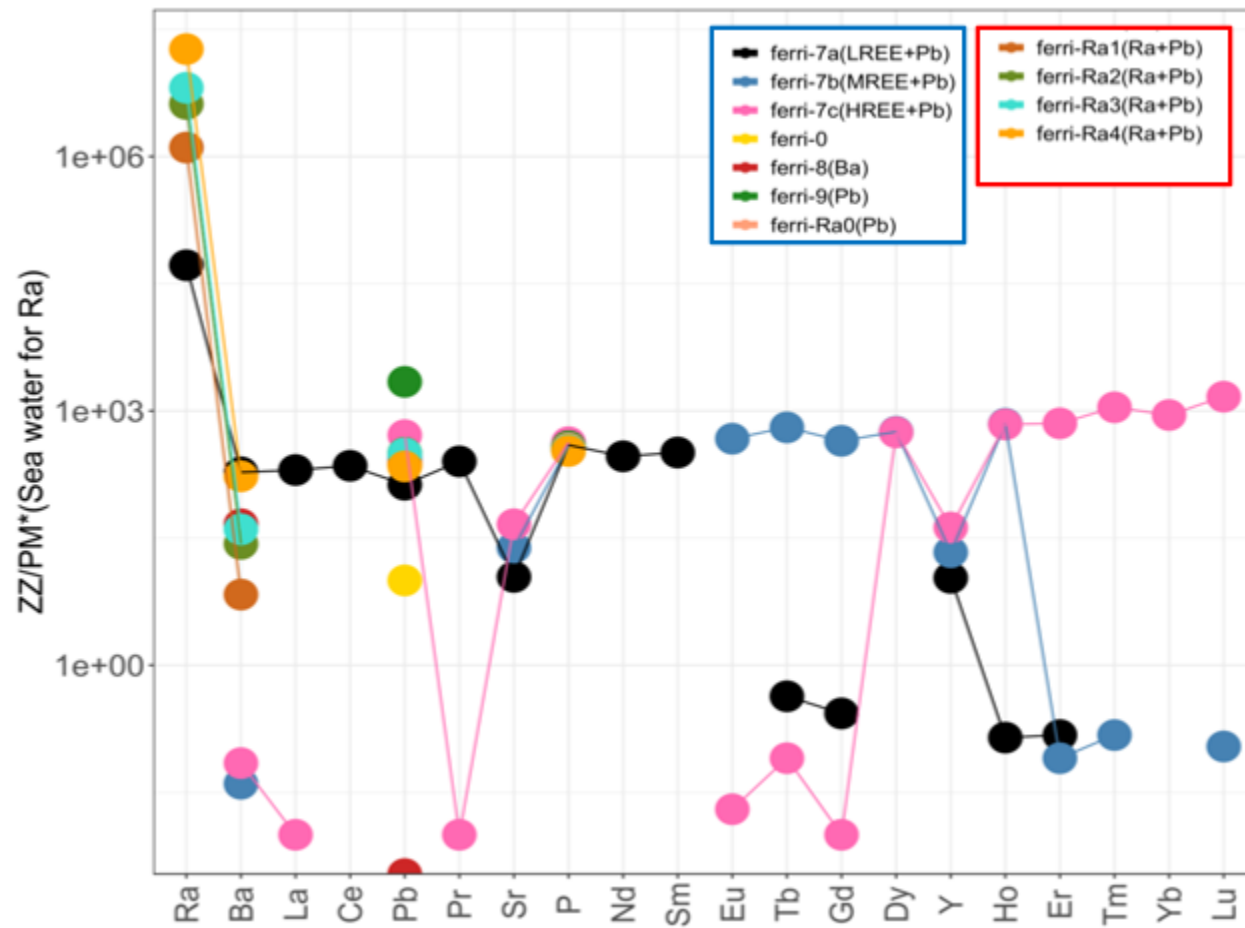
Figure 16. PM-normalised elemental abundances of reference materials: blue rectangle – Fh standards without Ra; red rectangle: Fh standards with Ra.
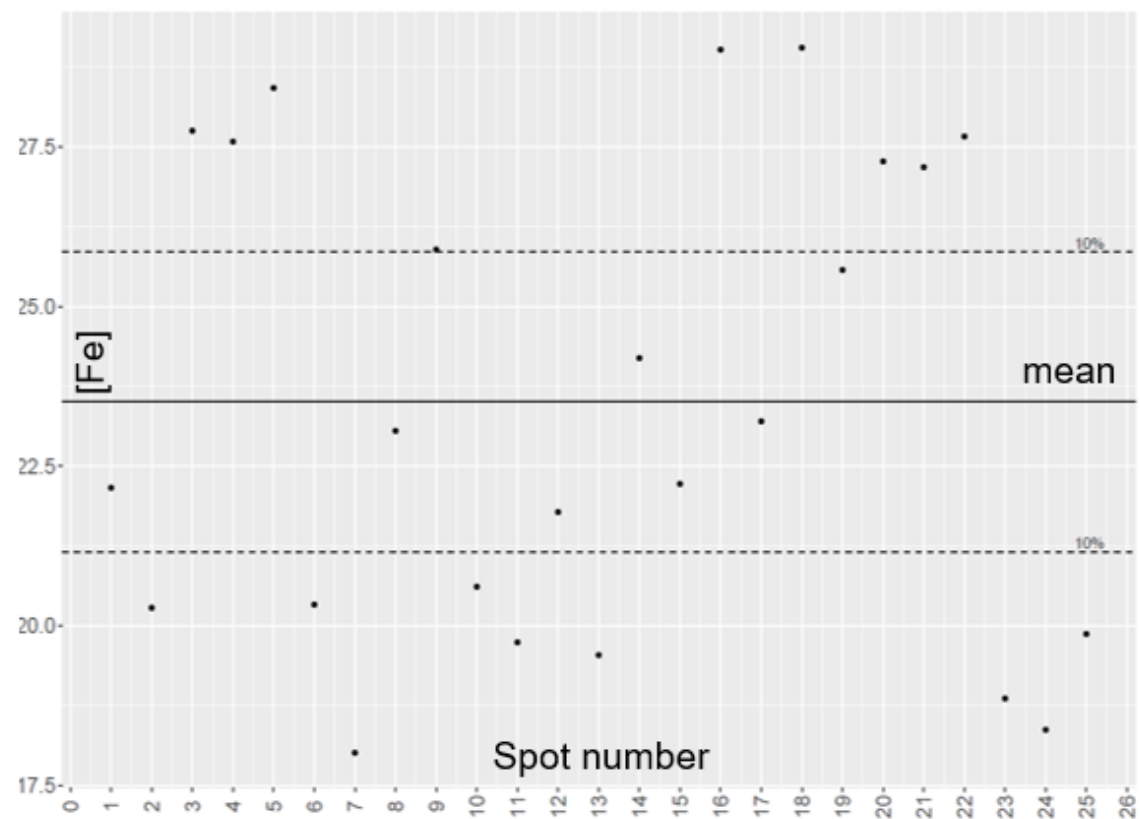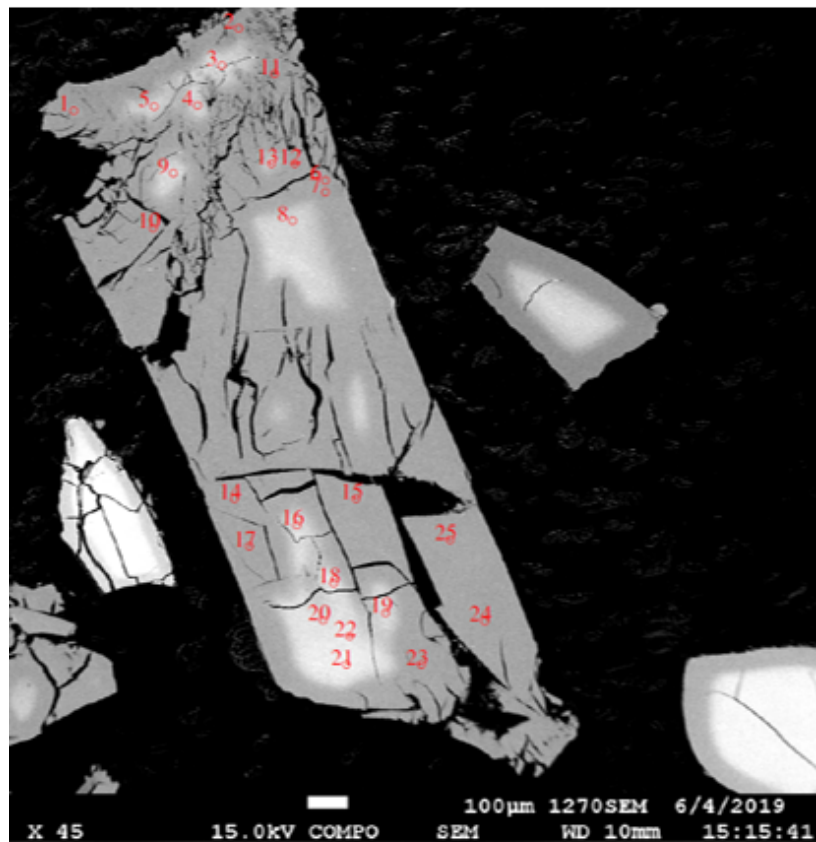
Figure 17. Fh standard created with previous standard creation protocol, which yielded heterogeneous standards, denoted by a. the distribution of bright and dark areas b. the difference in Fe concentration measured by SEM-EDS (e.g., bright spot 4 ~27.5 wt. %, dark spot 11~20 wt.%).
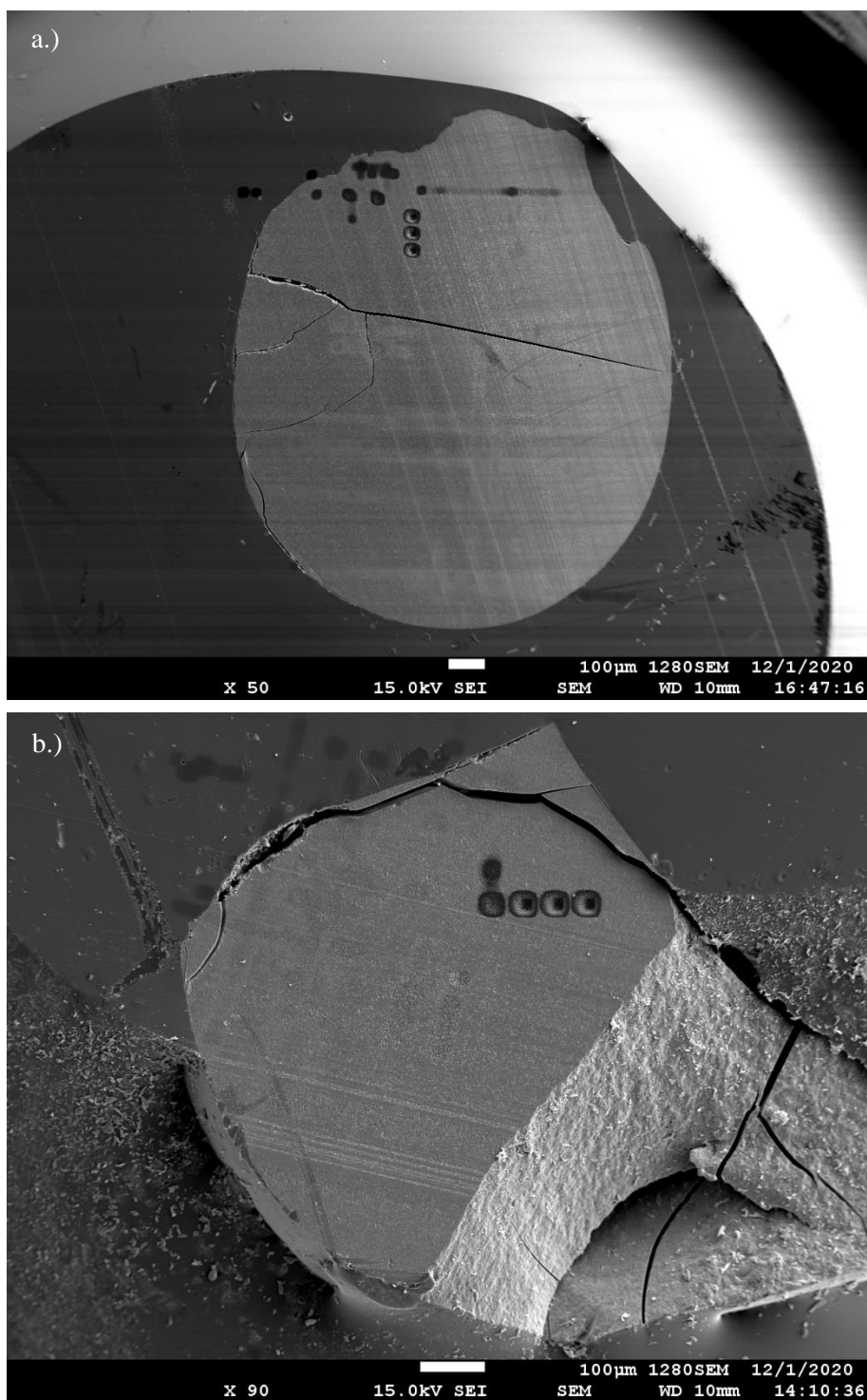
Figure 18. SEM images of the Fh standards: a.) ref-ferri-Ra2 and b.) ref-ferri-Ra0.
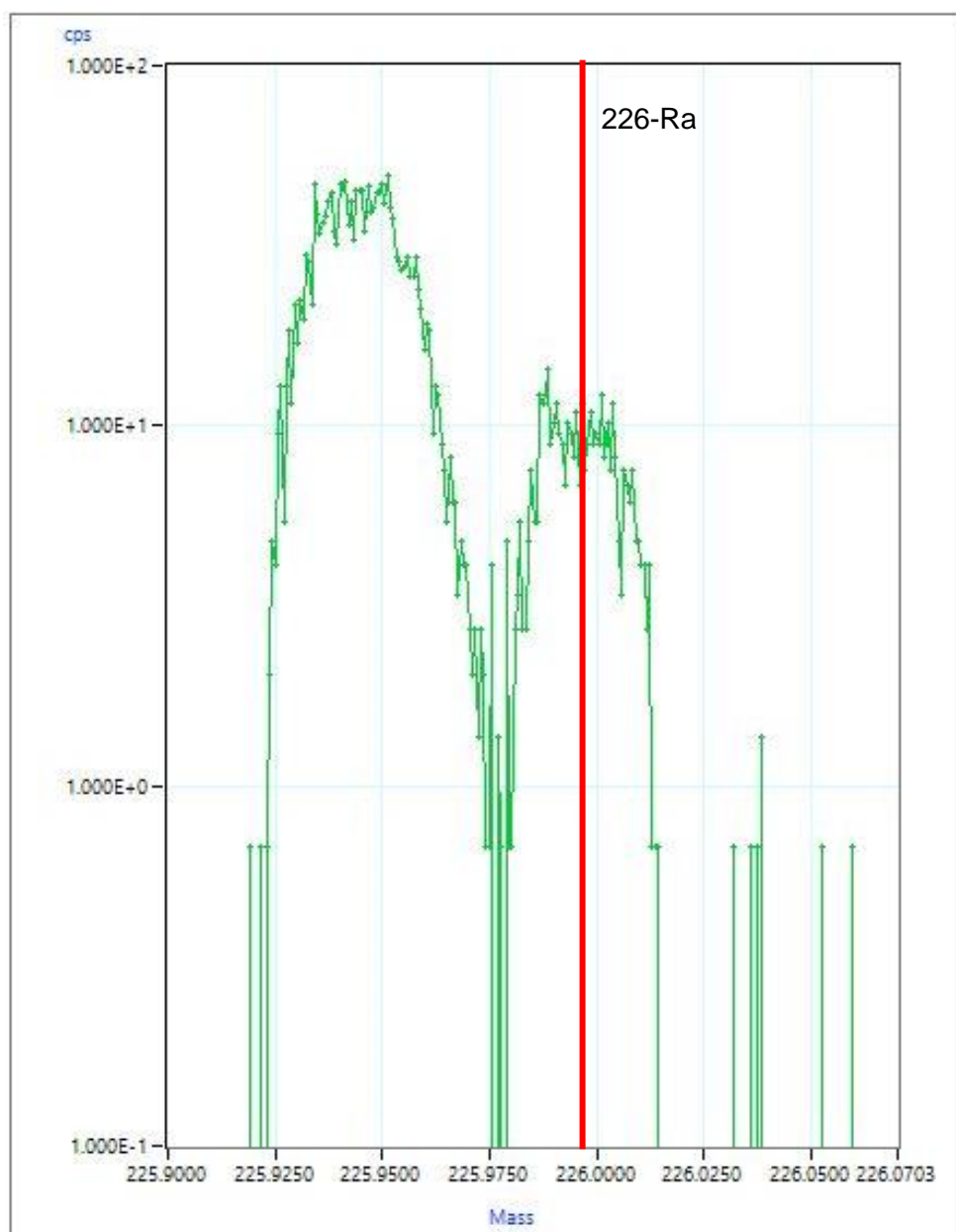
Figure 19. Mass spectrum at m/z=226.025 in uraninite. The right peak is the identified ^{226}Ra$^+$ peak and the left peak is a possible interfering peak.
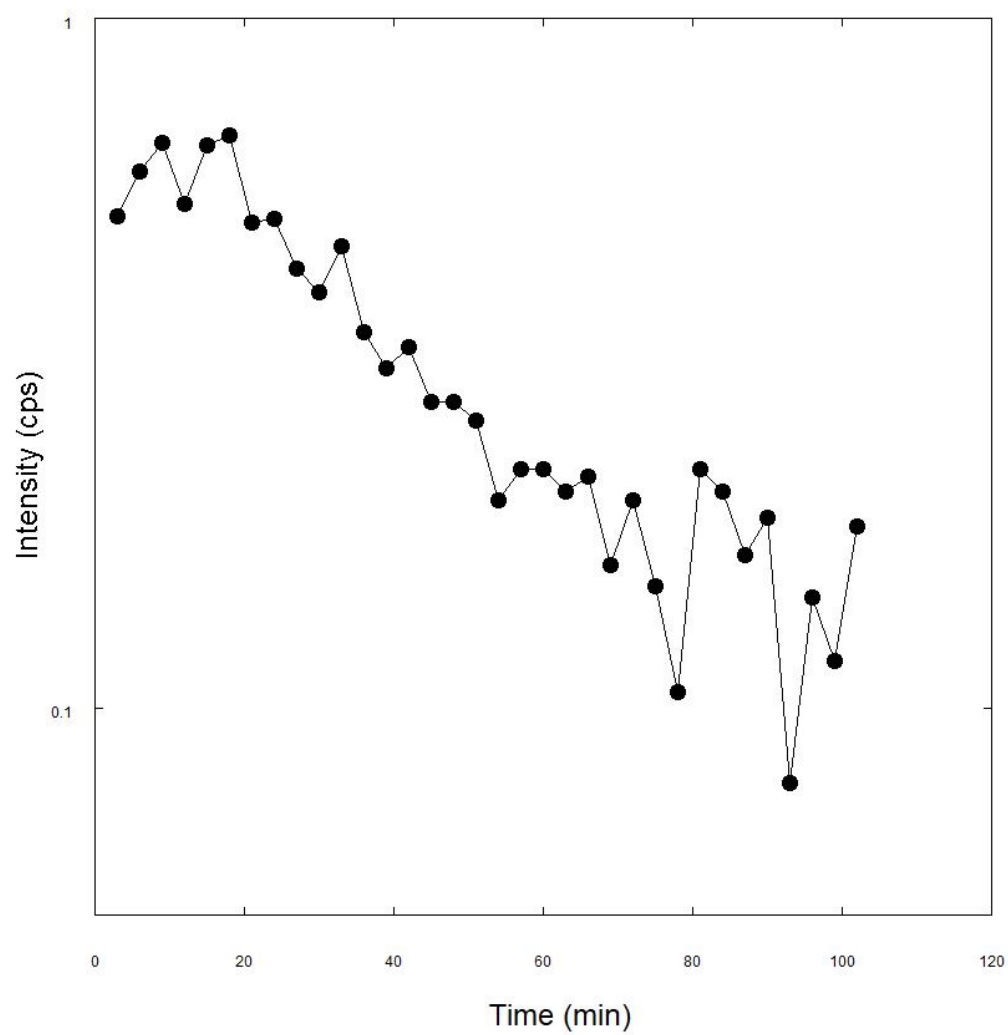
Figure 20. Time profile for the ^{226}Ra$^+$ ion signal in a Fh standard with Ra ([Ra] = 0.451 ppb).
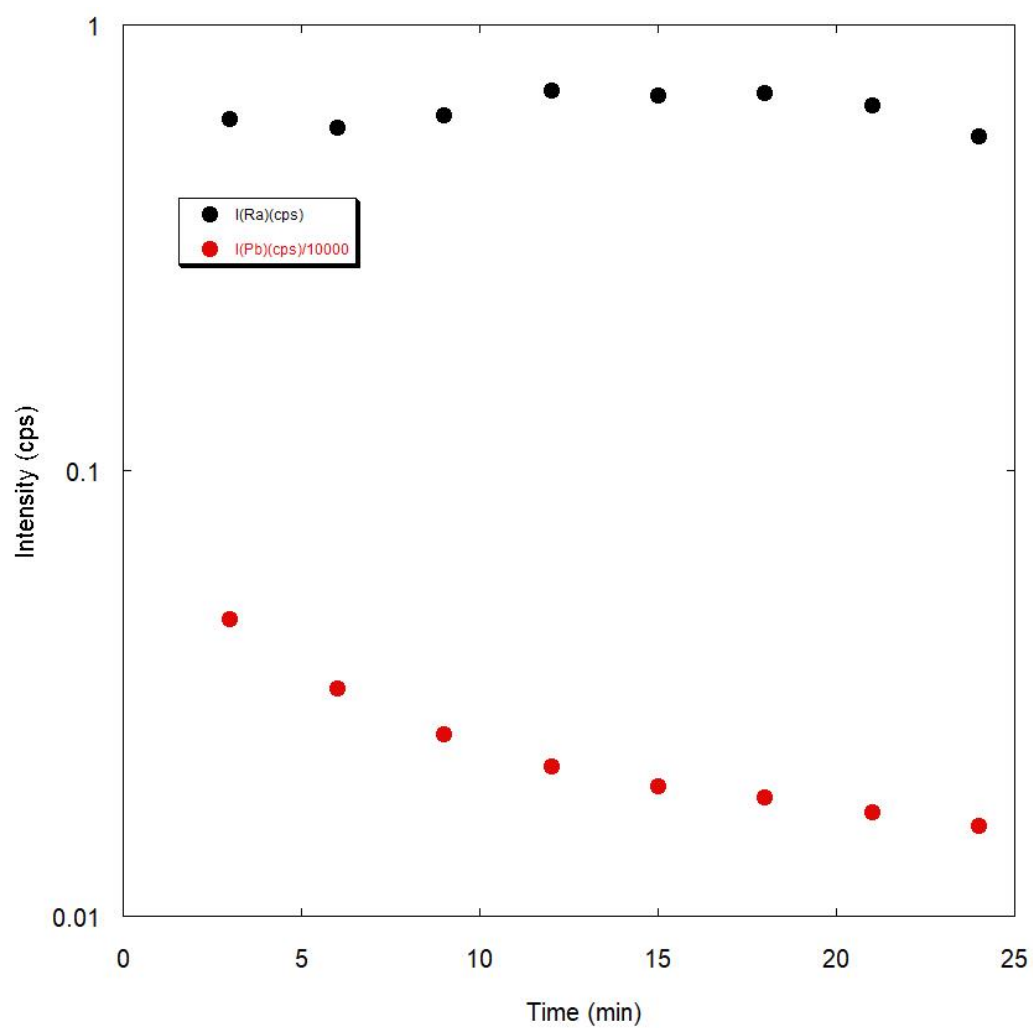
Figure 21. Spot analysis of ^{226}Ra$^+$ (black) and ^{208}Pb$^+$/10000 (red) for 150 cycles in a Fh standard with Ra.

Figure 22. Mass calibration of ^{226}Ra$^+$ mass peak (white) to that of ^{208}Pb$^+$ mass peak (blue) in uraninite using a multi-collector detector.
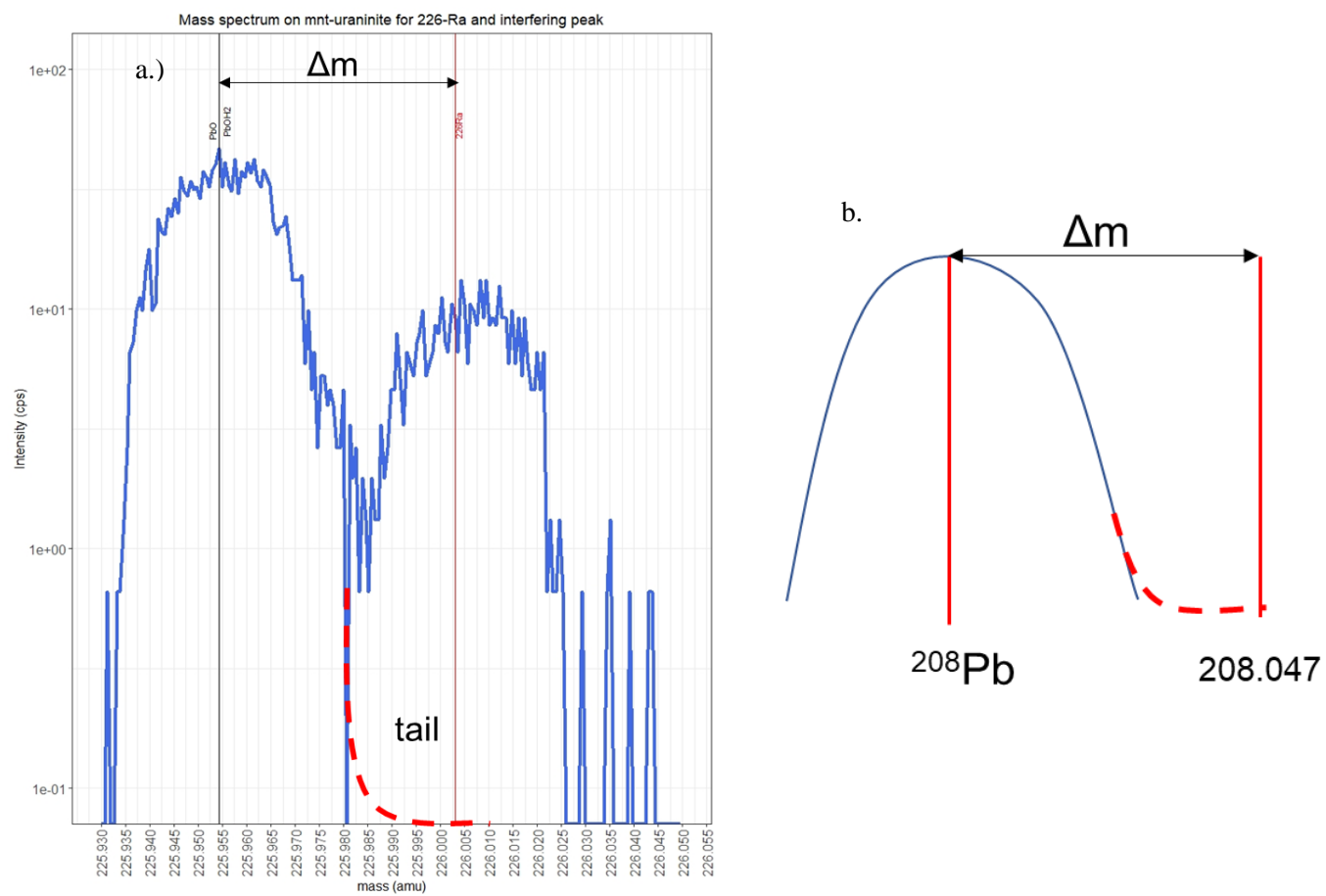
Figure 23. Visual representation of the tail positions of the interfered ^{226}Ra$^+$ peak and the interfering ^{208}Pb$^+$ peak.
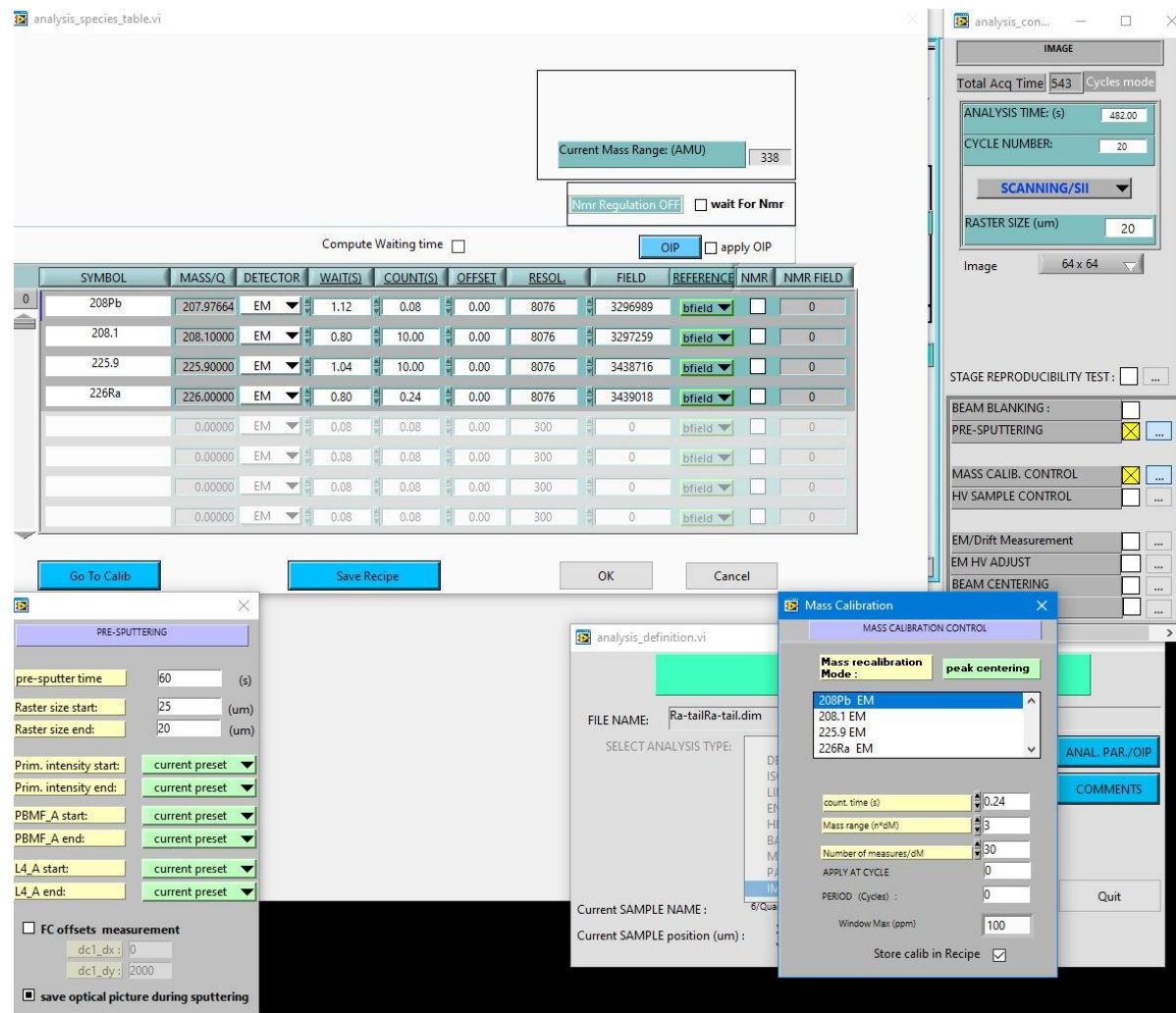
Figure 24. Analysis definition for the tail contribution analysis: top left. Table denoting analysed isotopes, each with their specific counting time, waiting time and b field value; top right. Window denoting cycle number, total acquisition time including analysis time and pre-sputter duration, raster size of the analysed area and pixel resolution of the image; bottom left. Pre-sputter details regarding raster size and amount of time; bottom right: Mass calibration control regarding peak centring on ^{208}Pb$^+$, counting time, mass range and the number of measurements.

Figure 25. Analysis definition for $^{226}Ra^+$ mass spectrum analysis: top left. Table denoting the mass range of the mass spectrum (dM-; dM+), waiting time, b field value and amount of mass steps; top right. Window denoting total acquisition time including analysis time and waiting time.
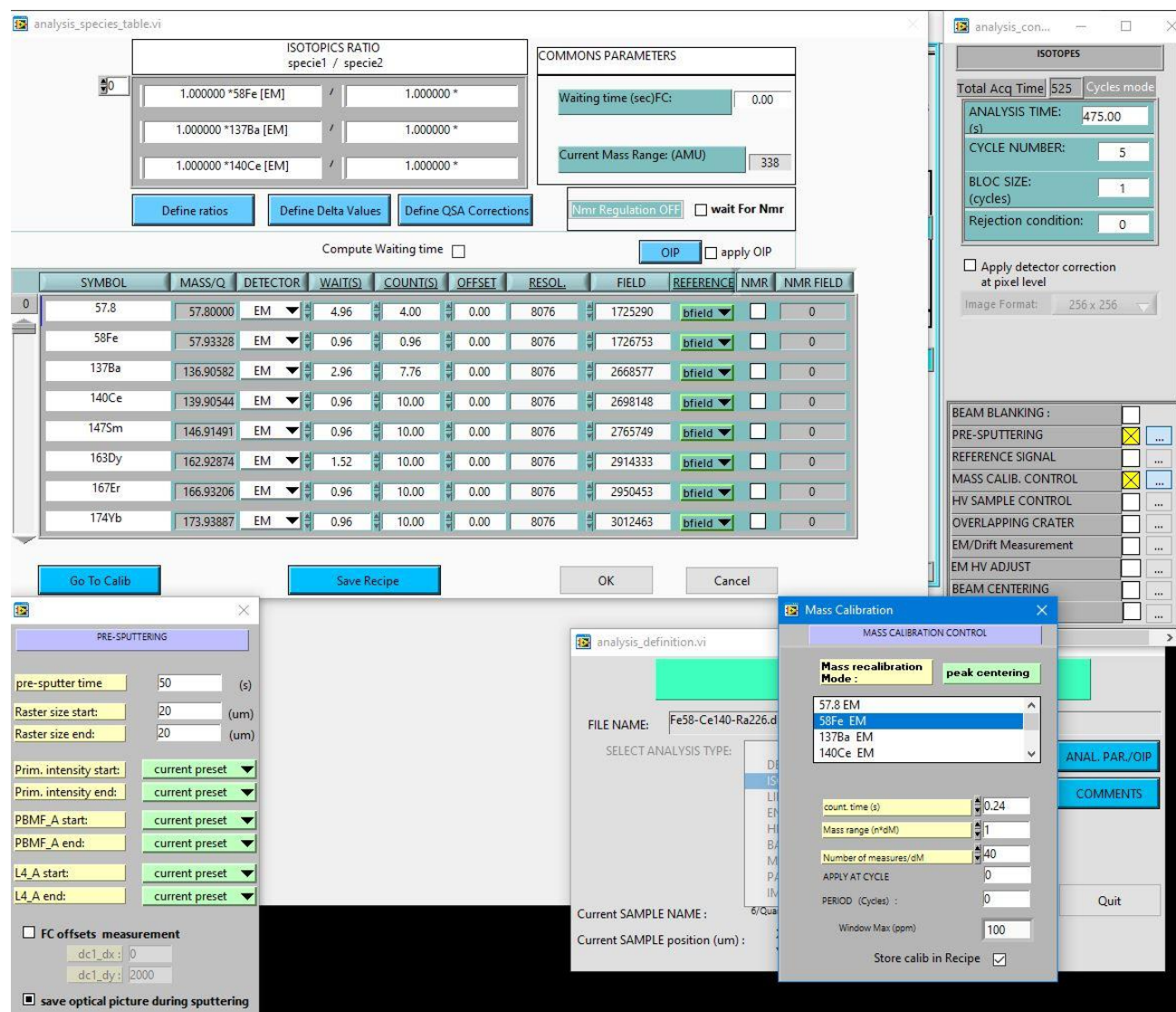
Figure 26. Analysis definition for MREE interference analysis: top left. Table denoting analysed isotopes, each with their specific counting time, waiting time, and b field value; top right. Window denoting cycle number, total acquisition time including analysis time and pre-sputter duration and raster size of the analysed area; bottom left. Pre-sputter details regarding raster size and amount of time; bottom right: Mass calibration control regarding peak centring on $^{58}Fe^+$, counting time, mass range and the number of measurements.
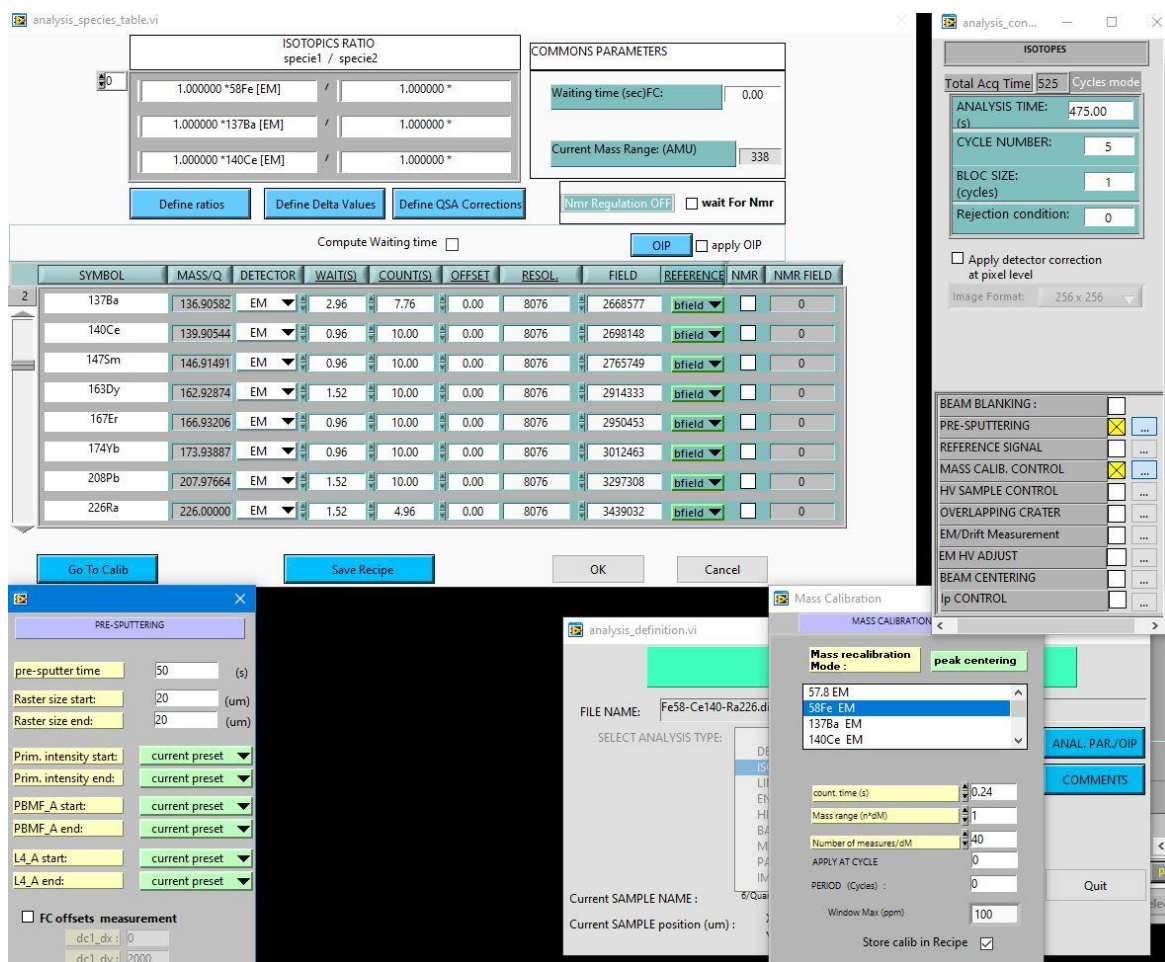
Figure 27. Analysis definition for MREE interference analysis continued: top left. Table denoting analysed isotopes, each with their specific counting time, waiting time, and b field value; top right. Window denoting cycle number, total acquisition time including analysis time and pre-sputter duration and raster size of the analysed area; bottom left. Pre-sputter details regarding raster size and amount of time; bottom right: Mass calibration control regarding peak centring on $^{58}Fe^+$, counting time, mass range and the number of measurements.

4.3.4 Performance of Ra detection

Ionisation efficiency

The tail contribution of the interfering mass peak on the left side of the $^{226}Ra^+$ mass peak was evaluated by obtaining a series of mass spectrums at different values of energy offset and HMR settings. The tail contribution was undertaken by observing the interfered peak/$^{208}Pb^+$ and $^{226}Ra^+$/Interfering peak ratios at different energy offset values and m/Δm of 8000 and at different HMR settings with an offset of 0 eV. As seen in figure 28, the energy offset mass spectrums showed a gradual signal decrease as the energy offset further decreased, without any apparent separation on the interfering peak and $^{226}Ra^+$ peak. The HMR mass spectrums showed some separation occurring at m/Δm 8000. Further evaluation of the tail contribution of the previously mentioned ratios was done through spot analyses while using energy offset or HMR. The HMR above m/Δm 8000 significantly decreased tail contribution based on the ratios shown in figure 29.

$^{226}Ra^+$ background signal

Calibration curves for the Fh Ra standards series were obtained for almost every session and normalised to $^{58}Fe^+$, as shown in figure 30.

In order to determine whether the resulting $^{226}Ra^+$ signal was true Ra and not a background signal, the baseline for the $^{226}Ra^+$ signal was established. The baseline of the $^{226}Ra^+$ signal was measured at the Ra mass of 226.025 by analysing Fh standards that do not contain Ra and any interfering elements. Ref-ferri-Ra0 was the best candidate as it contains only Fe, P and Pb. Figure 31 shows the baseline measured at the mass of Ra in all non-Ra Fh standards in different sessions. The normalised background signals to $^{58}Fe^+$ are shown in figure 32, which made it more evident that the baseline is around 0.015 cps.

Figure 33 shows the calculated background Ra concentration based on the Ra calibration curves in figure 30. In the July 22 session, the background signal was the equivalent of 0.27 ppb.
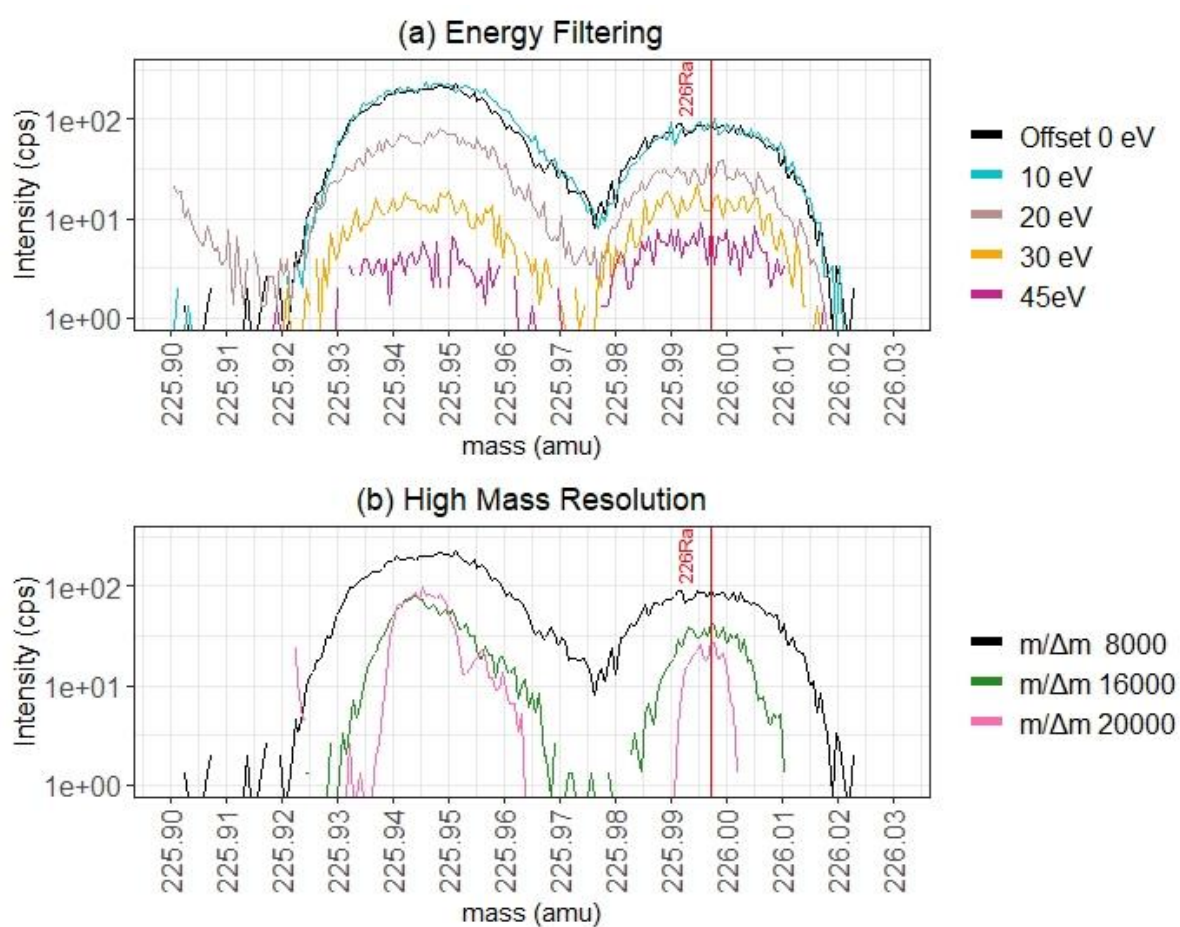
Figure 28. Mass spectrum at m/z= 226.025 featuring (a) energy filtering (with m/Δm= 8000) and (b) high mass resolution (without energy offset).

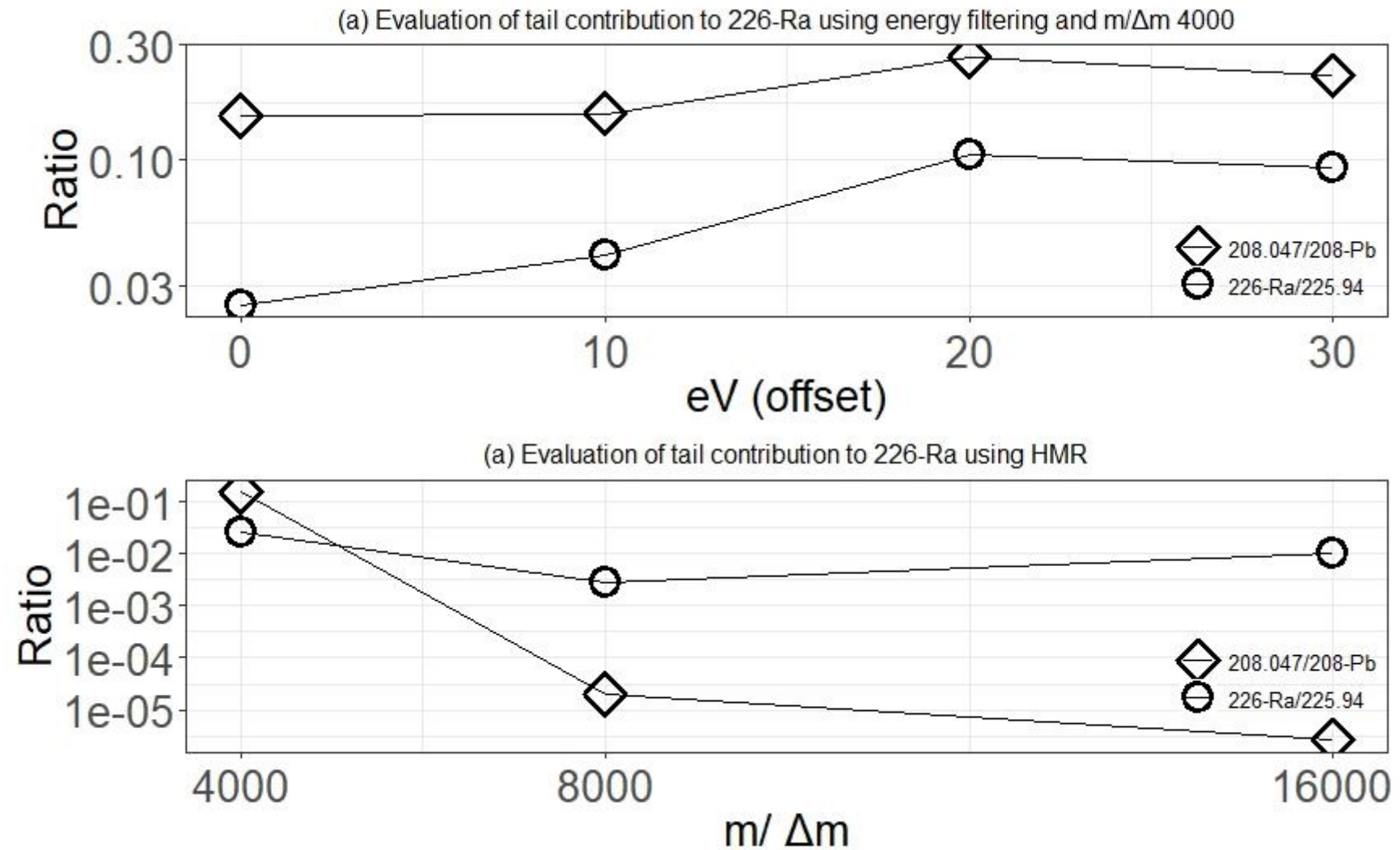Figure 29. Evaluation of interfering peak of $^{226}Ra^+$ tail contribution to $^{226}Ra^+$ signal by applying (a) energy filtering (with m/Δm= 4000) and (b) high mass resolution (without energy offset).

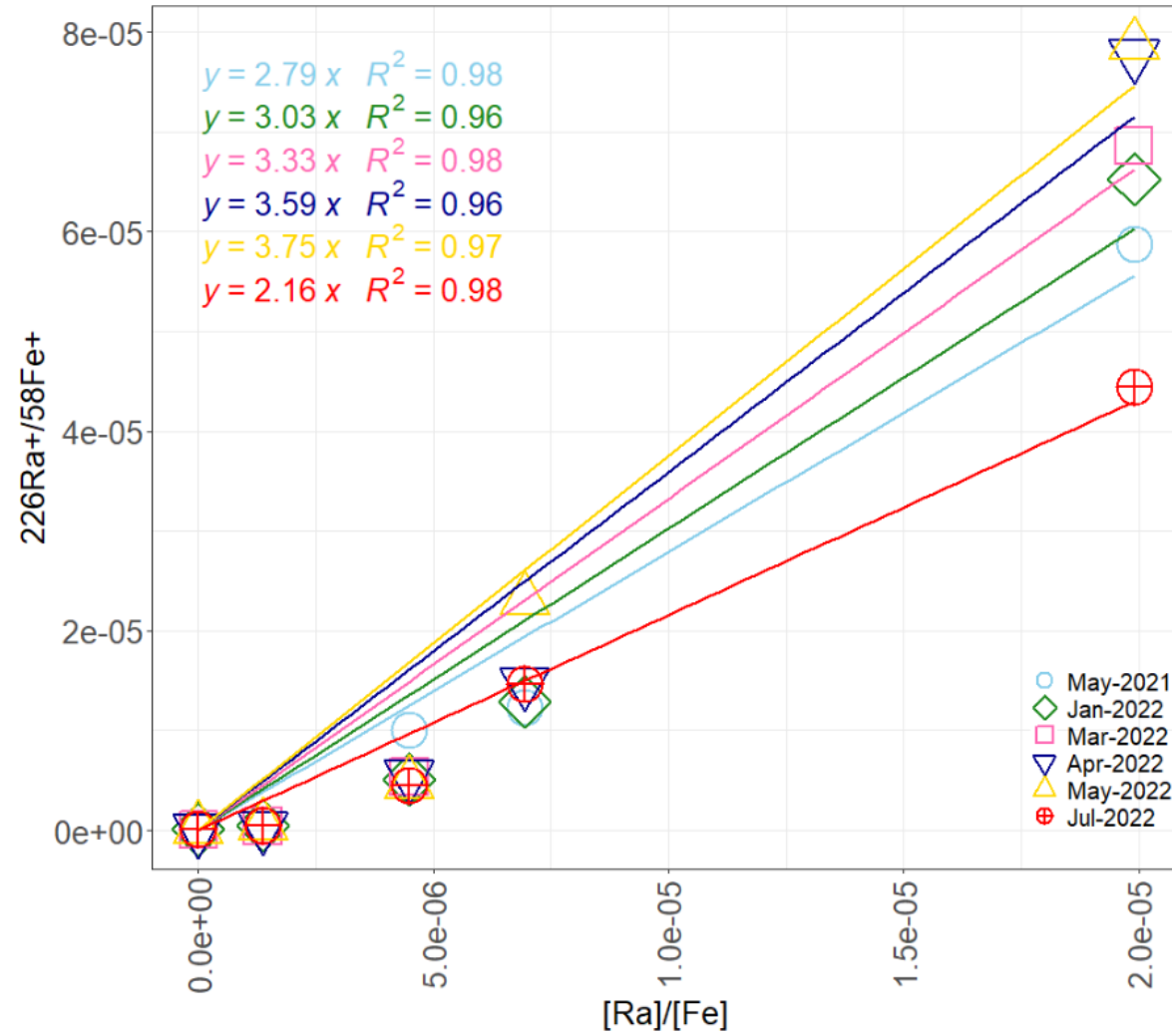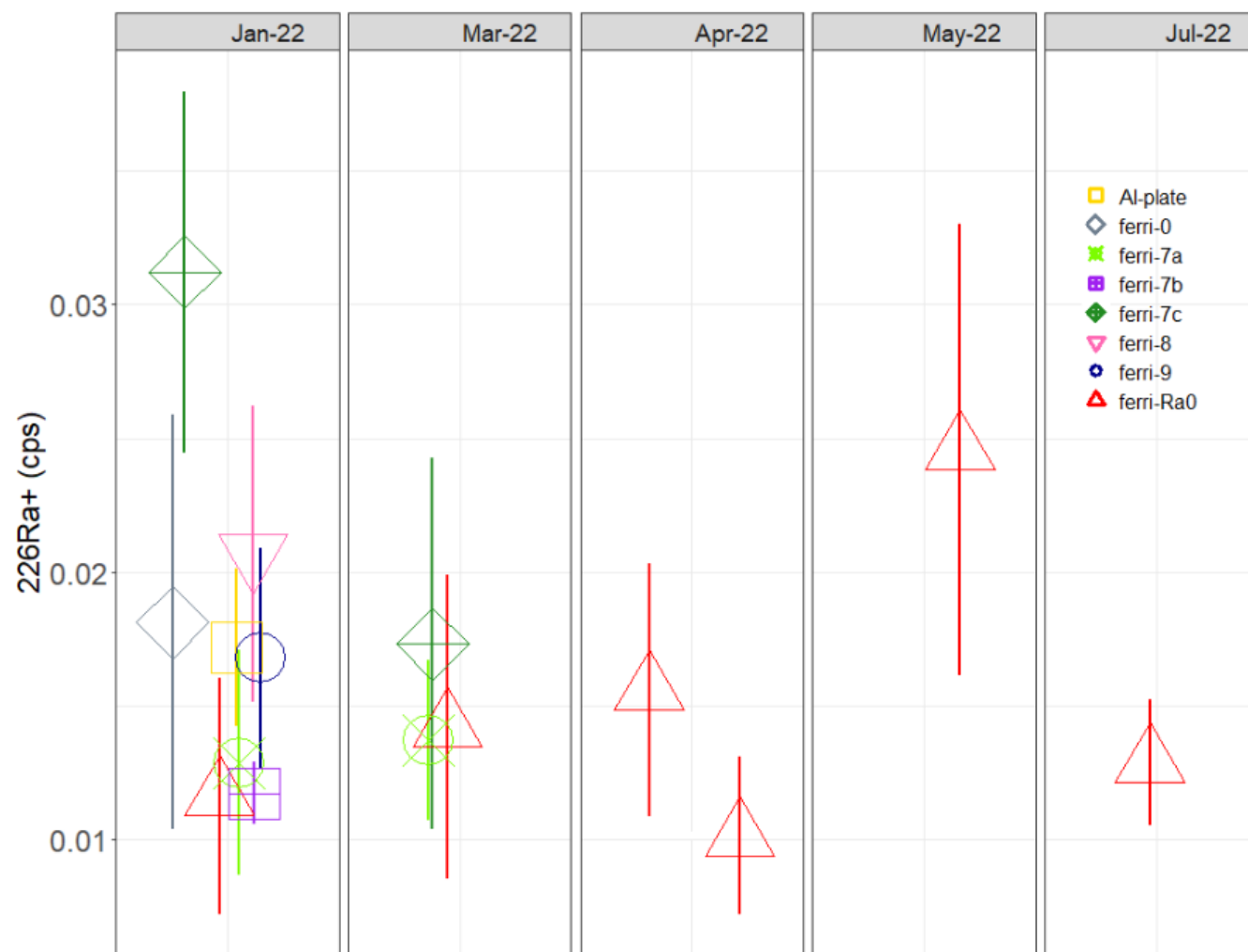Figure 30. $^{226}Ra^+$ normalised to $^{58}Fe^+$ calibration curves for every session

Figure 31. ^{226}Ra$^+$ background signal analysis in Fh standards without Ra and aluminium plate for every session.
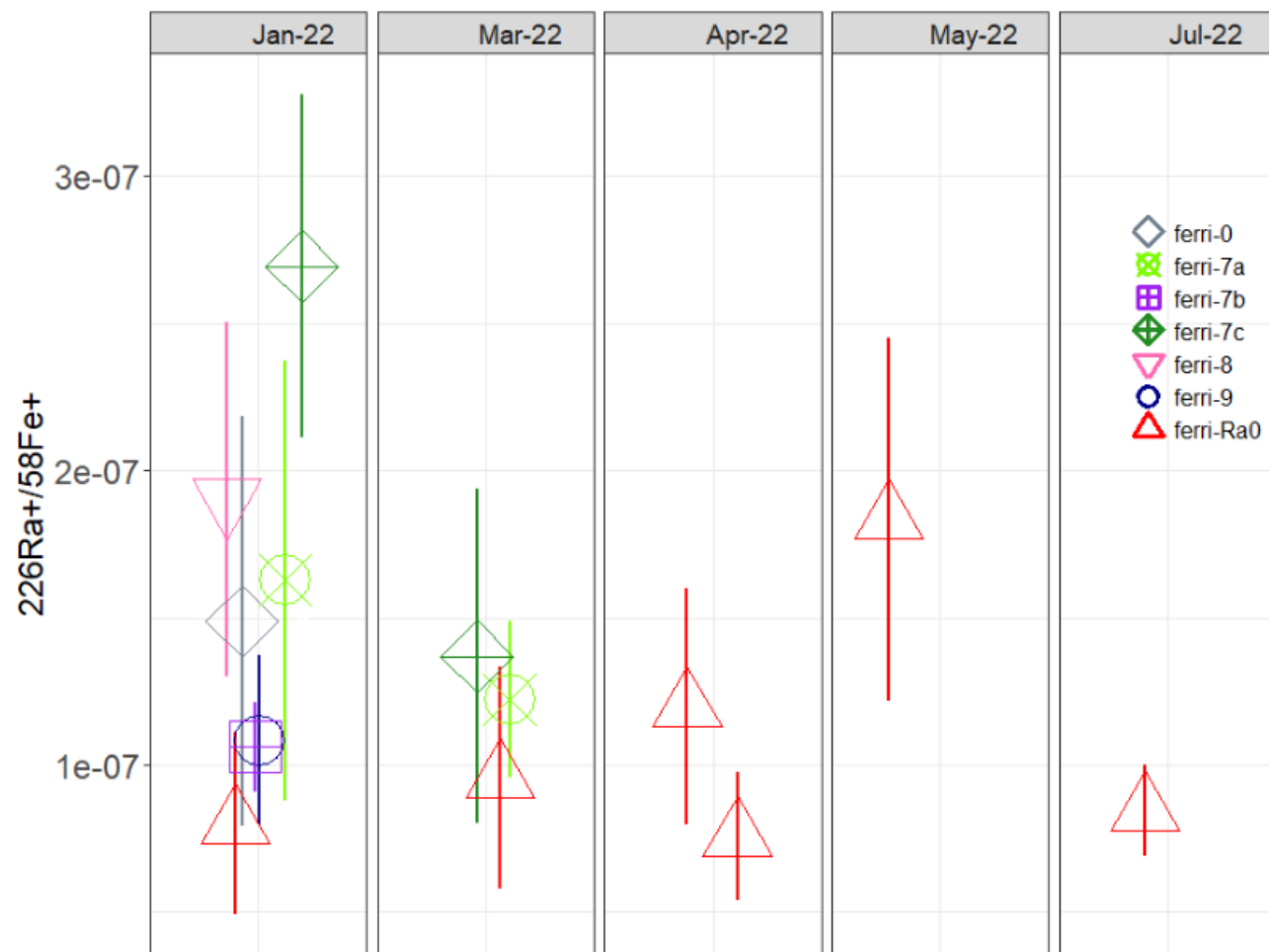
Figure 32. $^{226}Ra^+$ background signal normalised to $^{58}Fe^+$ in Fh standards without Ra for every session.
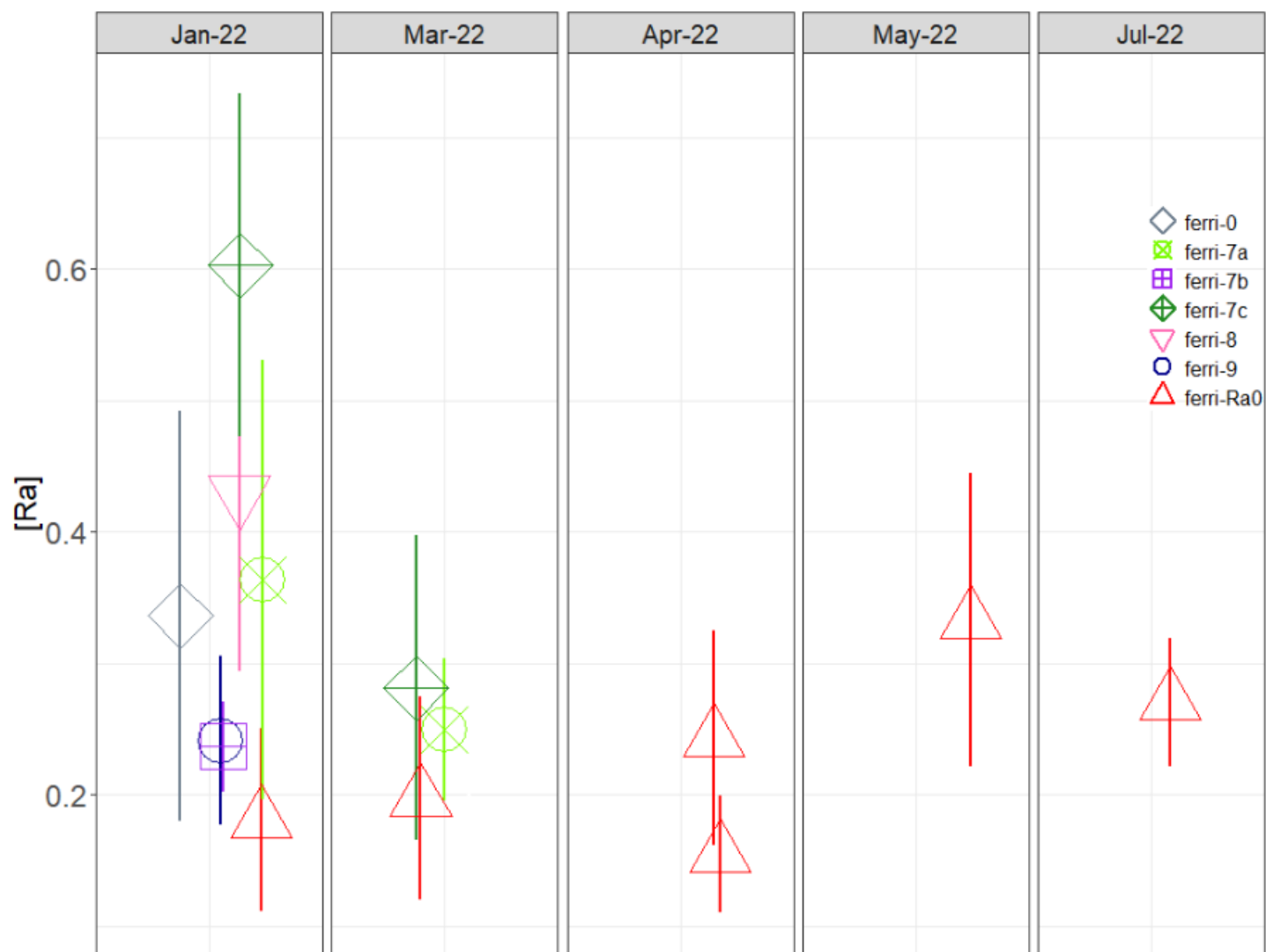
Figure 33. Corresponding Ra concentration for each $^{226}Ra^+$ background signal for every session.

4.4 Discussion

With the confirmed homogeneity based on morphological and chemical observations in SEM, the ref-ferri-7 series was deemed a suitable homogeneous Fh standard series for AFBs analysis. The same could be said for the Fh Ra standard series, which showed a uniform colour over their surface. In the past Fh standard creation protocol, chemical composition was evaluated as well, but only for the ref-ferri-7 REE series, as seen in figure 34, through which they were deemed to be homogeneous standards, along with uniform colour shade over the surface.

The appropriate interference reduction methods were determined while maintaining high transmission of the $^{226}Ra^+$ ion signal by evaluating tail contribution and observing how the transmission was affected. Mass spectrum analysis at the $^{226}Ra^+$ mass peak (Fig. 28) did not provide any guidance regarding which interference reduction methods to apply, except that the peak at m/Δm 20000 was too thin (0.01 amu thickness), leading to difficulty during mass centring, and thus inappropriate for $^{226}Ra^+$ analysis. Therefore, tail contribution using interfering peak/ interfered peak ratios obtained through spot analysis was applied (fig, 29). The tail contribution analysis revealed that energy offset did not decrease the tail contribution, hinted by the mass spectrum as well. It was apparent that HMR above m/Δm 8000 significantly decreased tail contribution based on the estimated interfered peak/$^{208}Pb^+$ and $^{226}Ra^+$/Interfering peak ratios. Accordingly, at m/Δm 8000 an interfering peak of an intensity of 10 cps would have a tail contribution to the $^{226}Ra^+$ signal of 0.0001 cps which was deemed negligible. As such, it was concluded that no significant interferences or tail contributions were present.

Interference of MREE to the $^{226}Ra^+$ signal was initially speculated due to high $^{226}Ra^+$ background values in the MREE and HREE Fh standards, as seen in the Jan 22 session in figure 31. However, upon repeating the analysis, the $^{226}Ra^+$ signal significantly decreased in the MREE and HREE Fh standards, close to the baseline level set by the ref-ferri-Ra0 standard. Therefore, MREE and HREE did not contribute to the $^{226}Ra^+$ signal as they showed intensity signals close to baseline values. The fluctuation of the signal might have been influenced by machine and/or surface conditions. Furthermore, microtomed surfaces were rough and not optimal for SIMS analyses, often requiring smooth and flat surfaces.

As it was established that there was no significant interference to the Ra signal and background signal intensity was established to be around 0.02 cps, a Ra calibration curve based on in-house synthesised Fh standards was drawn for each session.

So far, there are no Ra calibration curves drawn for SIMS analysis, as Ba is usually used as a surrogate Ra, Ba and Ra having similar chemical and environmental behaviours[68]. The calibration curves demonstrated that the standards correlated. There was some non-linearity observed in the Ra calibration curves due to the 3rd standard from the left being under-detected, whose cause is unknown. However, the R^2 factors of the calibration curves (Fig. 30) were between 0.96 and 0.98, indicating that the Fh Ra standard series was viable for estimating Ra concentrations in AFBs.
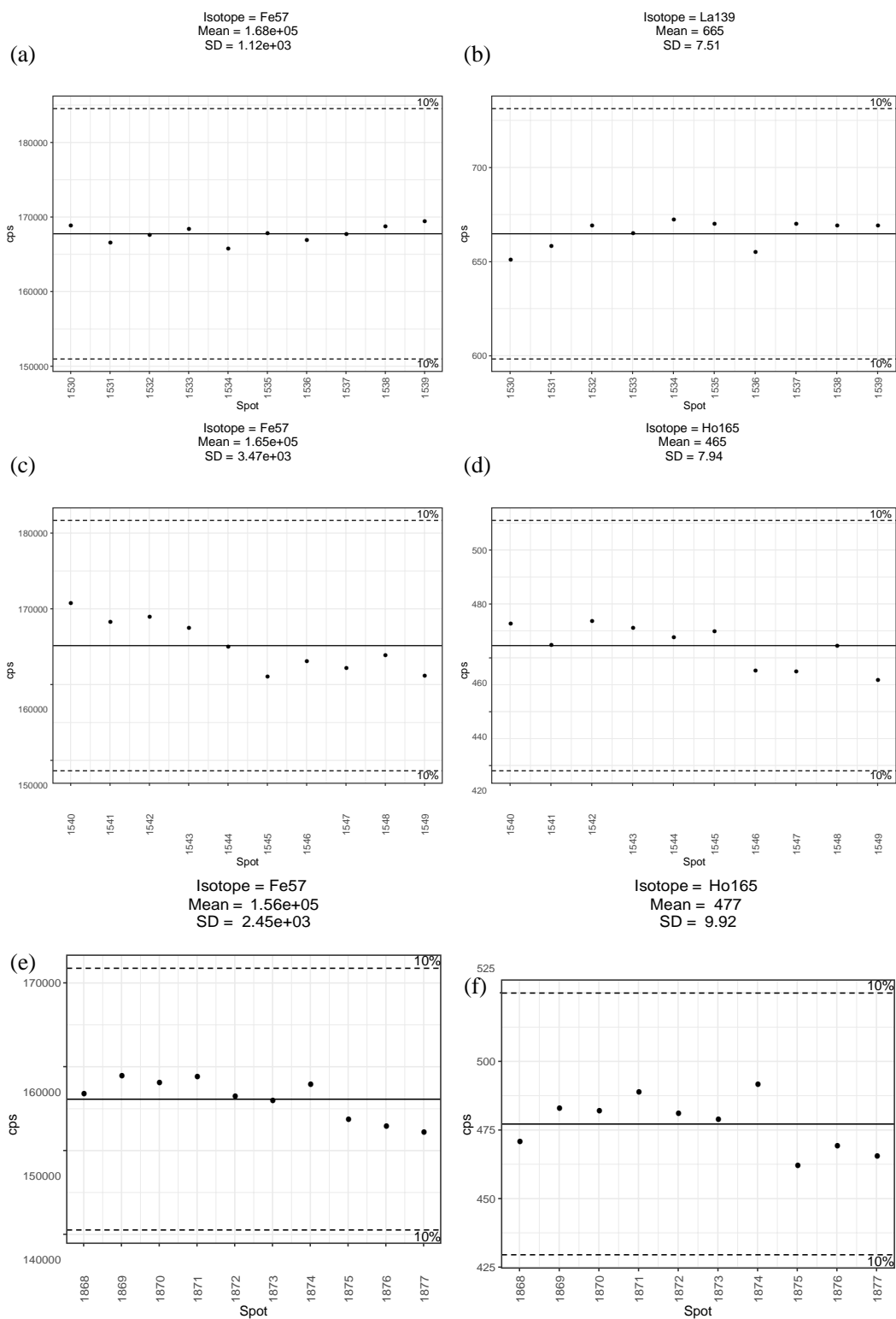
Figure 34. Secondary ion intensities of ref-ferri-7a-2 for (a) 57-Fe and (b) 139-La, of ref-ferri-7b-3 for (c) 57-Fe (d) 165-Ho, and of ref-ferri-7c-5 for (e) 57-Fe (f) 165-Ho. The solid line represents the mean of the obtained ion intensities, and the dashed lines represent a 10% difference from the mean.

4.5   Conclusion

A Fh standard creation method was developed. As a result, two reliable Fh standard series have been created regarding homogeneity and secondary ion yields. These series were used to calculate the trace element and Ra abundances of AFBs. For the first time, A standard series doped with Ra was created and $^{226}Ra^+$ calibration curves were drawn for each session.

The analytical conditions for REE analysis and Ra analysis were established. In addition, the analytical conditions for Ra analysis were further improved to detect the $^{226}Ra^+$ peak without interference and sufficient signal successfully, the tail contribution to $^{226}Ra^+$ being deemed as negligible.

 The background signal of $^{226}Ra^+$ was determined and used in AFB analyses as an indicator for the detection of the true signal above background levels. Once the true signals of $^{226}Ra^+$ in AFBs were estimated, the $^{226}Ra^+$ normalised to $58Fe+$ calibration curve obtained from the previously synthesised and mounted Fh standards with Ra was to be utilised for the estimation of Ra concentrations of AFBs.

5. Chapter 5 Application to AFB analysis

5.1 Summary

The role of AFBs in the progression of malignant mesothelioma (MM) and other cancers and the mechanism behind the contribution of AFBs to cancer were investigated through in-situ AFB analysis of REE and $^{226}Ra^+$ by SIMS analyses.

$^{226}Ra^+$ was detected above the background signal in several AFBs of a smoking patient. As a general rule, secondary ion intensities were normalised to the major element comprising the matrix, in this case, Fe. The $^{58}Fe^+$ of AFBs was 10 times lower than that of the Fh standards, therefore the major element Ba was used as a confirmation of whether the Ra concentrations were to be estimated from $^{226}Ra^+$ or $^{226}Ra^+/^{58}Fe^+$ calibration curve. The Ba concentrations, estimated from the $^{137}Ba^+/^{58}Fe^+$ calibration curve, were above ICP-MS bulk Ba concentration which represented a diluted Ba concentration of the AFB. Therefore, the Ra concentrations were estimated from the $^{226}Ra^+/^{58}Fe^+$ calibration curve. The calculated Ra concentrations of AFBs were converted to effective doses of radioactivity and an AFB Ra hotspot model for malignant mesothelioma (MM) was drawn which indicated that a heterogeneous distribution of AFB Ra hotspots may lead to MM incidence.

5.2 Methods

5.2.1 AFB mounting protocol

Initially, TEM samples were considered for SIMS analysis. However, due to their nanometre size thicknesses, the TEM samples are not able to withstand a strong beam on the nA scale, making them unsuitable for analysis. Thus, an AFB sample mounting protocol for SIMS was developed, which could provide AFBs with micrometre scale thicknesses. The schematic diagram of the AFB sample mounting protocol is shown in figure 35.

The AFB sample mounting protocol involved encasing AFBs in resin and ultra-microtoming the resin-encased AFBs until their internal structure was exposed to the surface. A bullet-shaped numbered mould of 14x5x3 mm was used to mount the AFBs in resin. Firstly, about 70 µl (1/3 of the mould volume) of resin was pipetted in the mould of interest and left to cure overnight.

The following day, 10 µl of resin glue was pipetted over the surface of the cured resin from the previous day. The resin glue cured quickly once exposed to ambient air within 1 to 2 hours. After the resin glue was pipetted, the resin mould was moved to a microscope, where AFBs from a dried lung tissue sample were placed on the glue surface. The resin mould was placed on the glass slide of the dried lung tissue sample to prevent electrostatic forces from removing the AFBs off the tungsten needle when traversing between the glass slide and the resin mould. The number in the mould was used as a guide for the location of the AFBs and future steps. The AFBs were preferentially lined up at the edge of the glue-filled area by picking them up from the dried lung tissue sample with a tungsten needle of 0.5 µm thickness. After the AFBs were lined up, the resin glue was left to cure for about 5 hours.

After 5 hours, the positions of the AFBs were observed under an electronic optical microscope to confirm that their positions remained unchanged and that the resin glue appeared solid. Pictures of the AFBs were taken at this stage. After observing the AFBs, a stitched map of the resin mould was obtained using the same electronic optical microscope.

Subsequently, 100 µl of resin was gently pipetted over the AFBs, as two applications of 50 µl of resin. Finally, the resin mould was gently tilted to spread the pipetted resin evenly. The freshly pipetted resin was left to cure overnight.

The next step was preparing the resin block (as the resin mould was set, it is referred to as a resin block from this step onwards) for the ultra-microtoming of the AFBs. The resin block needed to be sawed and placed into an aluminium tube in order to be easily handled for ultra-microtoming. Based on the previously obtained electronic, optical microscope map of the resin block and the location of the AFBs within this map, the measurements of the cuts to be undertaken using the precision saw were estimated. The resulting cut resin block was required to have a width and length of under 4 mm so that it could fit a 4 mm wide and 5mm long hollow aluminium tube. The aluminium tube was hollow at both ends, so half of the aluminium tube was filled with malleable indium to create a solid bottom. Before proceeding to the next step, the fitting of the resin block into the aluminium tube was checked. If the dimensions of the resin block were too large to fit the aluminium tube, the block was shaved with sandpaper ensuring the location of the AFBs was furthest from where the shaving was being undertaken. Once the correct fitting of the resin block into the aluminium tube was confirmed, the fresh resin was gently added with a needle through the crevices around the resin block until the resin was seen to reach the top of the aluminium tube. The resin was left to cure overnight.

The resin block was set unto the microtome support and ultra-microtomed until the interiors of the AFB of interest were exposed. The AFBs were visible through the transparent resin by electronic optical microscope observation. As such, it was possible to estimate the amount of resin required to microtome in order to expose the AFBs. Once exposure of the AFBs to the surface of the resin was confirmed by an electronic optical microscope, the ultra-microtoming process was concluded.

The resulting AFB sample in the aluminium tube was placed within an aluminium disc with 5 mm diameter holes. The holes were created by drilling into a solid aluminium disk and smoothing the interior of the holes with sandpaper until the empty aluminium tubes could cleanly pass through the drilled hole.

The AFB sample was coated with 300 Å of gold and observed in SEM. The AFBs were photographed and mapped in SEM. The AFBs were located in SIMS analysis using a 50 μm^2 raster while probing $^{56}Fe^+$ and using an in-house mapping system. Once the AFB was located, the raster diameter was reduced to 20 μm^2 and centred.

SIMS analysis of AFBs yields secondary ion intensities. The secondary ion intensities needed to be converted into concentrations by analysing the AFBs together with a standard of the same matrix, in this case, the Fh standard series. Analysis of an AFB and an Fh standard involved a relationship between the intensity ratios of the Fh standard and AFBs. The relationship refers to using the secondary ion yields of the Fh standards with the intensity ratios of the AFBs to calculate the elemental abundances of the AFBs.
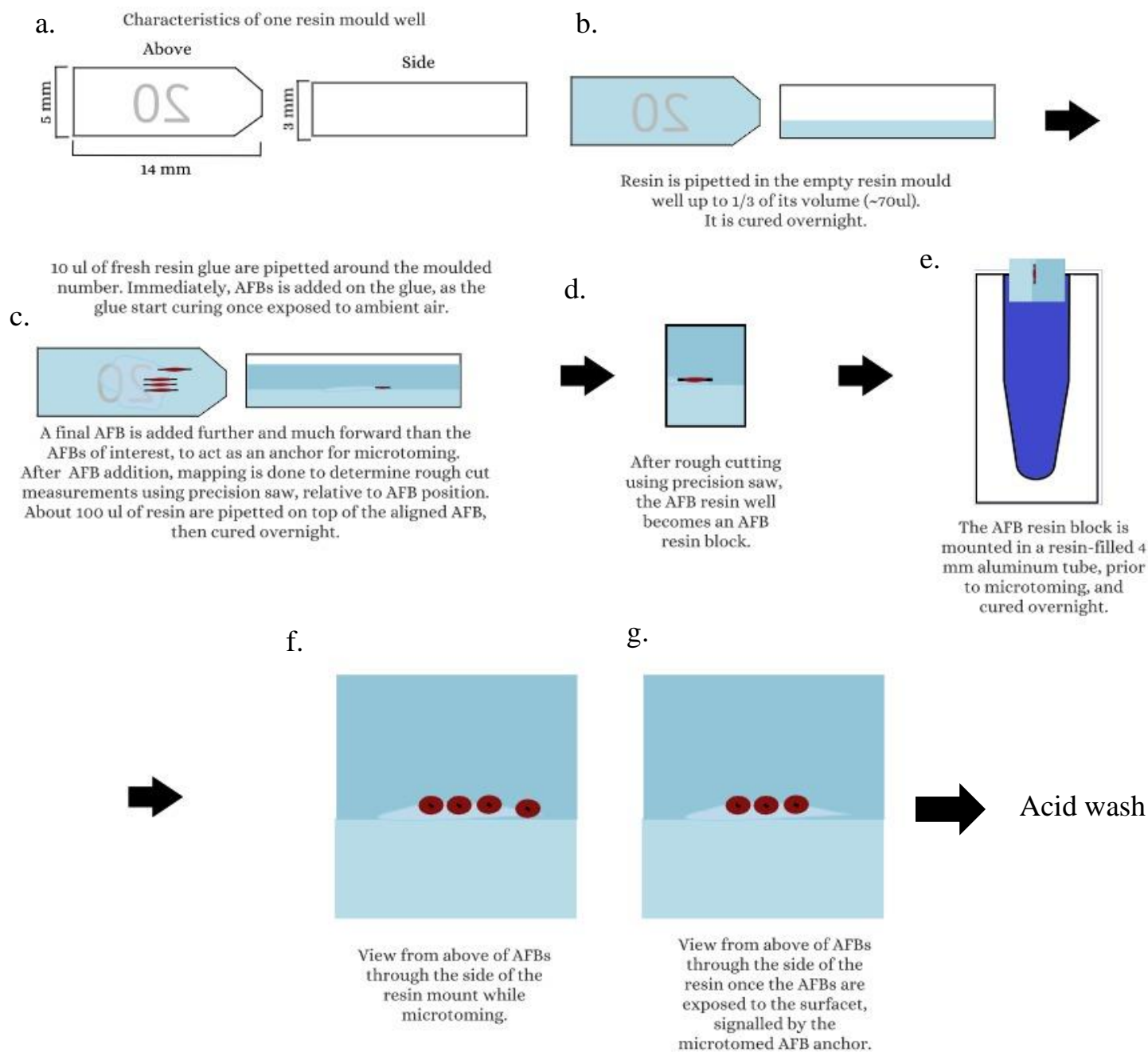
a. Characteristics of one resin mould well

Above

5 mm / 14 mm

Side

3 mm

b.

Resin is pipetted in the empty resin mould well up to 1/3 of its volume (~70ul). It is cured overnight.

c. 10 ul of fresh resin glue are pipetted around the moulded number. Immediately, AFBs is added on the glue, as the glue start curing once exposed to ambient air.

A final AFB is added further and much forward than the AFBs of interest, to act as an anchor for microtoming. After AFB addition, mapping is done to determine rough cut measurements using precision saw, relative to AFB position. About 100 ul of resin are pipetted on top of the aligned AFB, then cured overnight.

d. After rough cutting using precision saw, the AFB resin well becomes an AFB resin block.

e. The AFB resin block is mounted in a resin-filled 4 mm aluminum tube, prior to microtoming, and cured overnight.

f. View from above of AFBs through the side of the resin mount while microtoming.

g. View from above of AFBs through the side of the resin once the AFBs are exposed to the surfacet, signalled by the microtomed AFB anchor.

Acid wash

Figure 35. AFB sample mounting protocol: a. Resin mould characteristics; b. Pipetting the first volume of resin; c. Adding resin glue, gluing AFBs and one AFB much more in front which serves as a marker for microtome, and pipetting the second and final volume of resin which is cured overnight; d. rough cutting using a precision saw of the resin mould into a resin block with AFBs; e. mounting the AFB resin block into an Al tube filled with resin which is cured overnight; f and g. Microtoming until the AFBs are exposed, indicated by the disappearance of the AFB marker. After microtoming, the AFB sample is acid washed to remove any contaminants.

5.2.2 Analytical conditions

The REE analytical conditions are the same as the ones described in chapter 4.2.2.

Prior to commencing the Ra analysis for AFB, the previously established analytical conditions for Ra were changed due to low intensities of $^{208}Pb^+$ in the AFBs. This change was due to the centring of the $^{226}Ra^+$ signal to that of the $^{208}Pb^+$ signal not being possible. Therefore, the multi-collector was used to clearly distinguish the $^{226}Ra^+$ peak as it was calibrated on the $^{208}Pb^+$. Afterwards, the determined B field value for $^{226}Ra^+$ was copied into a new imaging analysis file that involved peak jumping and mass centring based on $^{58}Fe^+$, which was detectable in both the standard and the sample. The analytical conditions and definitions for the final $^{226}Ra^+$ analysis in the Fh standards and the AFBs are shown in table 5 and figure 36. The instrumental background was measured at a mass of 57.9, and the mass of the interfering peak was measured prior to $^{226}Ra^+$.

5.2.3 Image data reduction

For each AFB ion analysis, a region of interest for the AFB location was selected based on the distributions of $^{137}Ba^+$ and $^{208}Pb^+$ ion signals. An example of a selected region of interest in each analysed ion is shown in figure 37.

5.3 Results

5.3.1 REE analysis

In figure 38 the secondary yield distribution for metal and oxide elements of the ferri-7 series is shown in comparison to a previously analysed silicate standard series which was extensively studied within the laboratory. The Fh standard series had metal and oxide yields 1-60 % lower than the silicate standards. In addition, oxide yields of neighbouring isotopes, such as ^{143}NdO and ^{144}NdO, showed close yield values.

Secondary ion intensities from 2 AFBs of patient N1 were obtained in SIMS. The intensities were used to calculate their elemental abundances using the secondary ion yields obtained from the Fh REE standard series. These elemental abundances are plotted together with the bulk elemental abundances of patient N1 in figure 39, which were obtained using ICP-MS. The 2 AFBs showed high abundances for Sr and Ba, while Eu-Lu concentrations contained their isobaric interferences. In addition, light REEs were lower in abundance than heavy REEs.
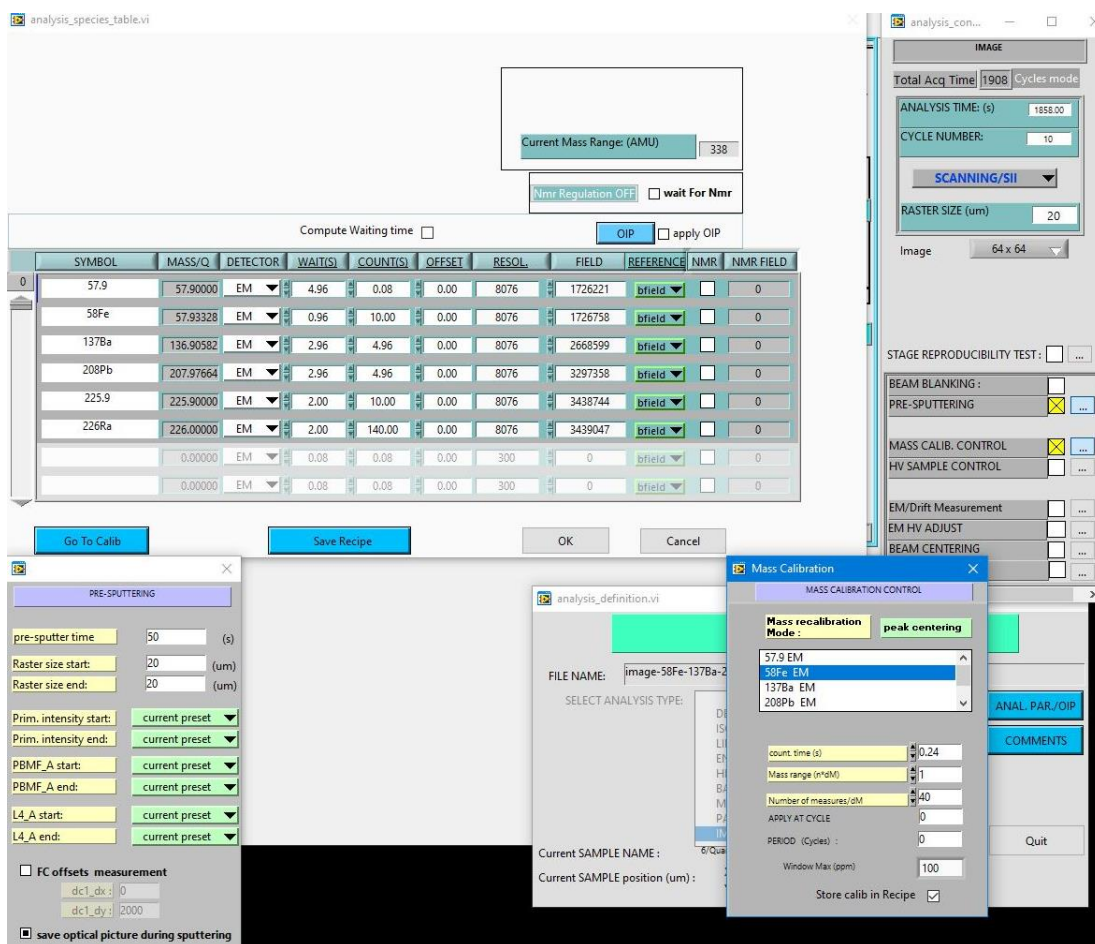
Figure 36. Analysis definition for AFB analysis: top left. Table denoting analysed isotopes, each with their specific counting time, waiting time and b field value; top right. Window denoting cycle number, total acquisition time including analysis time and pre-sputter duration, raster size of the analysed area and pixel resolution of the image; bottom left. Pre-sputter details regarding raster size and amount of time; bottom right: Mass calibration control regarding peak centring on $58Fe^+$, counting time, mass range and the number of measurements.
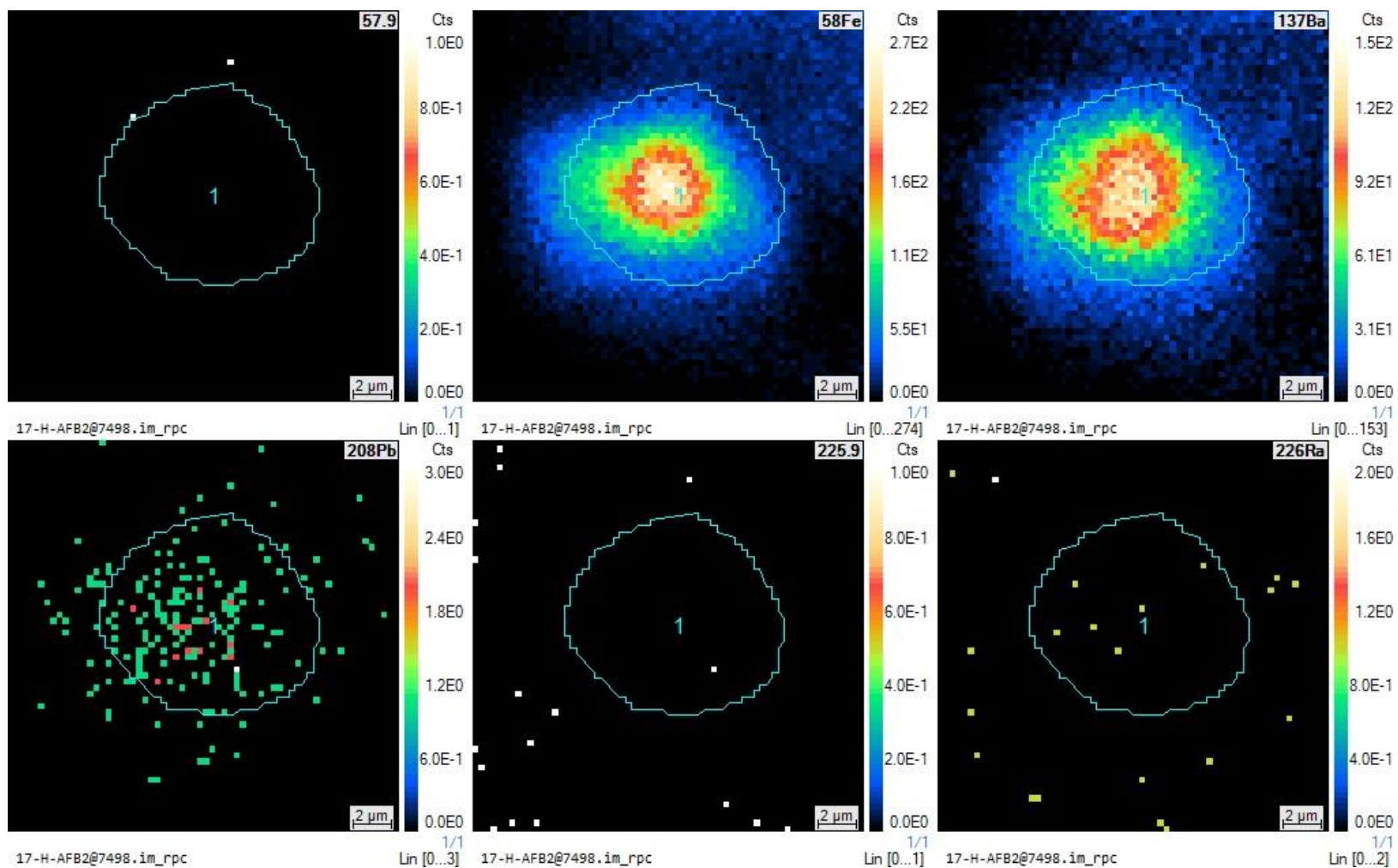
Figure 37. Ion images for each analysed isotope indicated on the top right with a region of interest (cyan circle).
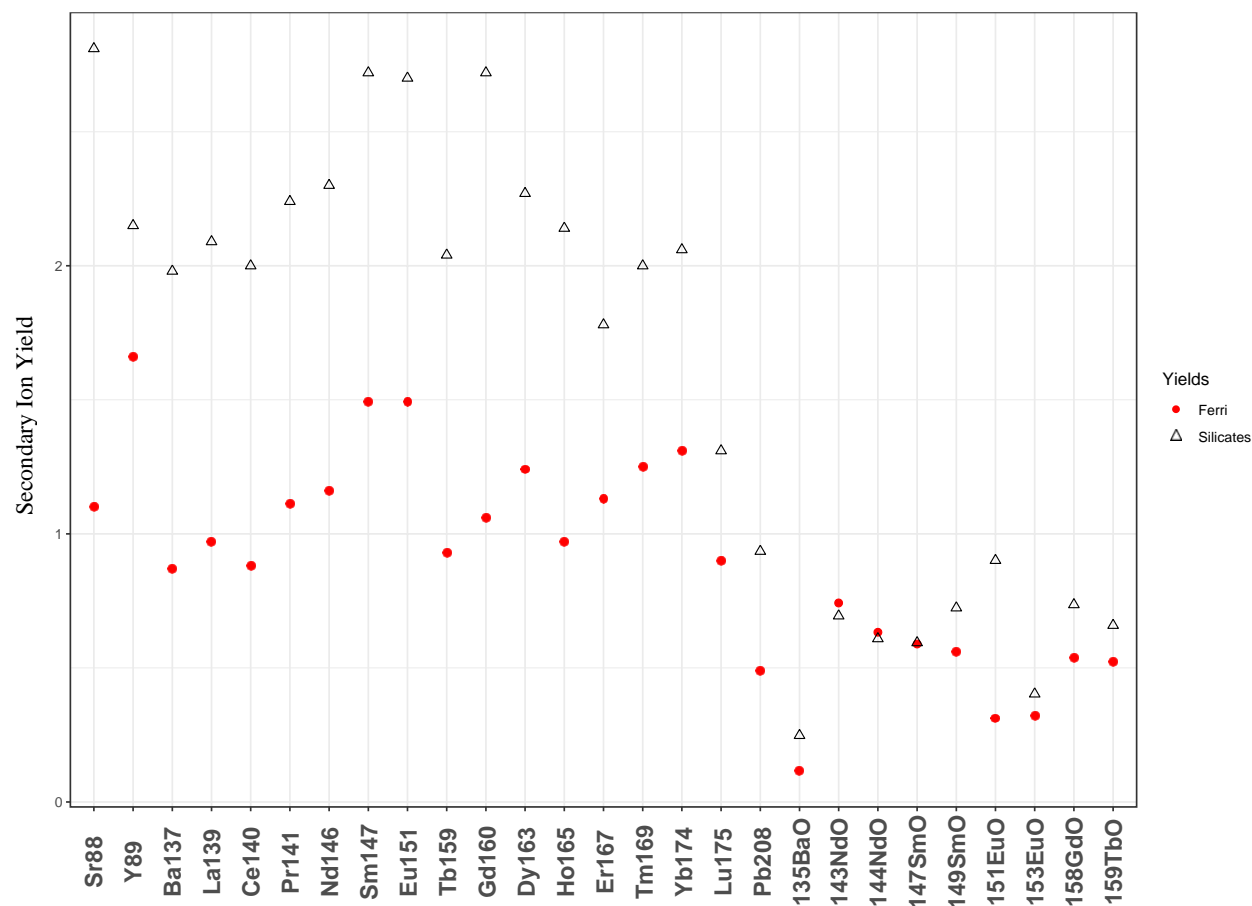
Figure 38. Secondary ion yields of Fh standard series (red) and silicate standard series (black), where the secondary yield equals to the intensity of the analysed isotope (ZZ^+) normalised to $^{57}Fe^+$ divided by the known molar concentration of the analysed isotope normalised to the molar concentration of ^{57}Fe. ($Y = (ZZ^+/^{57}Fe^+)/([ZZ]/[^{57}Fe])$).
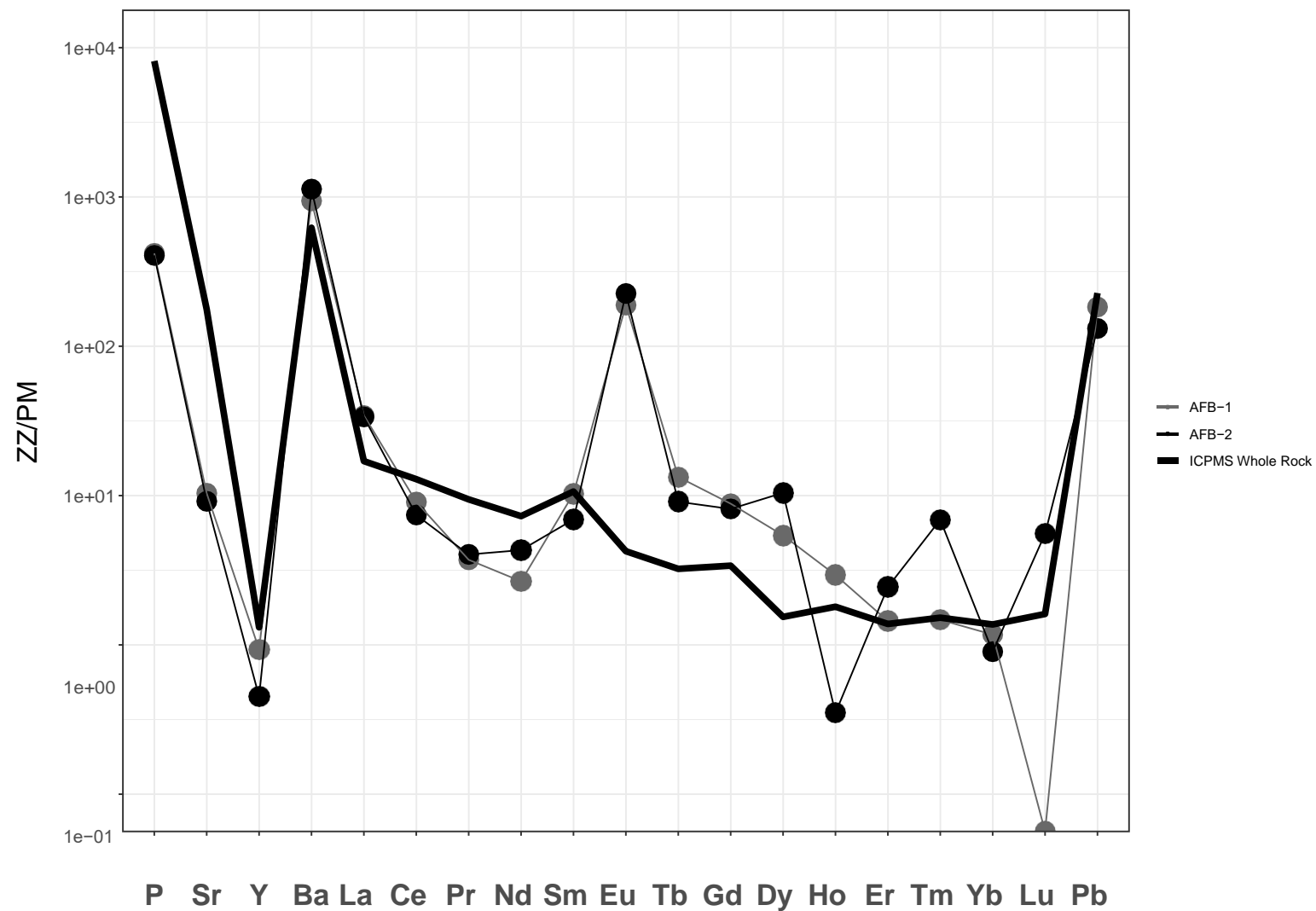
Figure 39. Elemental abundances of 2 AFBs from patient N1 analysed SIMS analysis with elemental abundances of an aliquot of patient N1 obtained by bulk ICP-MS analysis by Nakamura et al., 2009[1], all normalised to primitive mantle values.

5.3.2 Ra analysis

8 AFBs of smoking patient S1 were analysed with the same analytical conditions as the Fh Ra standard series in the July 22 session. Figure 40 shows the AFBs lined up on the border of the resin glue on top of the first volume of resin (Fig. 40a) prior to covering them with resin, sawing and microtoming, and the AFBs after microtoming and acid washing for 15 seconds with 0.01 M HCl (Fig. 40b). Multiple instances of imaging analysis were undertaken for the same spot as the ion beam sputtered through the vertically oriented AFBs. In addition, ref-ferri-Ra0 was analysed for background signal evaluation before and after AFB imaging analyses.

$^{58}Fe^+$ and $^{137}Ba^+$ ion intensities

Secondary ion intensities are usually normalised to a major element that represents the most abundant element in the matrices of both the standard and sample, in this current study being $^{58}Fe^+$. However, after the analyses of the AFBs, $^{58}Fe^+$ in the AFBs was found to be more than 10 times lower than in the Fh standards due to matrix effects on the ion yield. Therefore, $^{137}Ba^+$ was used to determine whether normalisation to $^{58}Fe^+$ was to be applied as planned. Ba and Ra are in the same periodic table group, so they were expected to have similar chemical behaviour and Ba is a major element as well. Calibration curves for Ba (Figs. 41 and 42) were drawn for the determination of the Ba concentrations in the AFBs and allowed a comparison to the Ba concentration obtained in this study by ICP-MS for the bulk lung sample. The Ba concentrations were estimated from the $^{137}Ba^+$ signals (Fig. 41) and $^{137}Ba^+/^{58}Fe^+$ (Fig. 42) signals. Ba concentrations estimated from the $^{137}Ba^+/^{58}Fe^+$ signals were higher than that obtained by bulk lung sample analysis by ICP-MS (Fig. 43b), while the Ba concentrations estimated from the $^{137}Ba^+$ were below than that of the bulk lung sample analysis by ICP-MS (Fig. 43a).

Detection of Ra in AFBs

The $^{226}Ra^+$ signals of AFBs above the background signal, along with the lines to indicate 3σ, 2σ and 1σ values of the standard deviation of the background signal, are shown in figure 44. From a statistical point of view, the $^{226}Ra^+$ signals above 3σ reflected the actual $^{226}Ra^+$ signal in AFBs. Therefore, it can be said that the radioactive Ra was detected in the AFBs. The background signal was subtracted from $^{226}Ra^+$ signals above 3σ, and the resulting $^{226}Ra^+$ signals were converted to Ra concentration using the Ra calibration curve from the July 2022 session in figure 30. The resulting Ra concentrations were between 4.57 and 6.09 ppb and 167.15-191.67 Bq (fig. 45).
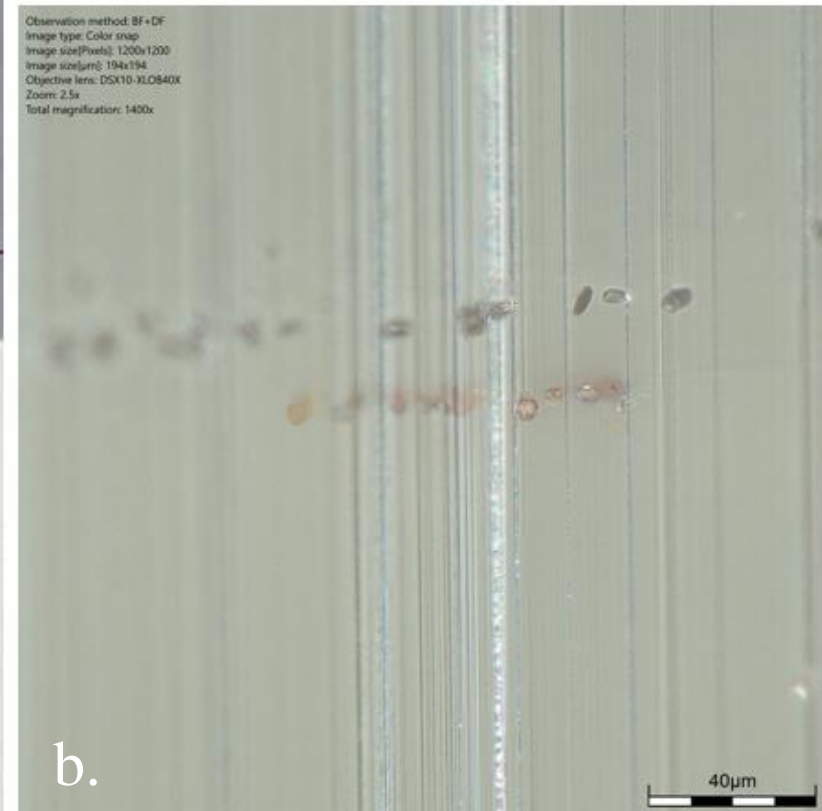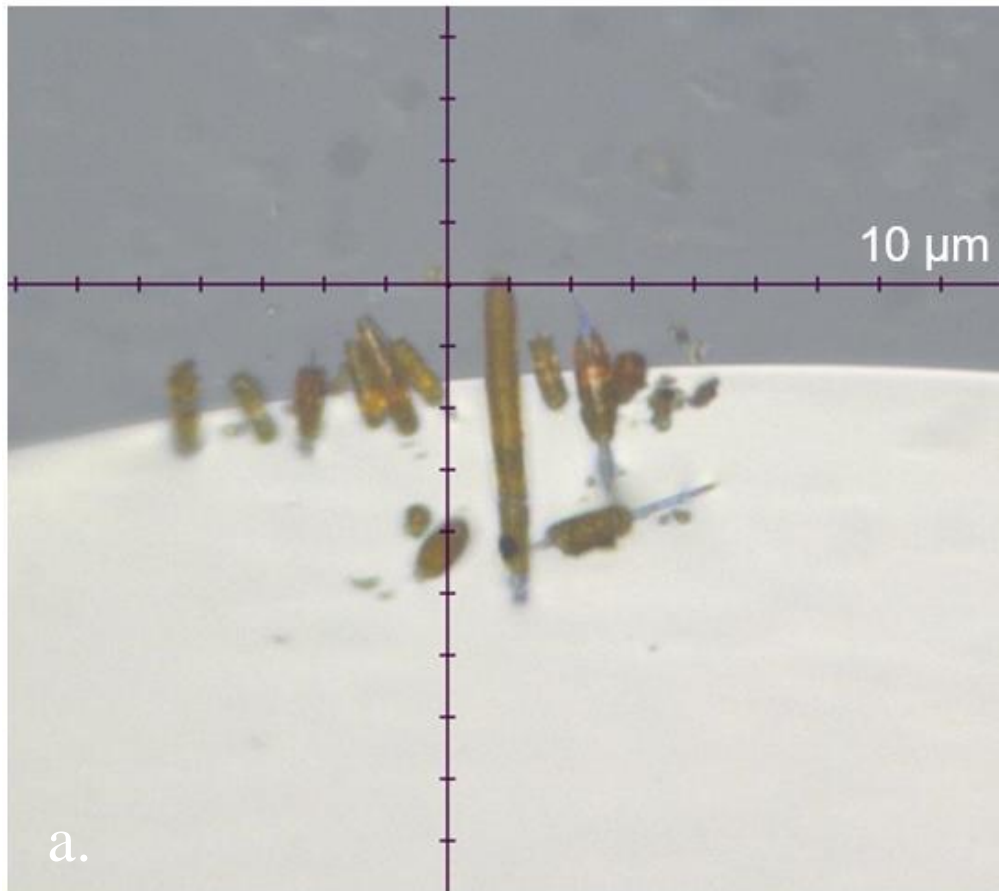
Figure 40. Optical microscope images of AFBs prepared for SIMS analyses: a. AFBs picked up by a needle from the dried lung sample and lined up on the border of the resin glue, b. Exposed AFBs by ultra-microtome.
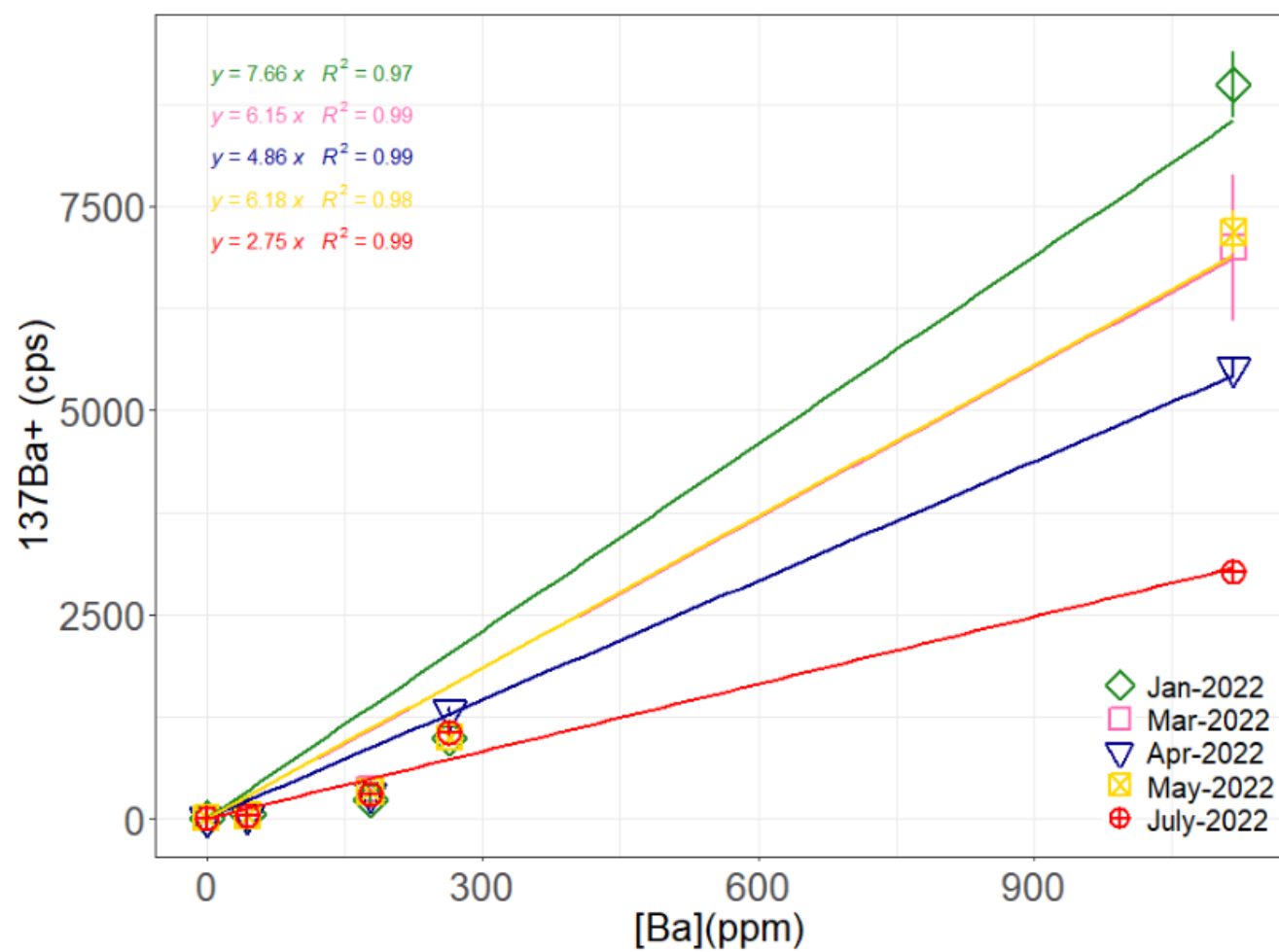
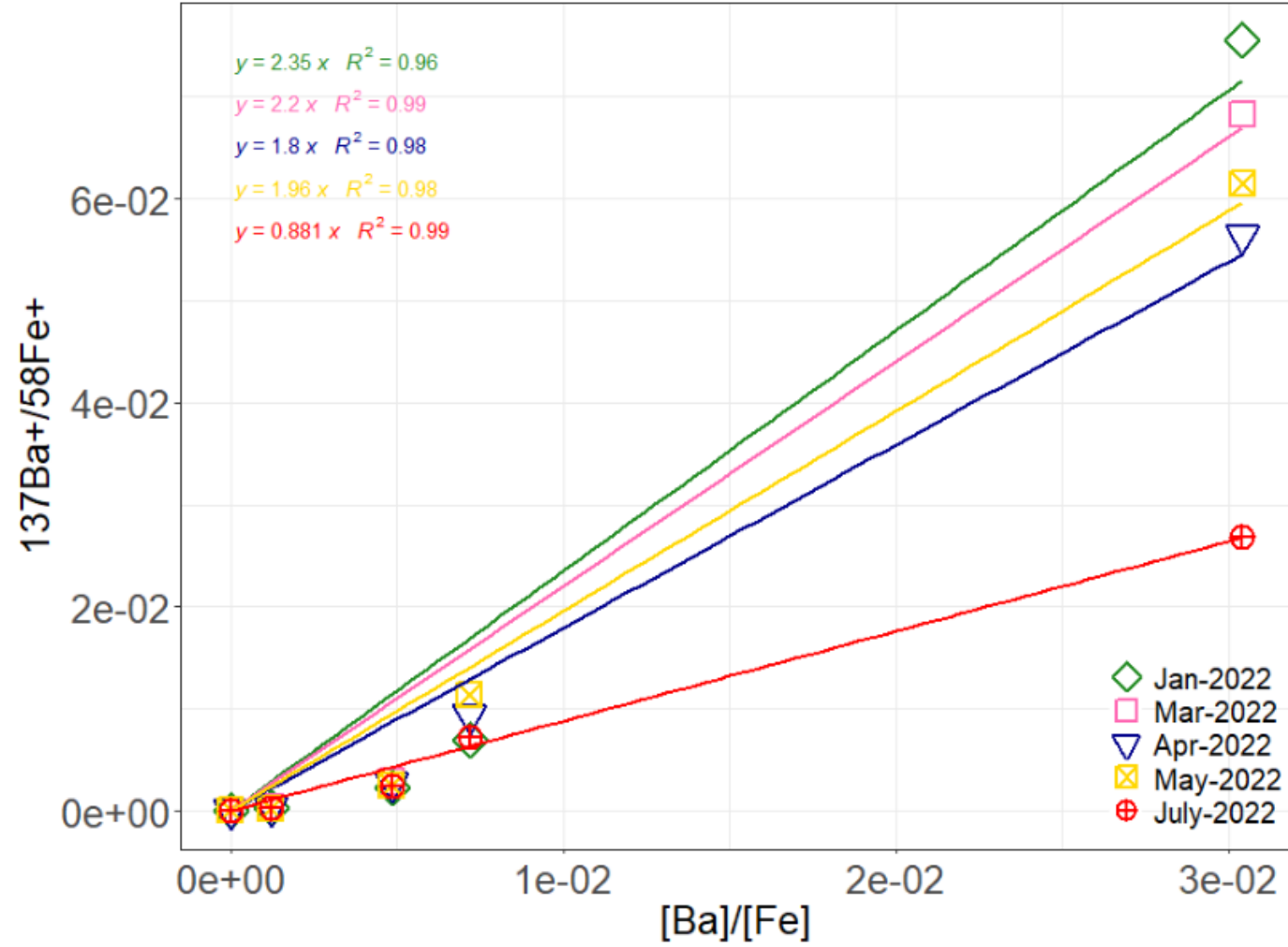Figure 41. Calibration curves for $^{137}Ba^+$ obtained for each session.

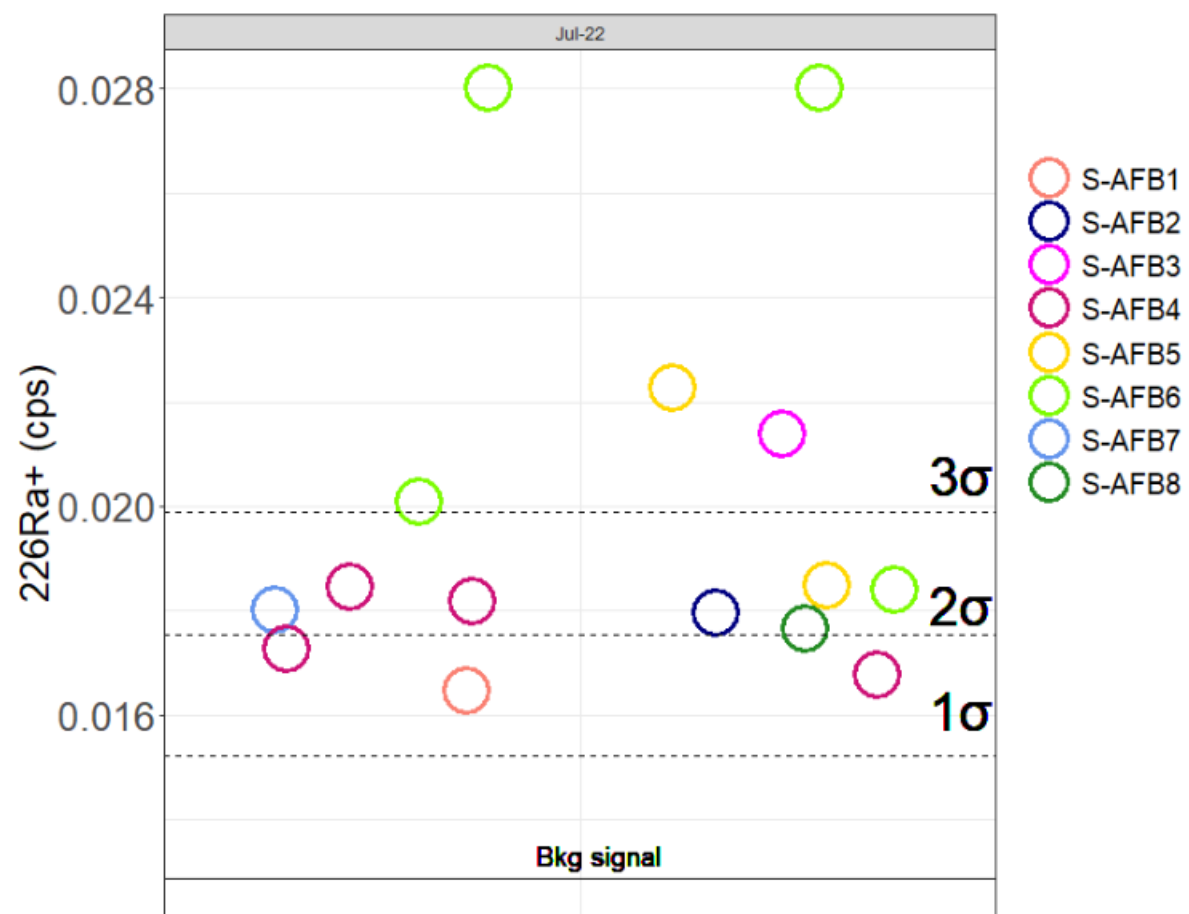Figure 42. Calibration curves for $^{137}Ba^+$ normalised to $^{58}Fe^+$ obtained for each session.

Figure 43. Ba concentrations calculated based on a. the $^{137}Ba^+$ calibration curve and b. $^{137}Ba^+/^{58}Fe^+$ calibration curve. The dashed line in both figures represents the Ba concentration obtained in this study by bulk lung sample analysis in ICP-Ms, from which the AFBs originate.

Figure 44. ^{226}Ra$^+$ intensities of analysed AFBs above the background signal (solid horizontal line) and 3σ, 2σ and 1σ of the standard deviations of the background signal (dotted horizontal lines).
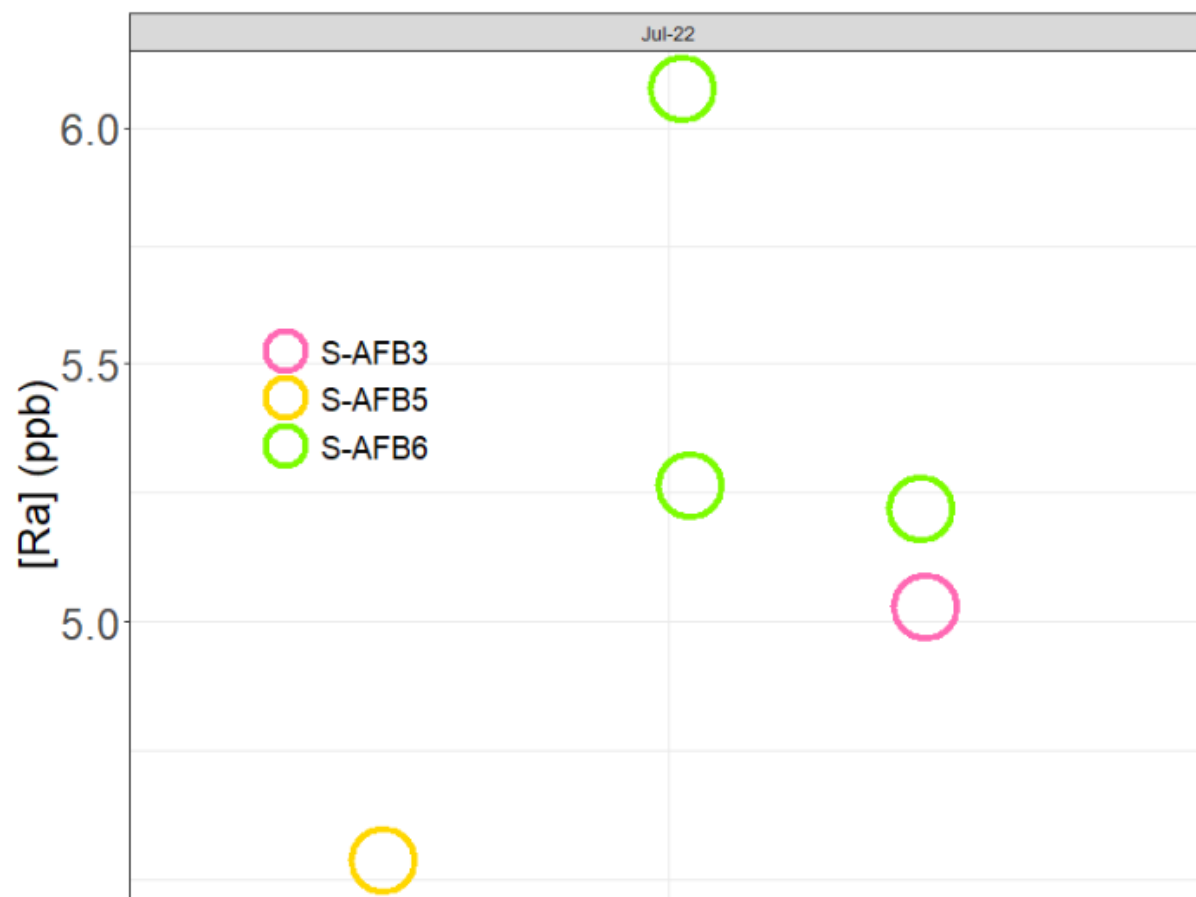
Figure 45. Ra concentrations at ppb level of analysed AFBs.

Equations for estimation of radiation damage to the lungs

The following series of equations[124] were used for:

estimation of the number of nuclei (N)

$$N = \frac{M}{m_{226Ra}} N_A \qquad \text{Equation 1}$$

where N is the number of Ra nuclei in a total mass (M) of Ra, m_{226Ra} is the atomic mass of ^{226}Ra and N_A is the Avogadro constant.

The number of nuclei at a certain time (N_t) is given by the integration with respect to time

$$N_t = N_{(0)} e^{-\lambda t} \qquad \text{Equation 2}$$

where N_t is the number of nuclei after t time has passed, $N_{(0)}$ is the number of nuclei at $t = 0$ and λ is the decay constant.

ΔN is the number of nuclei that decayed after 1 year (1y).

$$\Delta N = N_{(0)} - N_{1y} \qquad \text{Equation 3}$$

where N_{1y} is the number of nuclei at $t = 1$ year.

The decay constant (λ)

$$\lambda = \frac{\ln 2}{t(^1/_2)} \qquad \text{Equation 4}$$

where $t(^1/_2)$ is the half-life of the isotope.

Conversion of the ^{226}Ra α energy of 4.784 MeV into joules (J)

$$E_\alpha = 4.784 \text{ MeV} \times 1.6022 \times 10^{-13} \text{J/MeV} = 7.665 \times 10^{-13} \text{J} \qquad \text{Equation 5}$$

where E_α is the energy in J for an α-particle resulting from the decay of ^{226}Ra.

The absorbed dose for an organ or a tissue is D_T, defined by the amount of energy absorbed (E_T) per unit mass of the organ or the tissue (mass is defined as m_T).

$$E_T = \Delta N E_\alpha \qquad \text{Equation 6}$$

$$D_T = \frac{E_T}{m_T} \qquad \text{Equation 7}$$

The SI unit of the absorbed dose is gray (Gy) where $1 \text{ Gy} = 1 \text{ J}/_{kg}$.

The effective dose (D) is estimated from the absorbed dose (D_T), reflecting the radiation sensitivity of the tissue or organ of interest

$$D = D_T W_R W_T \qquad \text{Equation 8}$$

where W_R is the radiation weighting factor, that of α particle being 20[124]. W_T is the tissue weighting factor, that of the lungs being 0.12[124]. The SI unit of D is the sievert (Sv). The effective dose with the Sv unit represents the radiation effect on the human body.

Whole lung estimates of the effective dose

The 8 analysed AFBs in SIMS belonged to the smoker patient S1. Therefore, the Ra concentrations from all these analysed AFBs that were above 3σ of the standard deviation of the background signal, were averaged (5.22×10^{-9} g/g) and multiplied by the weight of ferritin in each AFB (1.7×10^{-11}g)[1], the weight of the lung (1000 g)[125], and the number of AFBs in the patient's lung sample (Table 1). The estimated Ra in the ferritin of all analysed AFBs in patient S1 was 2.84×10^{-11} g. The number of total Ra nuclei in the lungs was calculated using eq. 1, resulting in 7.57×10^{10} nuclei, of which 3.28×10^7 nuclei decay yearly (Eqs. 2, 3 and 4). The yearly generated energy was estimated to be 2.478×10^{-5} J (Eqs. 5 and 6), which corresponded to the energy of the nuclei. The energy of the nuclei was divided by the weight of the lungs (1 kg) in order to obtain the absorbed dose of 2.478×10^{-5} J/kg (Eq. 7) or gray. The effective dose to the lungs was calculated by multiplying the absorbed dose by the weighting factor of the lung ($W_T = 0.12$)[124] and the radiation weighting factor of α-particles ($W_R = 20$)[124] (Eq. 8). Thus, the effective dose per year was 5.95×10^{-5} Sv (Sievert). The whole lung receives a yearly effective dose of 0.0595 mSv on average.

Localised estimates of effective dose

For the estimation of the amount of Ra nuclei in each AFB, the Ra concentrations of the AFBs were multiplied by the weight of ferritin per AFB (1.7×10^{-11}g)[1]. From the resulting Ra concentration per AFB ferritin, the number of Ra nuclides was deduced for each analysis of AFB3 (n=1), AFB5 (n=1) and AFB6 (n=3). Subsequently, the number of decays per year of ^{226}Ra was calculated. The number of decays was then used to deduce the energy and the effective dose in the local volume surrounding one AFB.

The travel distance of an α-particle is 40 µm[126]. The volume of a sphere representing the 40 µm region around one AFB which an α-particle can penetrate was calculated for the estimation of the volume of lung tissue that was affected by the ionising radiation from the decay of ^{226}Ra. In turn, the volume of lung tissue was converted to a mass using the average lung tissue density for a smoker of 0.292 g/cm^3 [127]. Using all the above information, the localised absorbed doses of lung tissue within 40 µm of the AFBs were calculated (Eq. 7). The effective doses (Eq. 8) were between 2.08 and 2.77 mSv per year, depending on the AFB analysed, each effective dose being more than double than the public exposure limit. Table 7 shows the public exposure limit, the whole lung effective dose and the Ra concentrations and effective doses of the AFBs.

	[Ra] (ng/g)	Effective dose (mSv/year)
Public exposure limit		1
Whole Lung dose		0.0595
Local dose of AFB3	5.01	2.28
Local dose of AFB5	4.57	2.08
Local dose of AFB6-1	5.2	2.36
Local dose of AFB6-2	5.24	2.38
Local dose of AFB6-3	6.09	2.77

Table 7. Public exposure limit effective dose, total lung effective dose, and Ra concentrations and effective doses for each analysed AFB (localised effective dose) of patient S.

5.4 Discussion

5.4.1 REE analysis implications

In figure 38, the secondary yield distribution for metal and oxide elements of the ferri-7 series is shown in comparison to a previously analysed silicate standard series, which was extensively studied within the laboratory. The Fh standard series had metal and oxide yields 1-60 % lower than the silicate standards due to matrix effects. However, both standard series assumed similar distribution patterns of the secondary ion yields. In addition, oxide yields of neighbouring isotopes, such as ^{143}NdO and ^{144}NdO, showed close yield values. Therefore, the REE Fh standard series was deemed suitable for future sample analyses.

The high abundance of Ba hinted toward the possibility of a high Ra abundance since Ba and Ra behave similarly due to being part of the same group in the periodic table. Due to the importance of constraining the role of Ra in the onset of MM and the significant amount of time and resources it takes to prepare and analyse AFBs using SIMS, the focus was shifted to the analysis of Ra in the AFBs.

5.4.2 Ra analysis implications

For the AFB in-situ analysis of Ra, a new method for mounting the AFBs was developed. The AFBs were encased in resin and microtomed from the top to expose their interiors, similar to TEM analysis but with most initial lengths retained. Therefore, sufficient AFB material was available on the scale of microns in order to achieve a complete and successful analysis.

Furthermore, the AFB sample mount of the July 22 session was acid washed in 0.01 M HCl for 15 seconds to remove any possible contamination that had accumulated during microtoming. The acid washing was tested on ref-ferri-Ra0. Accordingly, the acid washing proved effective, observed through the improved background signal for the July 22 session.

In chapter 3 it was mentioned that the bulk lung samples contained not only AFBs but also lung artefacts, thus reflecting a diluted AFB Ra concentration by the lung artefacts, which prompted the necessity of an in-situ analysis for AFBs. Accordingly, the Ba concentrations from SIMS analysis that measured above the Ba bulk concentration would reflect the true undiluted Ba concentrations of the AFBs. The Ba concentrations of AFBs were estimated from the ^{137}Ba$^+$ calibration curve (Fig. 41) and ^{137}Ba$^+$/^{58}Fe$^+$ calibration curve (Fig. 42). The last obtained calibration curve shows great linearity, which reflected the final well-developed analytical conditions. Ba concentrations obtained from the ^{137}Ba$^+$ signals (Fig. 43a) were lower than that of bulk lung sample concentration obtained by ICP-MS. However, Ba concentrations obtained from the ^{137}Ba$^+$/^{58}Fe$^+$ signals (Fig. 43b) were higher than that of bulk lung sample concentration obtained by ICP-MS. As the Ba concentrations obtained from the ^{137}Ba$^+$/^{58}Fe$^+$ signals were above ICP-MS, it enforced the original plan of determination of Ra concentrations based on the ^{226}Ra$^+$ signals normalised to ^{58}Fe$^+$, from the ^{226}Ra$^+$/^{58}Fe$^+$ calibration curves (Fig. 30).

There was a 0.1% probability that ion signals above 3σ are background signals. Therefore, it can be said that the radioactive Ra was detected in the AFBs for those above the 3σ of the background signal. The Ra concentrations of the resulting signals from AFBs were estimated, for which whole lung effective dose and localised effective dose were calculated.

5.4.3 Whole lung and localised radiation

According to ICRP,2007[128], the public exposure limit is 1 mSv per year. The estimated annual effective dose was about 17 times lower than the public exposure limit. However, this value was calculated assuming the Ra was homogenously spread throughout the lungs. In reality, the Ra is concentrated in AFBs within small regions of the lungs. Therefore, a hotspot model taking into account the heterogenous distribution of radiation hotspots was developed.

Interestingly, Toohey et al., 1984[2] represents the only study to have detected ^{226}Ra in the lungs of an individual, in this case, a uranium mill worker. Ra within the lung has a biological half-life of 120 days, the initial inhaled amount representing around 180 Bq and it was concluded that dust particles with Ra were inhaled in the lung and excreted without depositing elsewhere in the body.

While the effective dose of ionising radiation calculated for the whole lungs is below the safety limit, the reality is that α-particles will only penetrate ~40 µm[126] into the tissue surrounding the AFBs. Therefore, the localised effective radiation dose may be much higher, but does not affect the entirety of the lung tissue. Furthermore, only the α decay energy from ^{226}Ra to ^{222}Rn was considered, as the rest of the isotopes in the decay chain until ^{210}Pb have short decay times. In order to consider α decay energies from ^{210}Pb (half-life=22y) to the stable isotope ^{206}Pb, their concentrations within the AFBs should be evaluated.

The radiation exposure values of the localised effective doses are highly significant and support the theory that ionising radiation could induce carcinogenesis in the vicinity of AFBs. Once cancer cells have formed, they could be transported via the lymph system or blood vessels to other areas of the lungs and surrounding tissue, such as the mesothelium. Therefore, the effects of ^{226}Ra on the development of MM are likely significant and should be taken very seriously.

The formation of AFBs was previously discussed in chapter 2 (Fig. 9). To summarise, the inhaled asbestos fibres are unsuccessfully phagocytosed by the alveolar macrophages (AM), leading to AM death. The AM remnants (containing Fe inclusions as well) accrete on the fibres which attract lung components and mucopolysaccharides, the latter having an affinity to Fe resulting in Fe accretion. Smoking patients would have AM laden with Fe due to cigarette smoke complexing Fe, therefore their AFBs would be rich in Fe (in the form of ferrihydrite (Fh)), dense and with smaller diameters. Non-smoking patients will have AFBs less rich in Fe, more porous and with larger diameters, as it depends only on the available iron in the lung environment.

Fe oxyhydroxides, such as Fh, are known to adsorb Ra[67]. Therefore, the AFB coat, which is mostly composed of Fh, is likely the main reservoir of Ra. Accordingly, the inhaled or ingested particles of Ra are adsorbed by the AFB Fh coat instead of being cleared by the lungs.

Moreover, ingestion of food products commonly consumed by the Japanese population such as seaweed[76], rice[74], leafy vegetables[75], eggs and green tea[77], provides a constant supply of Ra that can accumulate over years and decades. Asbestos fibres contain traces of Ra as well[72] which are insufficient to trigger tumour incidence but can be included in the overall Ra flux to the AFBs.

Furthermore, smokers can inhale a portion of Ra as well, originating from the tobacco plants which are heavily fertilised with phosphate fertilisers rich in radionuclides, such as U and Ra[78]. Furthermore, the major form of bedrock in SW Japan is granite[74], so the amount of radiation is larger in this area than in the NE area of Japan. Therefore, with the radioactive soil coupled with the radioactive fertilisers, the tobacco plants are able to adsorb a large number of radionuclides. Accordingly, when one cigarette is smoked, 75% of the nuclides are transferred to the lungs[80]. One other minor source of Ra is ingestion of natural radioactive elements, Japan having a committed effective dose from this kind of ingestion about 4 times higher than the world average, of 0.41 mSv per year[77].

Considering that osteosarcoma induction involves hotspots and diffuse radioactivity of Ra[70], both bone and lung cells have similar sensitivities to radiation exposure[71], a heterogenous distribution of Ra hotspots within the lungs might likely occur. Several sources of Ra accumulate onto the AFBs, creating Ra hotspots and leading to lung carcinoma and/or MM induction.

5.4.4 AFB Ra Hotspot Model

After the asbestos fibres are inhaled, they eventually reach the lower lungs where they cluster in heterogeneously distributed groups, followed by AFB formation as explained in the previous model (Fig. 9). Afterwards, the AFB Fh coat adsorbs Ra obtained from ingestion of food and water, inhalation of natural radioactive elements and cigarette smoke in the case of smokers. The Ra from the mentioned sources avoids lung clearance by accumulating on the AFBs over long periods of time, eventually reaching a threshold above safety limits and causing α-particle radiation throughout the surroundings of each AFB, which is termed a hotspot (Fig. 46b and c). The hotspots composed of several AFBs are heterogeneously distributed in the lungs; therefore, several areas of the lung are able to maintain normal functions while the hotspot areas are irradiated (Fig. 46a). The mesothelial cells within the vicinity of the AFBs immediately die due to the large radioactivity, while cells further from the AFBs are radiated with diffused radioactivity which may cause deregulations in the DNA of the cells (Fig. 46c). Damaged DNA damage within the cell can be either repaired by a specialised repairing system within the cell or the cell can continue replicating the damaged DNA, thus yielding cancerous cells (Fig. 46d). The cancerous cells collectively contribute to deregulations in the mesothelium, leading to the incidence of MM (Fig 46e). As the cancerous cells form tumours within the mesothelium and lung, these cells can metastasise through the blood flow to other locations such as the bones[129,130].
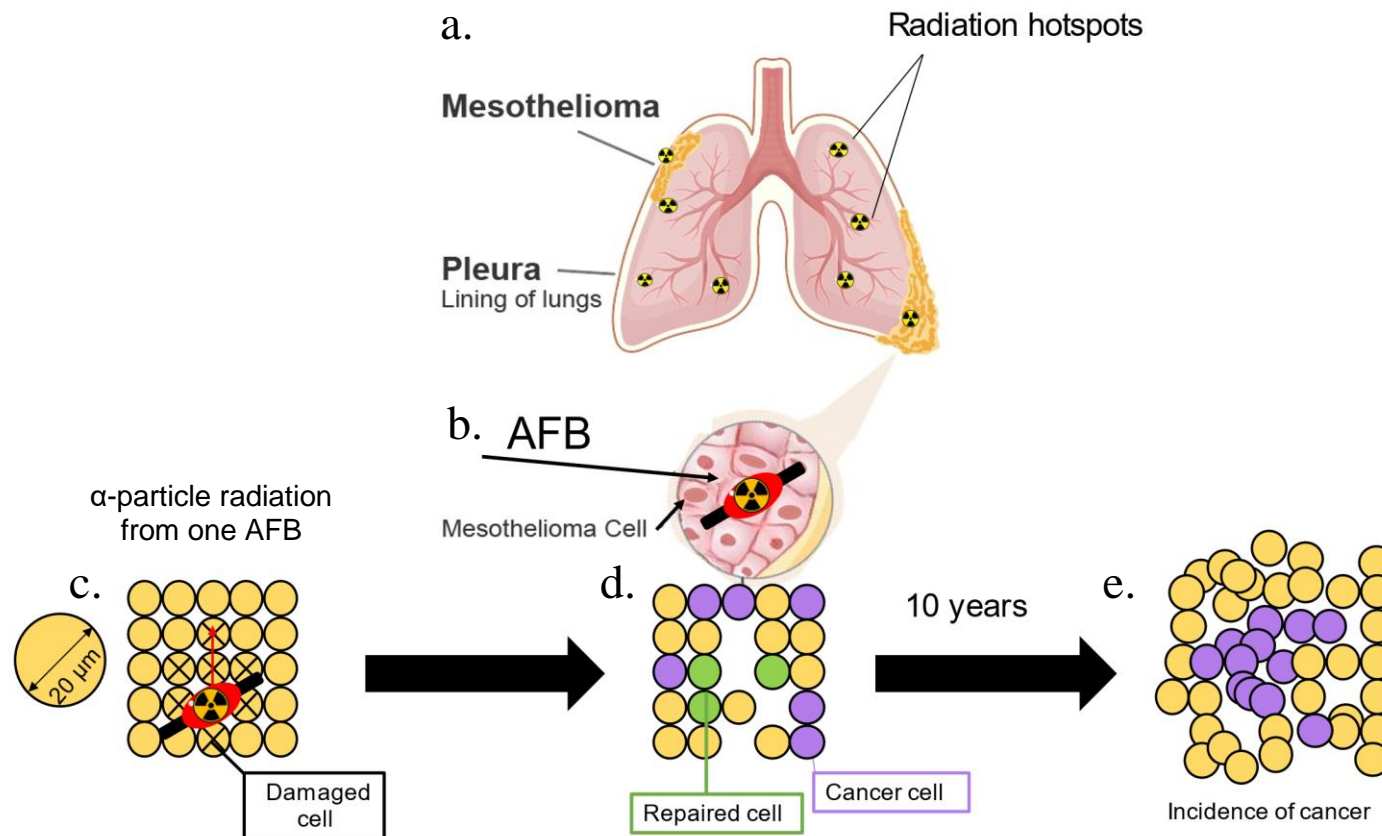
Figure 46. An illustration of the AFB Ra hotspot radiation model is described here: **a.** Heterogenous distribution of AFB Ra hotspots in the lungs, the hotspots continuously damage the tissue while the unaffected lung tissue maintains normal lung function; **b.** A simplified view of an AFB Ra hotspot; **c.** Graphical view of the impact of the α-particle radiation from an AFB with Ra to the surrounding mesothelial cells; **d.** α-particle radiation results in cell death in its proximity, cells with damaged DNA that become cancerous cells and damaged cells that are repaired through existing DNA repair systems; **e.** The proliferation of cancer cells leads to the incidence of cancer and tumorigenesis.

5.5 Conclusion

The analytical conditions of the Ra analysis were further improved for successful Ra detection in AFBs. The $^{226}Ra^+$ mass centring was fulfilled by using $^{58}Fe^+$ for internal mass calibration. In addition, an AFB mounting protocol was developed.

Having enough AFB material to analyse led to the detection of 4.57-6.09 ppb of Ra. Based on the detected Ra concentrations, the calculated Ra within the lungs of the smoker patient S1 had an annual effective dose of 6.03×10^{-2} mSv, which is 300 times lower than the public exposure limit of 1 mSv. On the other hand, localised effective doses of the AFBs were between 2.08 and 2.77 mSv, which are higher than the public exposure limit of 1 mSv.

The high annual localised effective doses, strongly indicate that ionising radiation is critical in MM progression, especially through DNA damage and chromosomal abnormalities.

An AFB Ra hotspot model was proposed where heterogeneously distributed hotspots in the lung cause constant tissue damage through radiation resulting in damaged DNA that proliferates, leading to cancer incidence. The unaffected lung tissue maintains normal function of the lungs which may explain the long latency of MM and delayed diagnosis.

6. CHAPTER 6 – Conclusions

- ICP-MS analysis of bulk lung samples revealed the presence of genotoxic elements such as Cd, U, and Ra. Heterogeneity of the lung samples was observed among studies suggesting a sample bias as the lung samples are aliquots with a heterogeneous distribution of lung particles and AFBs. Therefore, in-situ analysis of AFBs was proposed for the determination of their elemental abundances free of any lung particles.

- An Fh standard creation method was developed with which two homogenous Fh standard series were created for trace element and Ra analysis of AFBs.

- The AFBs that were analysed by SIMS showed high elemental abundances of Sr and Ba which are known to associate with Ra, giving strong suggestions that Ra is present within the AFBs.

- Ra was detected in AFBs, which was possible due to newly developed sample preparation techniques and analytical methods. The effective dose of the detected Ra was above the safety limit, indicating that ionising radiation has a role in MM development. An AFB Ra hotspot model was drawn based on the observed Ra concentrations and calculated localised effective doses of radiation. The model proposes that due to the heterogeneous distribution of AFBs, α-particle radiation is localised to small regions in the lung, leading to DNA damage and cancer incidence. The heterogeneity of the radiation exposure allows the existence of healthy lung tissues in unexposed areas which maintain normal lung function. Accordingly, the persistence of healthy lung tissue may explain the long latency period of the disease and its delayed diagnosis.

7. Future Work

- A more significant number of patients and AFBs is necessary for a more robust investigation of Ra distribution in AFBs using SIMS.

- Furthermore, the elements with high adsorption rates onto Fh such as genotoxic elements Ce, Cd and U should be investigated for their possible roles in MM incidence.

- Cigarette smoke is known to be rich in radioactive ^{210}Po. As such, this element should also be investigated, as it may contribute to α-particle radiation and thus initiation of MM.

References

1   Nakamura E, Makishima A, Hagino K, Okabe K. Accumulation of radium in ferruginous protein bodies formed in lung tissue: association of resulting radiation hotspots with malignant mesothelioma and other malignancies. *Proc Jpn Acad Ser B Phys Biol Sci* 2009; **85**: 229–239.

2   Toohey RE, Sha JY, Umezis PW, Hwang EY. An unusual case of radium exposure. *Argonne Natl Lab Environ Res Div Annu Rep July 1982–June 1983* 1984; **ANL**-**83**-**100**: 15–20.

3   Nagai H, Ishihara T, Lee WH, Ohara H, Okazaki Y, Okawa K *et al.* Asbestos surface provides a niche for oxidative modification. *Cancer Sci* 2011; **102**: 2118–2125.

4   Wachowski L, Domka L. Sources and Effects of Asbestos and Other Mineral Fibres Present in Ambient Air. *Polish J Environ Stud* 2000; **9**: 443–454.

5   Ghio AJ, Churg A, Roggli VL. Ferruginous bodies: Implications in the mechanism of fiber and particle toxicity. *Toxicol Pathol* 2004; **32**: 643–649.

6   Ross M, Langer AM, Nord GL, Nolan RP, Lee RJ, Van Orden D *et al.* The mineral nature of asbestos. *Regul Toxicol Pharmacol* 2008; **52**: 26–30.

7   Toyokuni S. Iron overload as a major targetable pathogenesis of asbestos-induced mesothelial carcinogenesis. *Redox Rep* 2014; **19**: 1–7.

8   Pass HI, Carbone M, Vogelzang NJ. *Malignant mesothelioma: Advances in pathogenesis, diagnosis, and translational therapies*. Springer-Verlag: New York, 2005 doi:10.1007/0-387-28274-2.

9   Aust AE, Cook PM, Dodson RF. Morphological and chemical mechanisms of elongated mineral particle toxicities. *J Toxicol Environ Heal - Part B Crit Rev* 2011; **14**: 40–75.

10   Jiang L, Akatsuka S, Nagai H, Chew SH, Ohara H, Okazaki Y *et al.* Iron overload signature in chrysotile-induced malignant mesothelioma. *J Pathol* 2012; **228**: 366–377.

11   Hawthorne FC. The crystal chemistry of amphiboles. *Can Mineral* 1983; **21**.

12   Catherine H, Skinner W. Mineralogy of Asbestos Minerals. *Indoor Built Environ* 2003; **12**: 385–389.

13   Harper M, Lee EG, Slaven JE, Bartley DL. An inter-laboratory study to determine the effectiveness of procedures for discriminating amphibole asbestos fibers from amphibole cleavage fragments in fiber counting by phase-contrast microscopy. *Ann Occup Hyg* 2012; **56**: 645–659.

14   Pascolo L, Gianoncelli A, Kaulich B, Rizzardi C, Schneider M, Bottin C *et al.* Synchrotron soft X-ray imaging and fluorescence microscopy reveal novel features of asbestos body morphology and composition in human lung tissues. *Part Fibre Toxicol* 2011; **8**: 1–11.

15   Jiang L, Toyokuni S. Elucidation of asbestos-induced mesothelial carcinogenesis toward its prevention. *Genes Environ* 2011; **33**: 4–9.

16   Di Giuseppe D, Zoboli A, Vigliaturo R, Gieré R, Bonasoni MP, Sala O *et al.* Mineral fibres and asbestos bodies in human lung tissue: A case study. *Minerals* 2019; **9**: 1–21.

17   Kuang Y, Wang Q. Iron and lung cancer. *Cancer Lett* 2019; **464**: 56–61.

18   Sukiennicki GM, Marciniak W, Muszyńska M, Baszuk P, Gupta S, Białkowska K *et al.* Iron levels, genes involved in iron metabolism and antioxidative processes and lung cancer incidence. *PLoS One* 2019; **14**: e0208610.

19   Winter WE, Bazydlo LAL, Harris NS. The molecular biology of human iron metabolism. *Lab Med* 2014; **45**: 92–102.

20   Bardelli F, Veronesi G, Capella S, Bellis D, Charlet L, Cedola A *et al.* New insights on the biomineralisation process developing in human lungs around inhaled asbestos

fibres. *Sci Rep* 2017; **7**: 1–11.

21   Harrison PM, Arosio P. The ferritins: Molecular properties, iron storage function and cellular regulation. *Biochim Biophys Acta - Bioenerg* 1996; **1275**: 161–203.

22   Turi JL, Yang F, Garrick MD, Piantadosi CA, Ghio AJ. The iron cycle and oxidative stress in the lung. *Free Radic Biol Med* 2004; **36**: 850–857.

23   Liu G, Debnath S, Paul KW, Han W, Hausner DB, Hosein HA *et al.* Characterization and surface reactivity of ferrihydrite nanoparticles assembled in ferritin. *Langmuir* 2006; **22**: 9313–9321.

24   Aung W, Hasegawa S, Furukawa T, Saga T. Potential role of ferritin heavy chain in oxidative stress and apoptosis in human mesothelial and mesothelioma cells: Implications for asbestos-induced oncogenesis. *Carcinogenesis* 2007; **28**: 2047–2052.

25   Michel FM, Ehm L, Antao SM, Lee PL, Chupas PJ, Liu G *et al.* The Structure of Ferrihydrite, a Nanocrystalline Material. *Science (80-)* 2007; **316**: 1726–1729.

26   Michel FM, Barron V, Torrent J, Morales MP, Serna CJ, Boily J-F *et al.* Ordered ferrimagnetic form of ferrihydrite reveals links among structure, composition, and magnetism. *Proc Natl Acad Sci* 2010; **107**: 2787–2792.

27   Chanvorachote P, Luanpitpong S. Iron induces cancer stem cells and aggressive phenotypes in human lung cancer cells. *Am J Physiol - Cell Physiol* 2016; **310**: C728–C739.

28   Janney DE. Transmission Electron Microscopy of Synthetic 2- and 6-Line Ferrihydrite. *Clays Clay Miner* 2000; **48**: 111–119.

29   Toyokuni S. Iron addiction with ferroptosis-resistance in asbestos-induced mesothelial carcinogenesis: Toward the era of mesothelioma prevention. *Free Radic Biol Med* 2019; **133**: 206–215.

30   Governa M, Rosanda C. A histochemical study of the asbestos body coating. *Br J Ind Med* 1972; **29**: 154–159.

31   Allison AC. Pathogenic Effects of Inhaled Particles and Antigens. *Ann N Y Acad Sci* 1974; **221**: 299–308.

32   McLemore TL, Mace ML, Roggli V, Marshall M V., Lawrence EC, Wilson RK *et al.* Asbestos body phagocytosis by human free alveolar macrophages. *Cancer Lett* 1980; **9**: 85–93.

33   Churg AM, Warnock ML. Asbestos and other ferruginous bodies. Their formation and clinical significance. *Am J Pathol* 1981; **102**: 447–456.

34   Richards RJ, Curtis CG. Biochemical and cellular mechanisms of dust-induced lung fibrosis. *Environ Health Perspect* 1984; **55**: 393–416.

35   Hamilton RF, Thakur SA, Holian A. Silica binding and toxicity in alveolar macrophages. *Free Radic Biol Med* 2008; **44**: 1246–1258.

36   Markowitz S. Asbestos-related lung cancer and malignant mesothelioma of the pleura: Selected current issues. *Semin Respir Crit Care Med* 2015; **36**: 334–346.

37   Ghio AJ, Pavlisko EN, Roggli VL, Todd NW, Sangani RG. Cigarette Smoke Particle-Induced Lung Injury and Iron Homeostasis. *Int J COPD* 2022; **17**: 117–140.

38   Blount M, Holt PF, Leach AA. The protein coating of asbestos bodies. *Biochem J* 1966; **101**: 204–207.

39   Zhang WZ, Butler JJ, Cloonan SM. Smoking-induced iron dysregulation in the lung. Free Radic. Biol. Med. 2019; **133**: 238–247.

40   Chew SH, Toyokuni S. Malignant mesothelioma as an oxidative stress-induced cancer: An update. *Free Radic Biol Med* 2015; **86**: 166–178.

41   Pascolo L, Zabucchi G, Gianoncelli A, Kourousias G, Trevisan E, Pascotto E *et al.* Synchrotron X-ray microscopy reveals early calcium and iron interaction with crocidolite fibers in the lung of exposed mice. *Toxicol Lett* 2016; **241**: 111–120.

42   Pascolo L, Gianoncelli A, Rizzardi C, De Jonge M, Howard D, Paterson D *et al.* Focused X-Ray Histological Analyses to Reveal Asbestos Fibers and Bodies in Lungs and Pleura of Asbestos-Exposed Subjects. *Microsc Microanal* 2016; **22**: 1062–1071.

43   Yoshida M, Minagawa S, Araya J, Sakamoto T, Hara H, Tsubouchi K *et al.* Involvement of cigarette smoke-induced epithelial cell ferroptosis in COPD pathogenesis. *Nat Commun* 2019; **10**. doi:10.1038/s41467-019-10991-7.

44   Zhang V, Nemeth E, Kim A. Iron in lung pathology. *Pharmaceuticals* 2019; **12**: 1–11.

45   Ghio AJ, Stonehuerner J, Richards J, Devlin RB. Iron Homeostasis in the Lung Following Asbestos Exposure. *Antioxid Redox Signal* 2008; **10**: 371–378.

46   Klebe S, Leigh J, Henderson DW, Nurminen M. Asbestos, smoking and lung cancer: An update. Int. J. Environ. Res. Public Health. 2020; **17**. doi:10.3390/ijerph17010258.

47   Hanahan D, Weinberg RA. Hallmarks of cancer: The next generation. Cell. 2011; **144**: 646–674.

48   Magnani C, Dalmasso P, Biggeri A, Ivaldi C, Mirabelli D, Terracini B. Increased risk of malignant mesothelioma of the pleura after residential or domestic exposure to asbestos: A case-control study in Casale Monferrato, Italy. *Environ Health Perspect* 2001; **109**: 915–919.

49   Godleski JJ. Role of asbestos in etiology of malignant pleural mesothelioma. *Thorac Surg Clin* 2004; **14**: 479–487.

50   Carbone M, Ly BH, Dodson RF, Pagano I, Morris PT, Dogan U a *et al.* Malignant mesothelioma: Facts, Myths, and Hypotheses. *J Cell Physiol* 2012; **227**: 44–58.

51   Hirano S, Suzuki KT. Exposure, metabolism, and toxicity of rare earths and related compounds. *Environ Health Perspect* 1996; **104**: 85–95.

52   Censi P, Tamburo E, Speziale S, Zuddas P, Randazzo LA, Punturo R *et al.* Yttrium and lanthanides in human lung fluids, probing the exposure to atmospheric fallout. *J Hazard Mater* 2011; **186**: 1103–1110.

53   Pagano G, Aliberti F, Guida M, Oral R, Siciliano A, Trifuoggi M *et al.* Rare earth elements in human and animal health: State of art and research priorities. *Environ Res* 2015; **142**: 215–220.

54   Bloise A, Barca D, Gualtieri AF, Pollastri S, Belluso E. Trace elements in hazardous mineral fibres. *Environ Pollut* 2016; **216**: 314–323.

55   Dardenne K, Schäfer T, Lindqvist-Reis P, Denecke MA, Plaschke M, Rothe J *et al.* Low temperature XAFS investigation on the Lutetium binding changes during the 2-line ferrihydrite alteration process. *Environ Sci Technol* 2002; **36**: 5092–5099.

56   Hua J, Liu C, Li F, Zhu Z, Wei Z, Chen M *et al.* Effects of Rare Earth Elements' Physicochemical Properties on Their Stabilization during the Fe(II)aq-induced Phase Transformation of Ferrihydrite. *ACS Earth Sp Chem* 2019; **3**: 895–904.

57   Tiberg C, Sjöstedt C, Persson I, Gustafsson JP. Phosphate effects on copper(II) and lead(II) sorption to ferrihydrite. *Geochim Cosmochim Acta* 2013; **120**: 140–157.

58   Liu J, Zhu R, Liang X, Ma L, Lin X, Zhu J *et al.* Synergistic adsorption of Cd(II) with sulfate/phosphate on ferrihydrite: An in situ ATR-FTIR/2D-COS study. *Chem Geol* 2018; **477**: 12–21.

59   Michon J, Frelon S, Garnier C, Coppin F. Determinations of uranium(VI) binding properties with some metalloproteins (transferrin, albumin, metallothionein and ferritin) by fluorescence quenching. *J Fluoresc* 2010; **20**: 581–590.

60   Price DJ, Joshi JG. Ferritin. Binding of beryllium and other divalent metal ions. *J Biol Chem* 1983; **258**: 10873–80.

61   Komárek M, Antelo J, Králová M, Veselská V, Číhalová S, Chrastný V *et al.* Revisiting models of Cd, Cu, Pb and Zn adsorption onto Fe(III) oxides. *Chem Geol* 2018; **493**: 189–198.

62   Sajih M, Bryan ND, Livens FR, Vaughan DJ, Descostes M, Phrommavanh V *et al.* Adsorption of radium and barium on goethite and ferrihydrite: A kinetic and surface complexation modelling study. *Geochim Cosmochim Acta* 2014; **146**: 150–163.

63   Chen MA, Kocar BD. Radium Sorption to Iron (Hydr)oxides, Pyrite, and Montmorillonite: Implications for Mobility. *Environ Sci Technol* 2018; **52**: 4023–4030.

64   Trivedi P, Dyer JA, Sparks DL. Lead sorption onto ferrihydrite. 1. A macroscopic and spectroscopic assessment. *Environ Sci Technol* 2003; **37**: 908–914.

65   Rout K, Mohapatra M, Anand S. 2-Line ferrihydrite: Synthesis, characterization and its adsorption behaviour for removal of Pb(ii), Cd(ii), Cu(ii) and Zn(ii) from aqueous solutions. *Dalt Trans* 2012; **41**: 3302–3312.

66   IAEA. The environmental behaviour of radium. *J Environ Radioact* 1991; **13**: 263–264.

67   IAEA. Behaviour of Radium : Revised Edition. *Environ Behav radium* 2014; : 267.

68   Thakur P, Ward AL, González-Delgado AM. Optimal methods for preparation, separation, and determination of radium isotopes in environmental and biological samples. J. Environ. Radioact. 2021; **228**. doi:10.1016/j.jenvrad.2020.106522.

69   Abergel R, Aris J, Bolch WE, Dewji SA, Golden A, Hooper DA *et al.* The enduring legacy of Marie Curie: impacts of radium in 21st century radiological and medical sciences. Int. J. Radiat. Biol. 2022; **98**: 267–275.

70   Darby SC, Council NR. Health Risks of Radon and Other Internally Deposited Alpha-Emitters-BEIR IV. *Biometrics* 1989; **45**: 1341.

71   Raabe OG. Concerning the health effects of internally deposited radionuclides. *Health Phys* 2010; **98**: 515–536.

72   Harley NH, Cohen BS, Pasternack BS, Fisenne IM, Rohl AN. Radioactivity in asbestos. *Environ Int* 1978; **1**: 161–165.

73   Greeman DJ, Rose AW, Washington JW, Dobos RR, Ciolkosz EJ. Geochemistry of radium in soils of the Eastern United States. *Appl Geochemistry* 1999; **14**: 365–385.

74   UCHIDA S, TAGAMI K. Transfer of Radium-226 from Soil to Rice: A Comparison of Sampling Area Differences. *J Nucl Sci Technol* 2009; **46**: 49–54.

75   Uchida S, Tagami K. Soil-to-crop Transfer Factors of Radium in Japanese Agricultural Fields. 2007.

76   Van Netten C, Hoption Cann SA, Morley DR, Van Netten JP. Elemental and radioactive analysis of commercially available seaweed. *Sci Total Environ* 2000; **255**: 169–175.

77   OTA T, SANADA T, KASHIWARA Y, MORIMOTO T, SATO K. Evaluation for Committed Effective Dose Due to Dietary Foods by the Intake for Japanese Adults. *Japanese J Heal Phys* 2009; **44**: 80–88.

78   Nain M, Chauhan RP, Chakarvarti SK. Alpha radioactivity in tobacco leaves: Effect of fertilizers. *Radiat Meas* 2008; **43**. doi:10.1016/j.radmeas.2008.04.034.

79   Hei TK, Kushner S. Radiation and Asbestos Fibers: Interaction and Possible Mechanism. In: *Anticarcinogenesis and Radiation Protection*. Springer US: Boston, MA, 1987, pp 345–348.

80   Boumala D, Belafrites A, Tedjani A, Mavon C, Groetz J-E. Annual effective dose and excess life time cancer risk assessment from tobacco plants. *Perspect Sci* 2019; **12**: 100394.

81   Pacella A, Andreozzi GB, Fournier J. Detailed crystal chemistry and iron topochemistry of asbestos occurring in its natural setting: A first step to understanding its chemical reactivity. *Chem Geol* 2010; **277**: 197–206.

82   Suzuki T, Sakakibara Y, Hisanaga N, Sakai K, Yu I-J, Lim H-S *et al.* The association

among ferruginous body, uncoated fibers, asbestos and non-asbestos fibers in lung tissue in terms of length. *Ind Health* 2016; **54**: 370–376.

83   Vernon-Parry KD. Scanning electron microscopy: an introduction. *III-Vs Rev* 2000; **13**: 40–44.

84   Newbury DE, Ritchie NWM. Is scanning electron microscopy/energy dispersive X-ray spectrometry (SEM/EDS) quantitative? *Scanning* 2013; **35**: 141–168.

85   Giannuzzi LA, Stevie FA. A review of focused ion beam milling techniques for TEM specimen preparation. *Micron* 1999; **30**: 197–204.

86   Vernon-Parry K, Wright A. TEM: An introduction — part 2. *III-Vs Rev* 2001; **14**: 48–51.

87   Leake BE, Woolley AR, Arps CES, Birch WD, Gilbert MC, Grice JD *et al.* Nomenclature of Amphiboles; Report of the Subcommittee on Amphiboles of the International Mineralogical Association Commission on New Minerals and Mineral Names. *Mineral Mag* 1997; **61**: 295–310.

88   Miles KR. Grunerite in Western Australia. *Am Mineral* 1943; **28**: 25–38.

89   Klein CJ. Cummingtonite-Grunerite Series: a chemical, optical and x-ray study. *Am Mineral* 1964; **53**: 963–982.

90   Lyons PC. Significance of riebickite and ferrohastringsite in microperthite granites. *Am Mineral* 1972; **57**: 1404–1412.

91   Evans B. Reactions among sodic, calcic, and ferromagnesian amphiboles, sodic pyroxene, and deerite in high-pressure metamorphose ironstone, Siphnos, Greece. *Mineral Am Sci Geol* 1986; **7**: 18–25.

92   Ahn JH, Buseck PE. Microstructures and fiber-formation mechanisms of crocidolite asbestos. *Am Mineral* 1991; **76**: 1467–1478.

93   Hirschmann M, Evens BW, Yang H. Composition and temperature dependence of Fe-Mg ordering in cummingtonite-grunerite as determined by X-ray diffraction Mlnc. *Am Mineral* 1994; **79**: 862–877.

94   Koerten HK, Hazekamp J, Kroon M, Daems WT. Asbestos body formation and iron accumulation in mouse peritoneal granulomas after the introduction of crocidolite asbestos fibers. *Am J Pathol* 1990; **136**: 141–57.

95   Guzman G, Alcantara E, Barron V, Torrent J. Phytoavailability of phosphate adsorbed on ferrihydrite, hematite, and goethite. *Plant Soil* 1994; **159**: 219–225.

96   Wang X, Li W, Harrington R, Liu F, Parise JB, Feng X *et al.* Effect of ferrihydrite crystallite size on phosphate adsorption reactivity. *Environ Sci Technol* 2013; **47**: 10322–10331.

97   Pascolo L, Gianoncelli A, Schneider G, Salomé M, Schneider M, Calligaro C *et al.* The interaction of asbestos and iron in lung tissue revealed by synchrotron-based scanning X-ray microscopy. *Sci Rep* 2013; **3**: 1–11.

98   Hiriart E, Deepe R, Wessels A. Mesothelium and malignant mesothelioma. *J Dev Biol* 2019; **7**. doi:10.3390/jdb7020007.

99   Bardelli F, Veronesi G, Capella S, Bellis D, Charlet L, Cedola A *et al.* New insights on the biomineralisation process developing in human lungs around inhaled asbestos fibres. *Sci Rep* 2017; **7**: 1–11.

100   Thomas R. *Practical Guide to ICP-MS*. 2004 doi:10.1017/CBO9781107415324.004.

101   Thomas R. A beginner's guide to ICP-MS - Part III: The plasma source. *Spectroscopy* 2001; **16**: 26-+.

102   Thomas R. A beginner's guide to ICP-MS. *Spectroscopy* 2001; **16**: 38–42.

103   Bulska E, Wagner B. Quantitative aspects of inductively coupled plasma mass spectrometry. *Philos Trans R Soc A Math Phys Eng Sci* 2016; **374**: 20150369.

104   Yokoyama T, Makishima A, Nakamura E. Evaluation of the coprecipitation of

105 Makishima A, Nakamura E. Determination of Major/ Minor and Trace Elements in Silicate Samples by ICP-QMS and ICP-SFMS Applying Isotope Dilution-Internal Standardisation (ID-IS) and Multi-Stage Internal Standardisation. *Geostand Geoanalytical Res* 2006; **30**: 245–271.

106 Makishima A, Kitagawa H, Nakamura E. Simultaneous Determination of Cd, In, Tl and Bi by Isotope Dilution-Internal Standardisation ICP-QMS with Corrections Using Externally Measured MoO+/Mo+ Ratios. *Geostand Geoanalytical Res* 2011; **35**: 57–67.

107 McDonough WF, Sun S s. The composition of the Earth. *Chem Geol* 1995; **120**: 223–253.

108 Sajih M, Bryan ND, Livens FR, Vaughan DJ, Descostes M, Phrommavanh V *et al.* Adsorption of radium and barium on goethite and ferrihydrite: A kinetic and surface complexation modelling study. *Geochim Cosmochim Acta* 2014; **146**: 150–163.

109 Mishra V, Baranwal V, Mishra RK, Sharma S, Paul B, Pandey AC. Immunotoxicological impact and biodistribution assessment of bismuth selenide (Bi2Se3) nanoparticles following intratracheal instillation in mice. *Sci Rep* 2017; **7**: 1–12.

110 Towe KM. Phosphorus and the Ferritin Iron Core: Function-Balanced Biomineralization. Orig. Evol. Mod. Asp. Biominer. Plants Anim. 1989; : 265–272.

111 Dyer JA, Trivedi P, Sanders SJ, Scrivner NC, Sparks DL. Lead sorption onto ferrihydrite. 3. Multistage contacting. *Environ Sci Technol* 2003; **37**: 923–930.

112 Ames LL, McGarrah JE, Walker BA, Salter PF. Uranium and radium sorption on amorphous ferric oxyhydroxide. *Chem Geol* 1983; **40**: 135–148.

113 Jutz G, Van Rijn P, Santos Miranda B, Böker A. Ferritin: A versatile building block for bionanotechnology. *Chem Rev* 2015; **115**: 1653–1701.

114 Granier T, Comberton G, Gallois B, Langlois D'Estaintot B, Dautant A, Crichton RR *et al.* Evidence of new cadmium binding sites in recombinant horse L-chain ferritin by anomalous fourier difference map calculation. *Proteins Struct Funct Genet* 1998; **31**: 477–485.

115 Anderson, H L, Arthur, S E, Brady, P V, Cygan, R T, Nagy, K L, and Westrich HR. Irreversible sorption of contaminants during ferrihydrite contamination. 1999.

116 Silvera SANN, Rohan TE. Trace elements and cancer risk: a review of the epidemiologic evidence. *Cancer Causes Control* 2007; **18**: 7–27.

117 Field RW, Withers BL. Occupational and Environmental Causes of Lung Cancer. *Clin Chest Med* 2012; **33**: 681–703.

118 Lee JC, Son YO, Pratheeshkumar P, Shi X. Oxidative stress and metal carcinogenesis. *Free Radic Biol Med* 2012; **53**: 742–757.

119 Ireland TR. *Ion Microprobe Mass Spectrometry : Techniques and Applications in Cosmochemistry, Geochemistry, and Geochronology*. 1995.

120 van der Heide P. *Secondary Ion Mass Spectrometry*. John Wiley & Sons, Inc.: Hoboken, NJ, USA, 2014 doi:10.1002/9781118916780.

121 Schwertmann U., Cornell RM. Iron oxides in the laboratory: preparation and characterization. *John Wiley Sons* 2008.https://www.wiley.com/en-us/Iron+Oxides+in+the+Laboratory%3A+Preparation+and+Characterization%2C+2nd%2C+Completely+Revised+and+Enlarged+Edition-p-9783527613229.

122 Cudennec Y, Lecerf A. The transformation of ferrihydrite into goethite or hematite, revisited. *J Solid State Chem* 2006; **179**: 716–722.

123 Das S, Hendry MJ, Essilfie-Dughan J. Transformation of Two-Line Ferrihydrite to

Goethite and Hematite as a Function of pH and Temperature. *Environ Sci Technol* 2011; **45**: 268–275.

124   Magill J. *Radioactivity Radionuclides Radiation*. Springer-Verlag: Berlin/Heidelberg, 2005 doi:10.1007/b138236.

125   D'Angelis CA, Coalson JJ, Ryan RM. Structure of the Respiratory System. In: *Pediatric Critical Care*. Elsevier, 2011, pp 490–498.

126   National Council on Radiation Protection and Measurements. Alpha-emitting particles in lungs : recommendations of the National Council on Radiation Protection and Measurements. *NCRP Rep* 1975; : v, 28 p.

127   Brudin LH, Rhodes CG, Valind SO, Wollmer P, Hughes JMB. Regional lung density and blood volume in nonsmoking and smoking subjects measured by PET. *J Appl Physiol* 1987; **63**: 1324–1334.

128   Tsapaki V, Damilakis J, Paulo G, Schegerer AA, Repussard J, Jaschke W *et al.* The 2007 Recommendations of the International Commission on Radiological Protection. ICRP publication 103. *Ann ICRP* 2007; **37**: 1–332.

129   Roato I. Bone metastases: When and how lung cancer interacts with bone. *World J Clin Oncol* 2014; **5**: 149–155.

130   Brodowicz T, O'byrne K, Manegold C. Bone matters in lung cancer. *Ann Oncol* 2012; **23**: 2215–2222.

Appendix
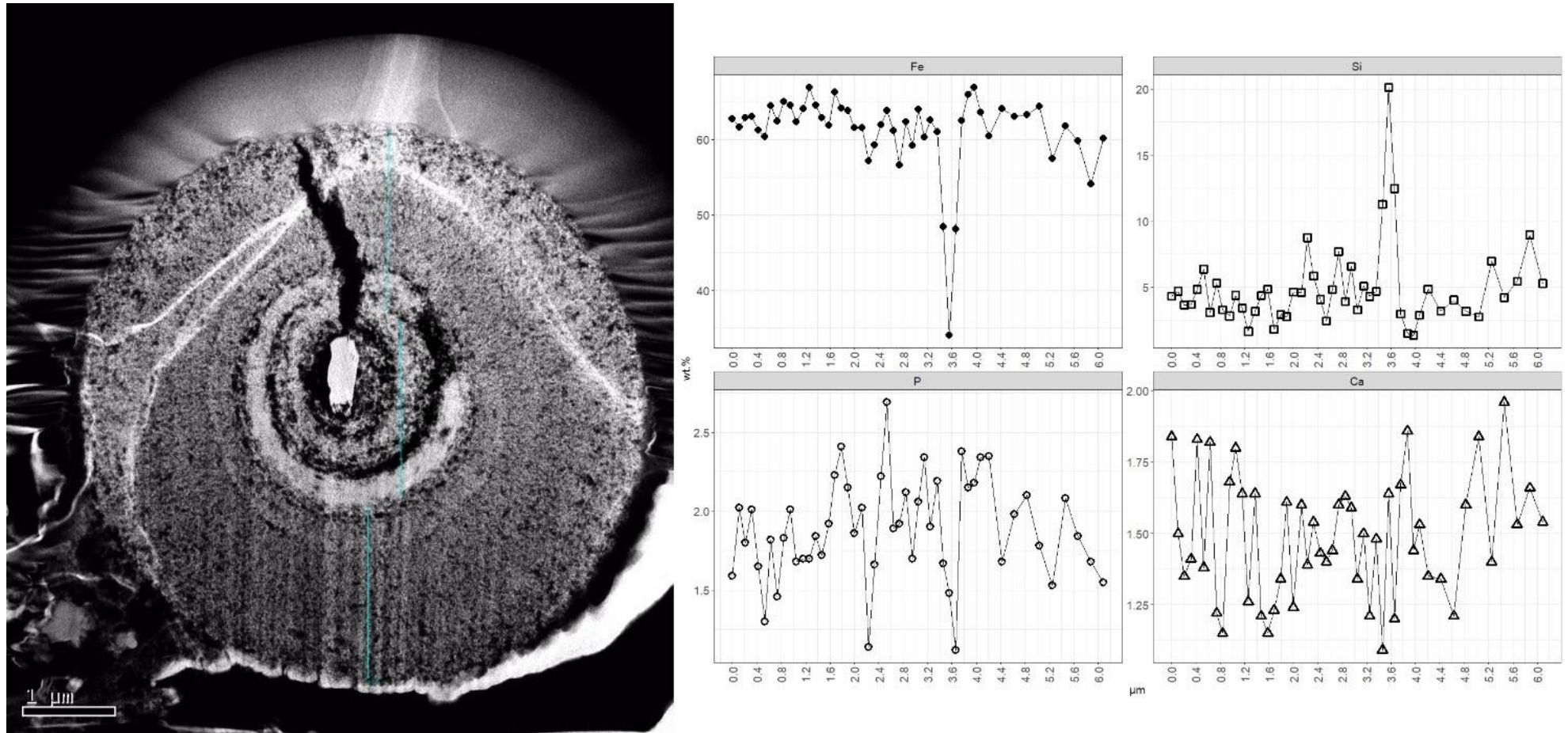
Figure A1: Internal morphology of patient E AFB1 and line profile of Fe, Si, P, and Ca.
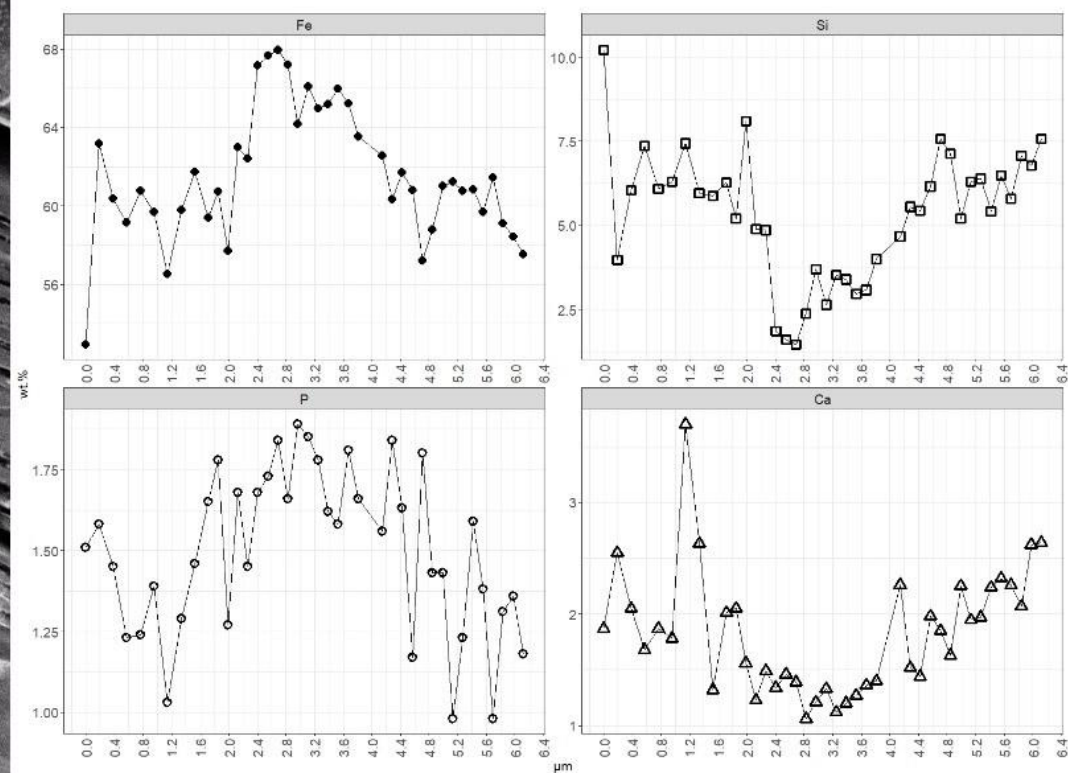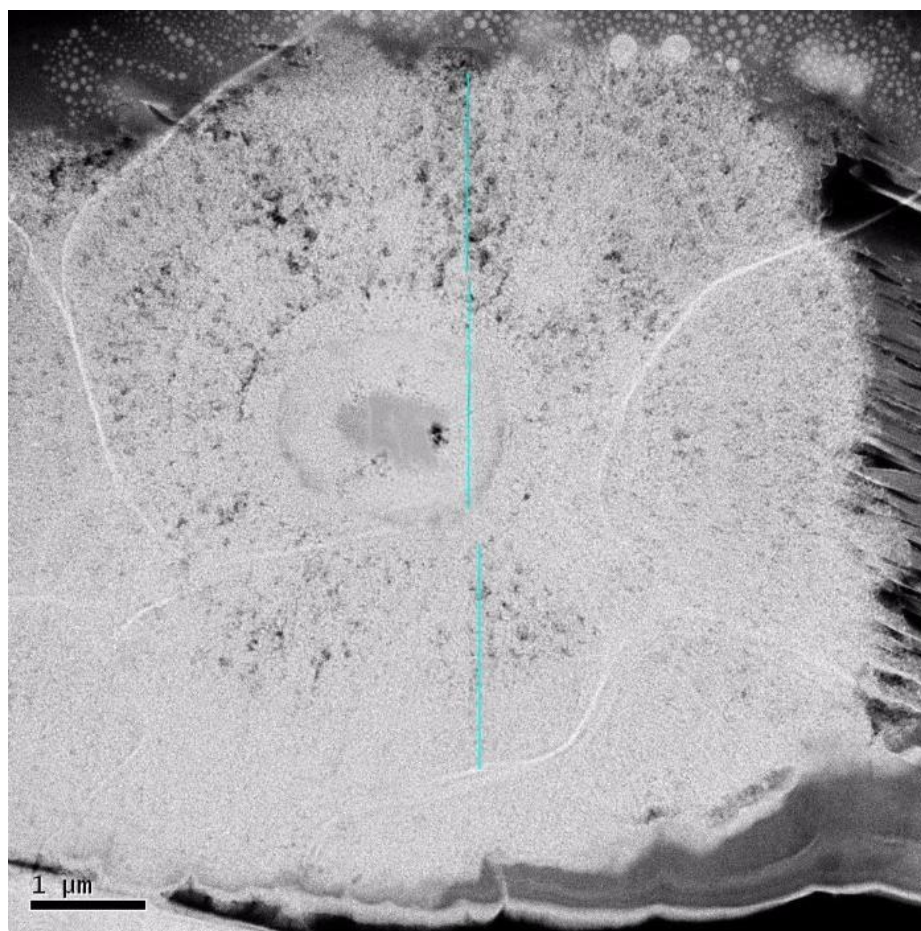
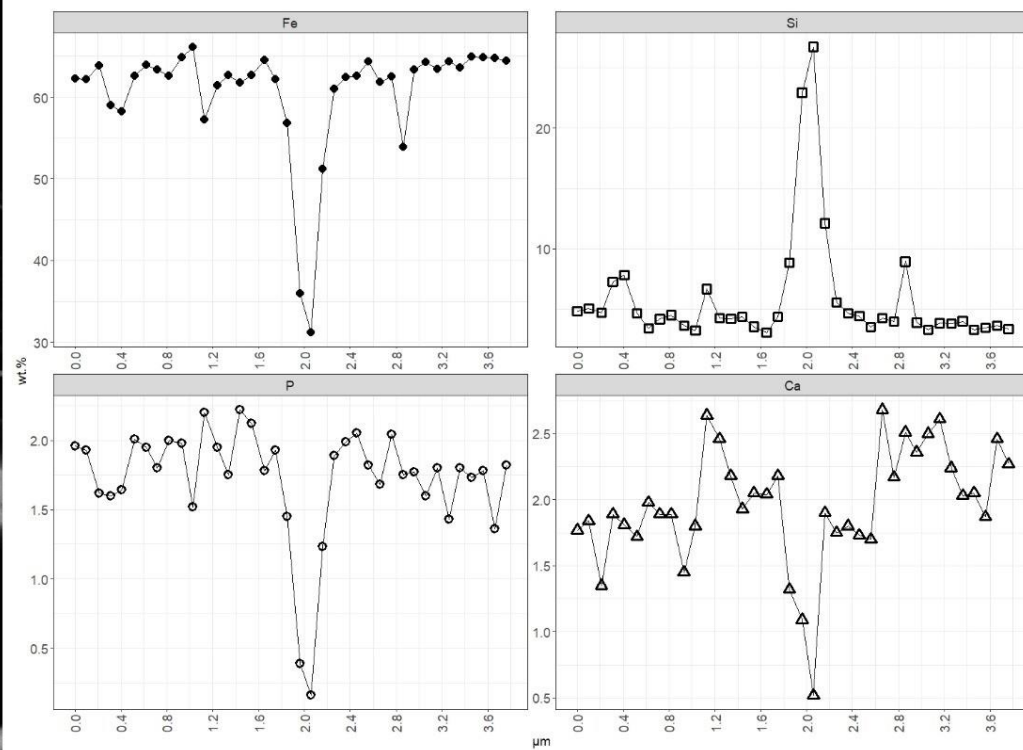Figure A2: Internal morphology of patient E AFB2 and line profile of Fe, Si, P, and Ca.
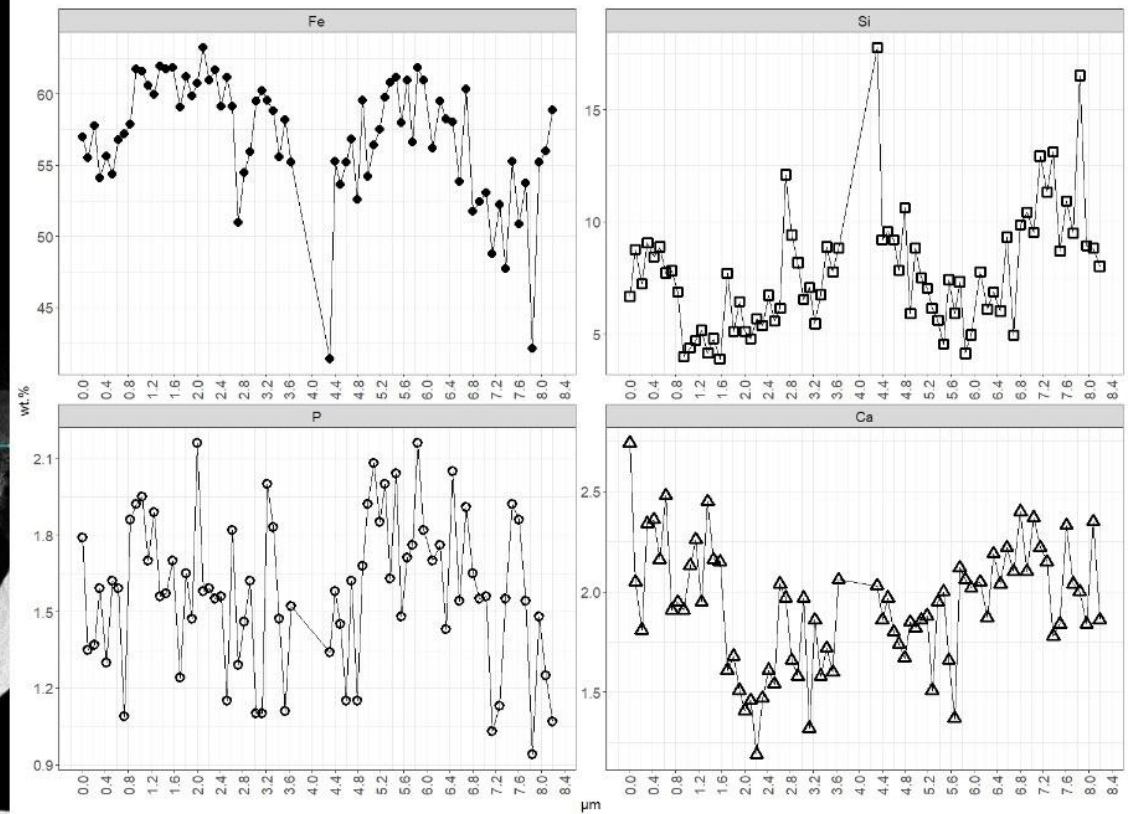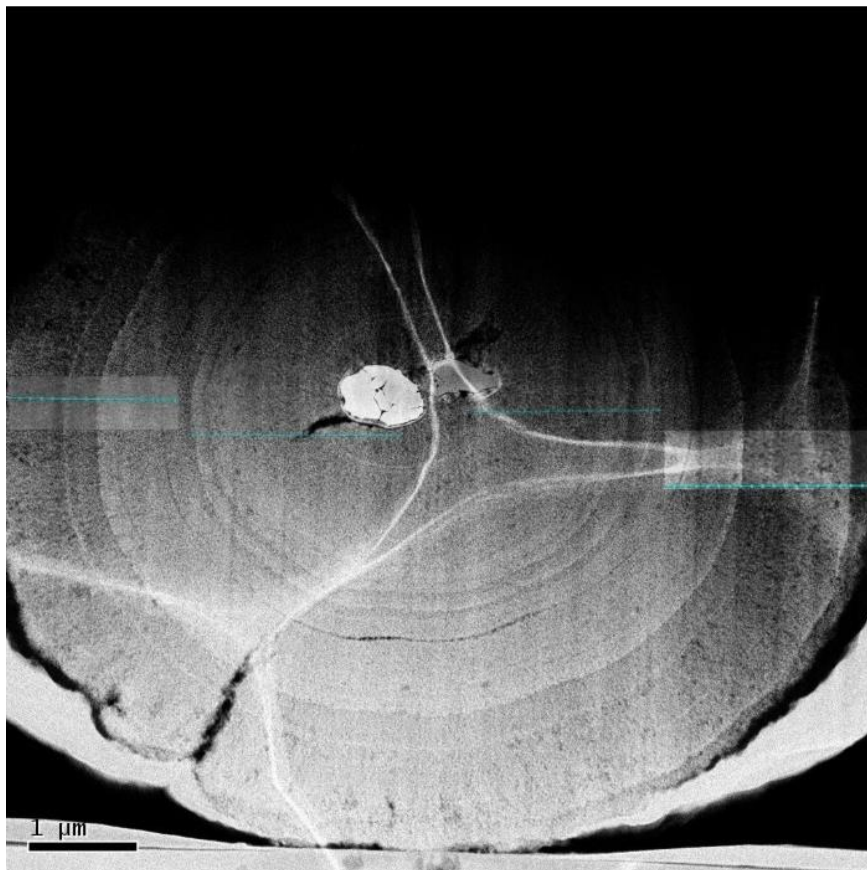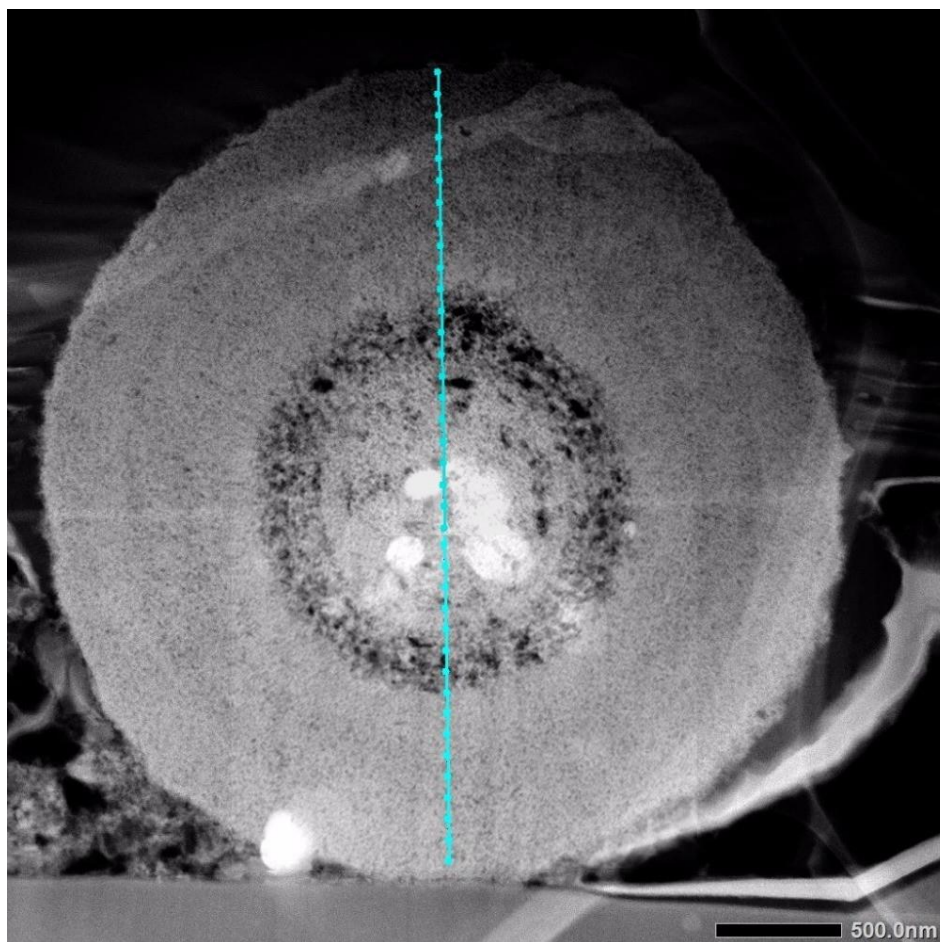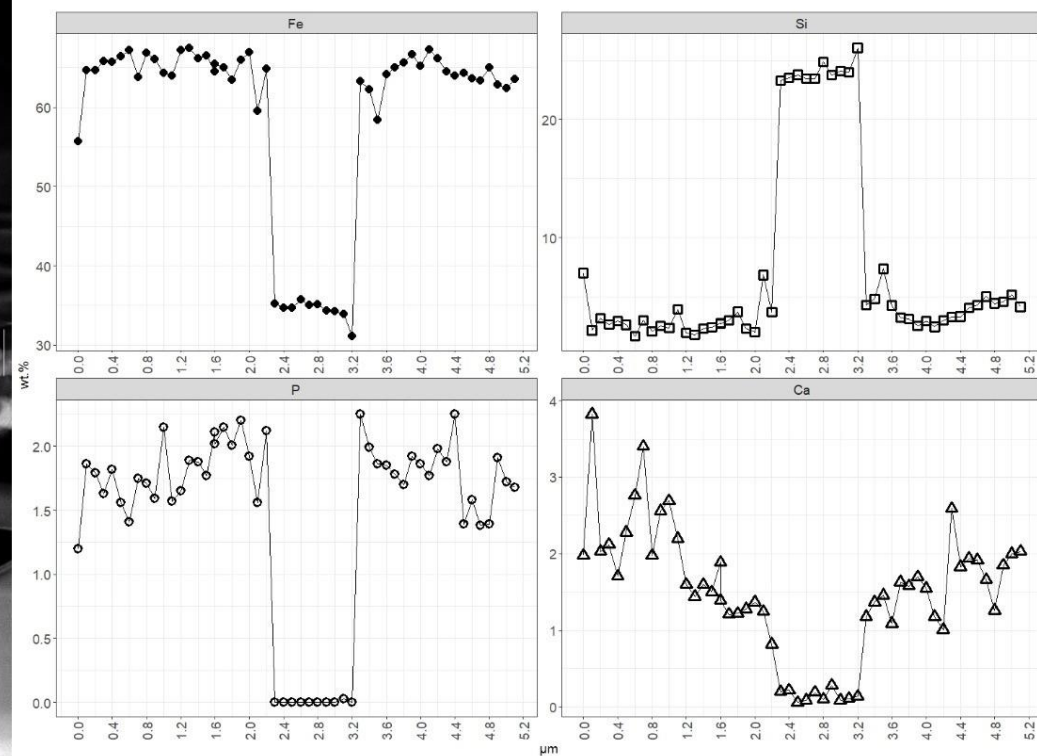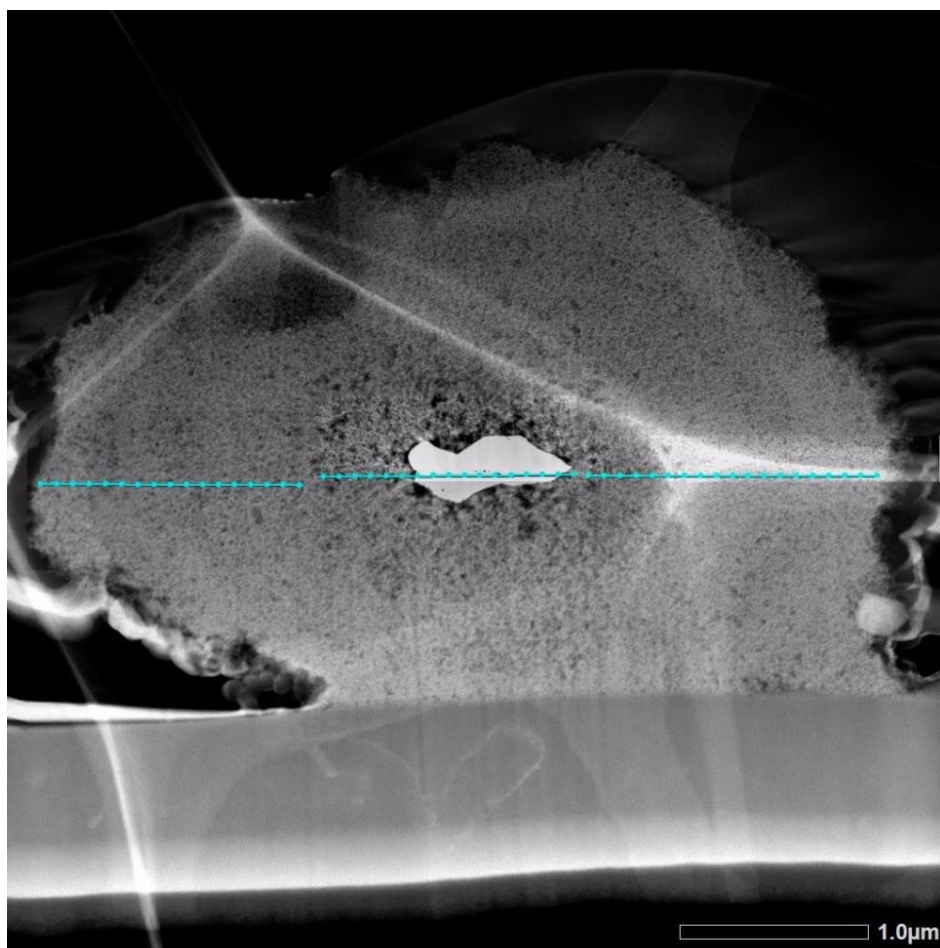
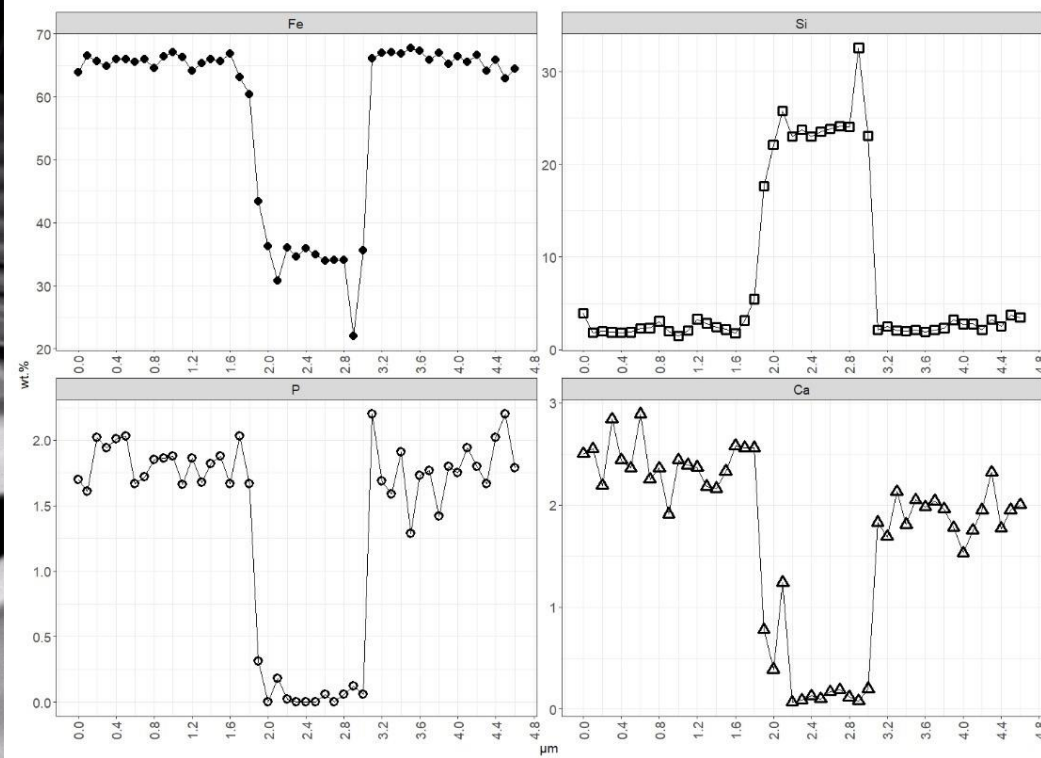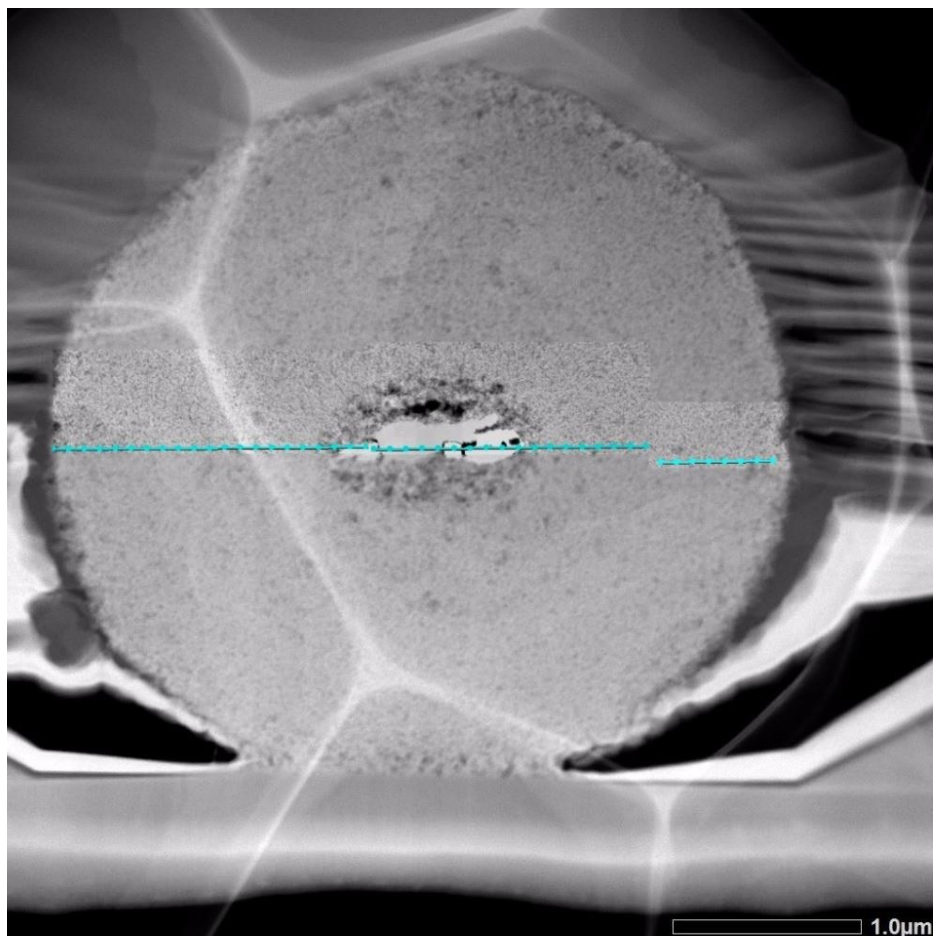Figure A3: Internal morphology of patient E AFB3 and line profile of Fe, Si, P, and Ca.
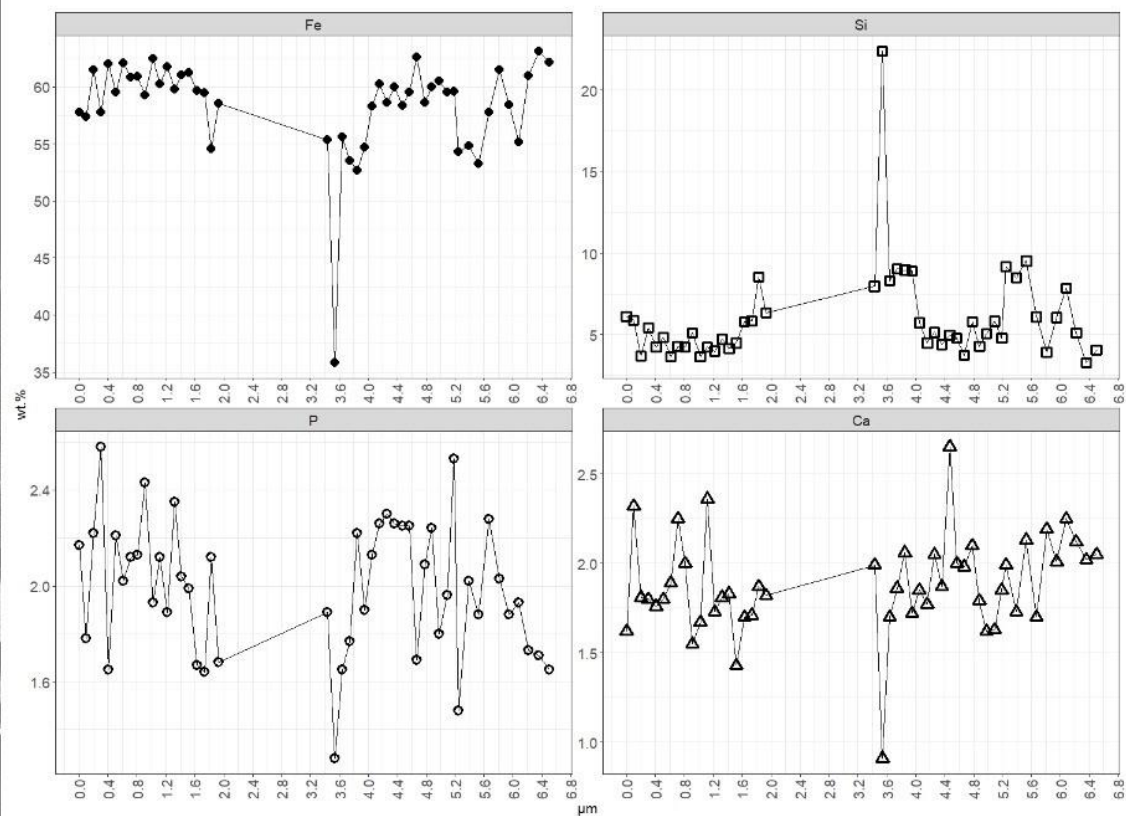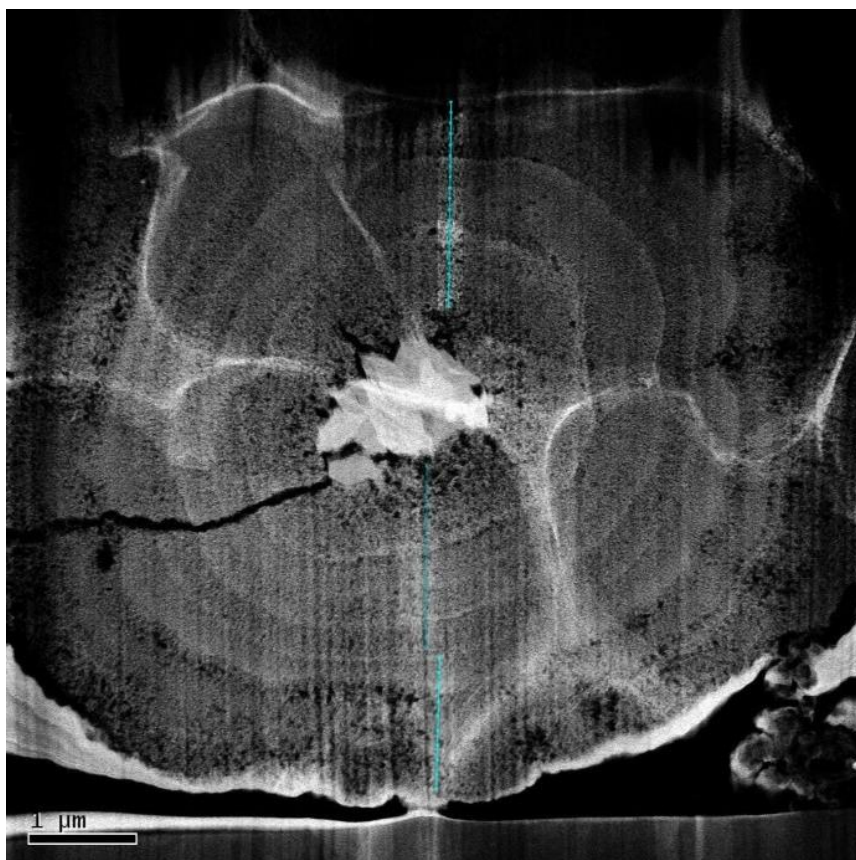
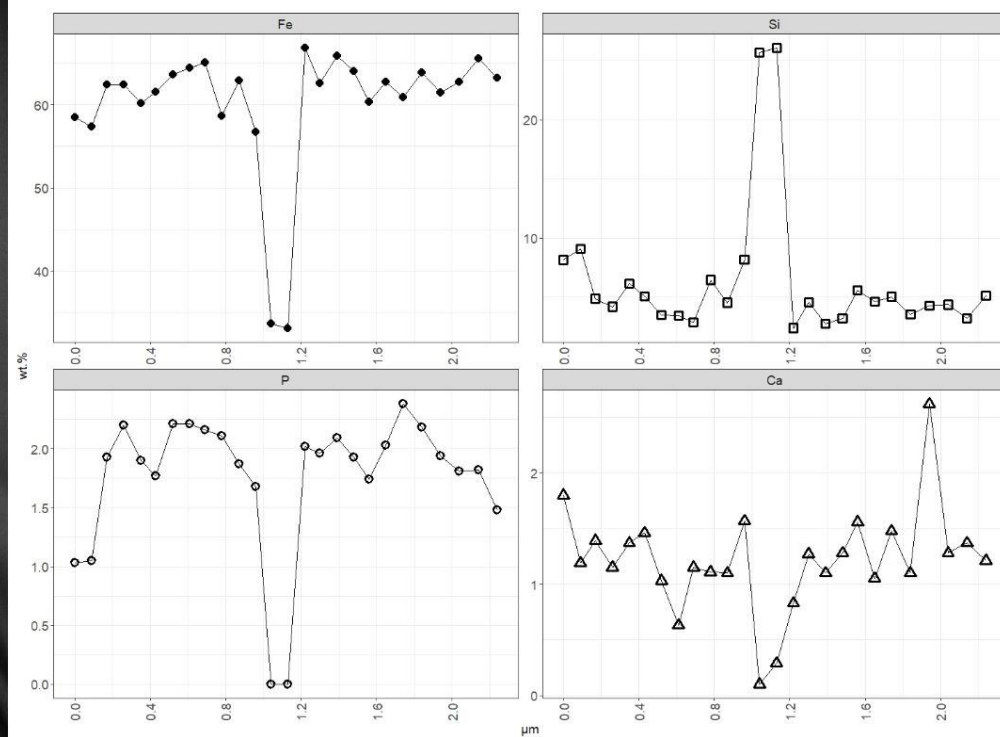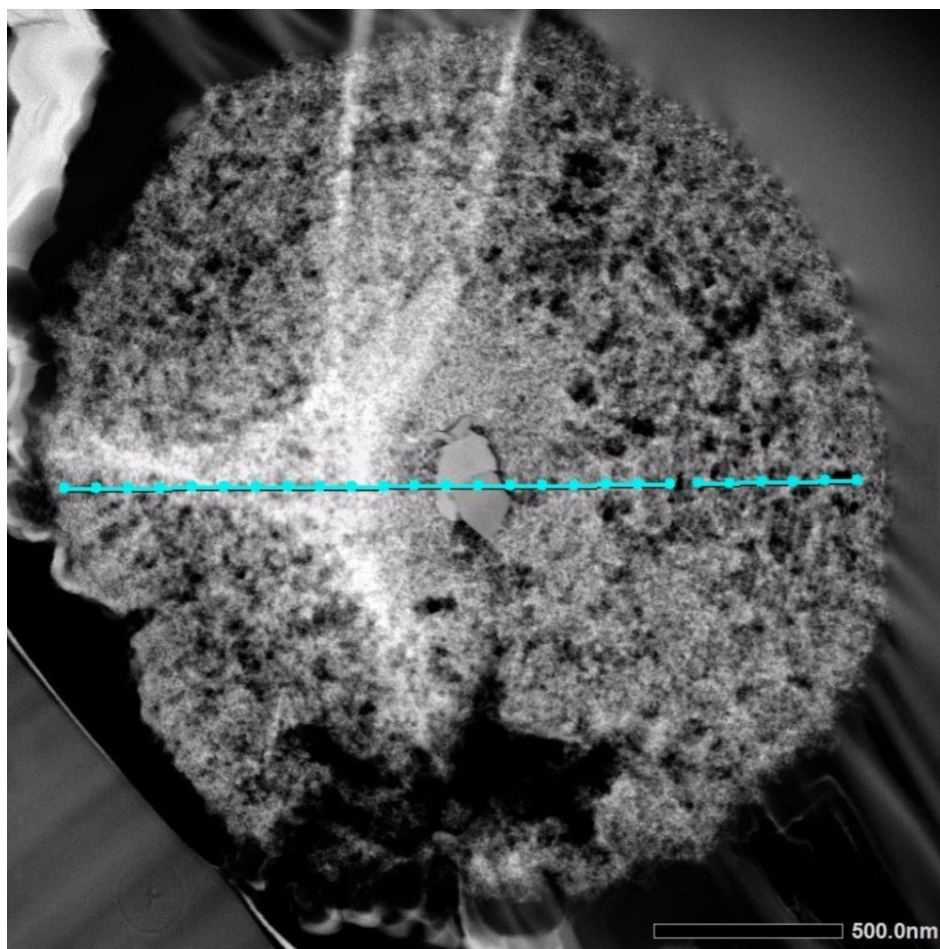Figure A4: Internal morphology of patient E AFB4 and line profile of Fe, Si, P, and Ca.
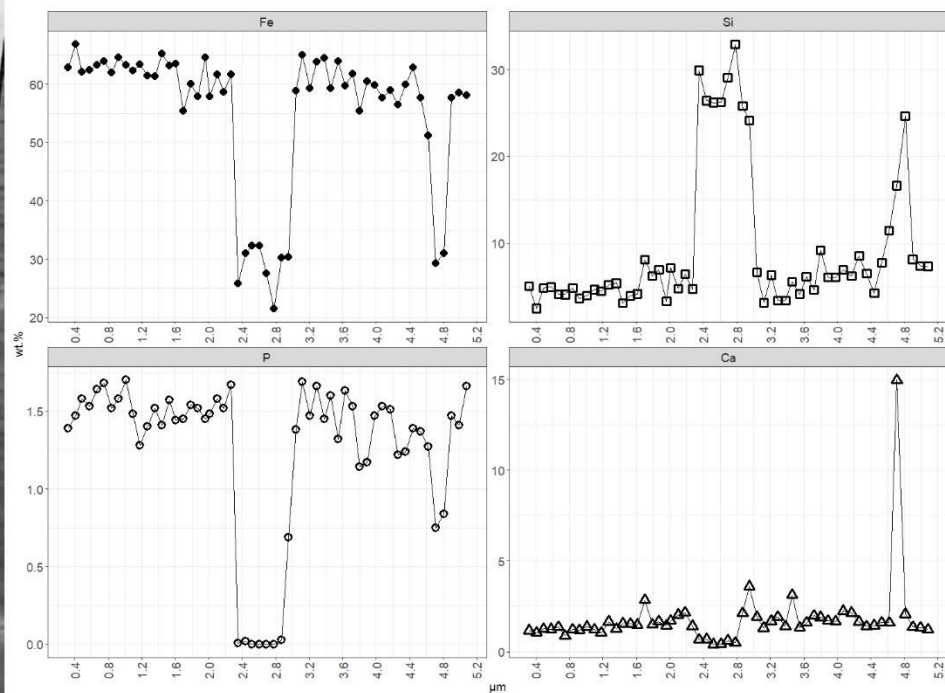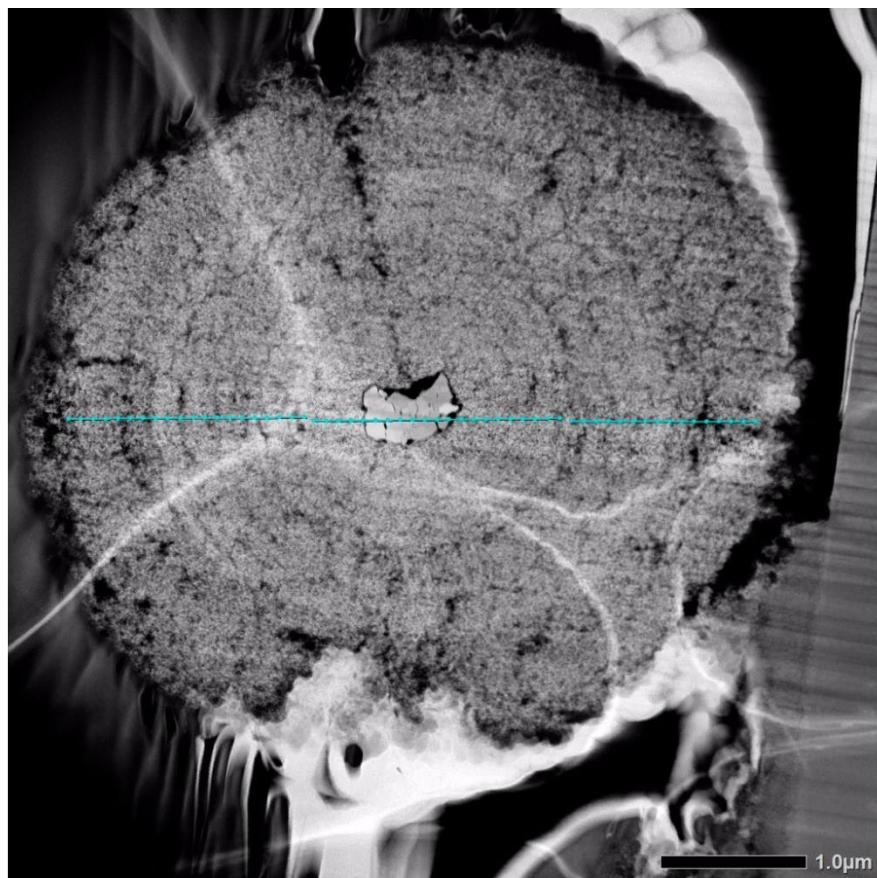
Figure A5: Internal morphology of patient K AFB1 and line profile of Fe, Si, P, and Ca.
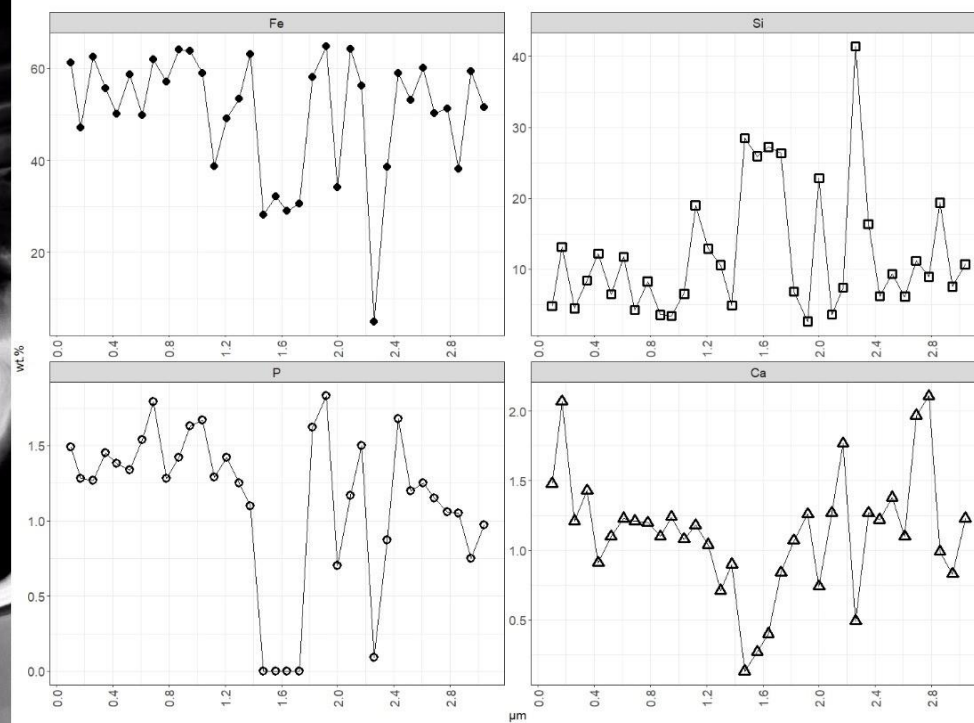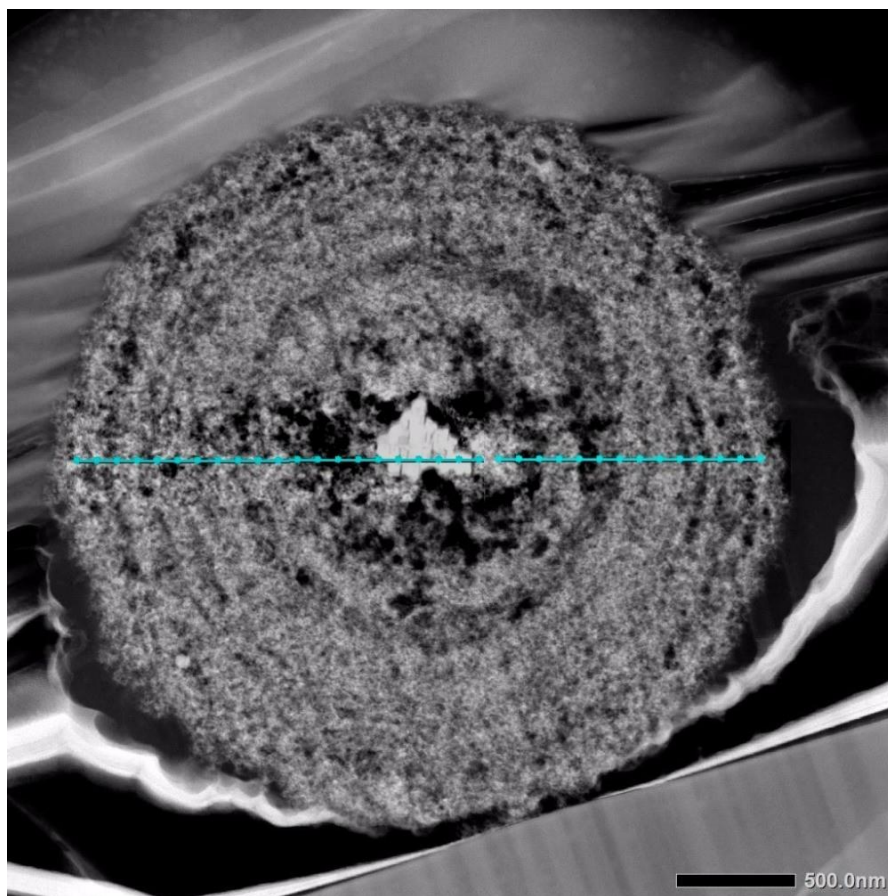
Figure A6: Internal morphology of patient K AFB2 and line profile of Fe, Si, P, and Ca.
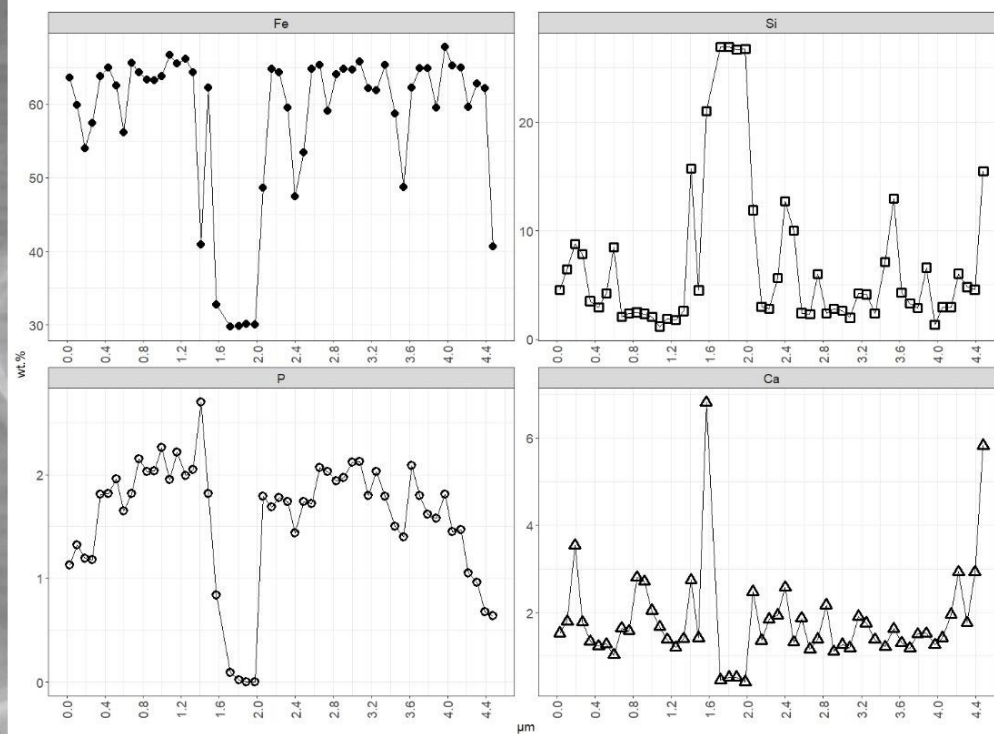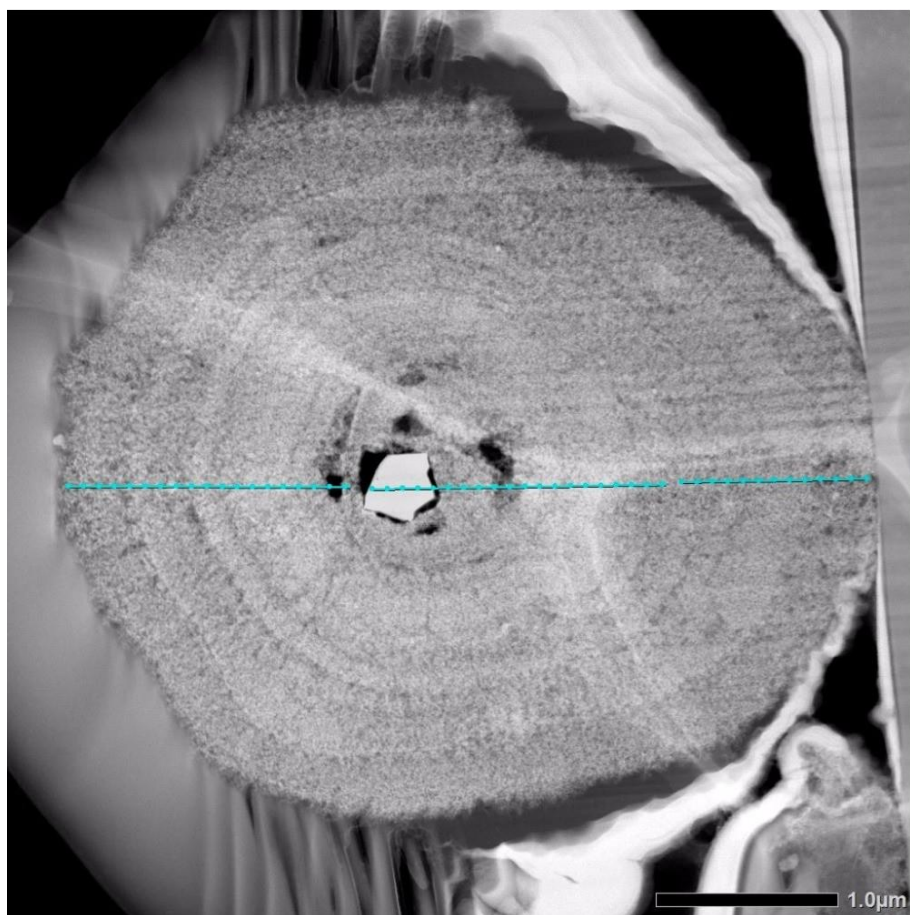
Figure A7: Internal morphology of patient K AFB3 and line profile of Fe, Si, P, and Ca.
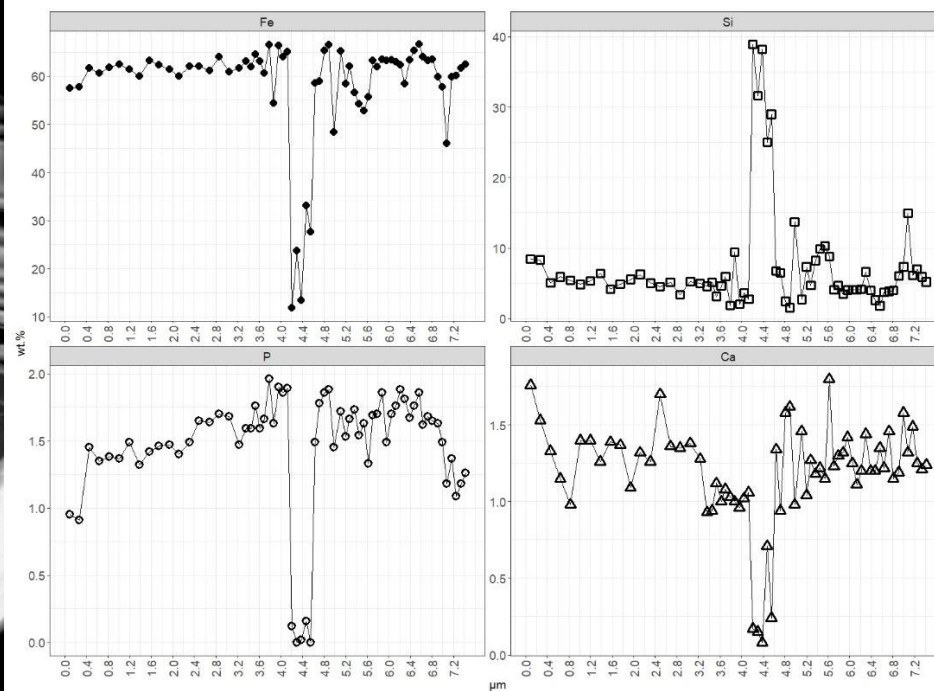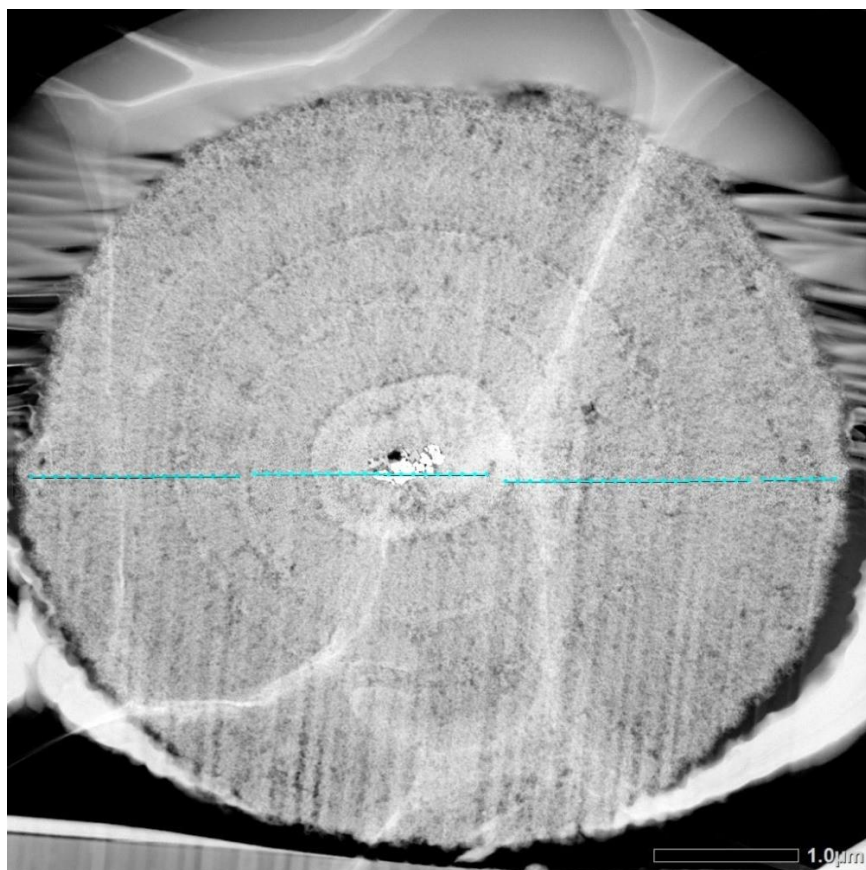
Figure A8: Internal morphology of patient K AFB4 and line profile of Fe, Si, P, and Ca.
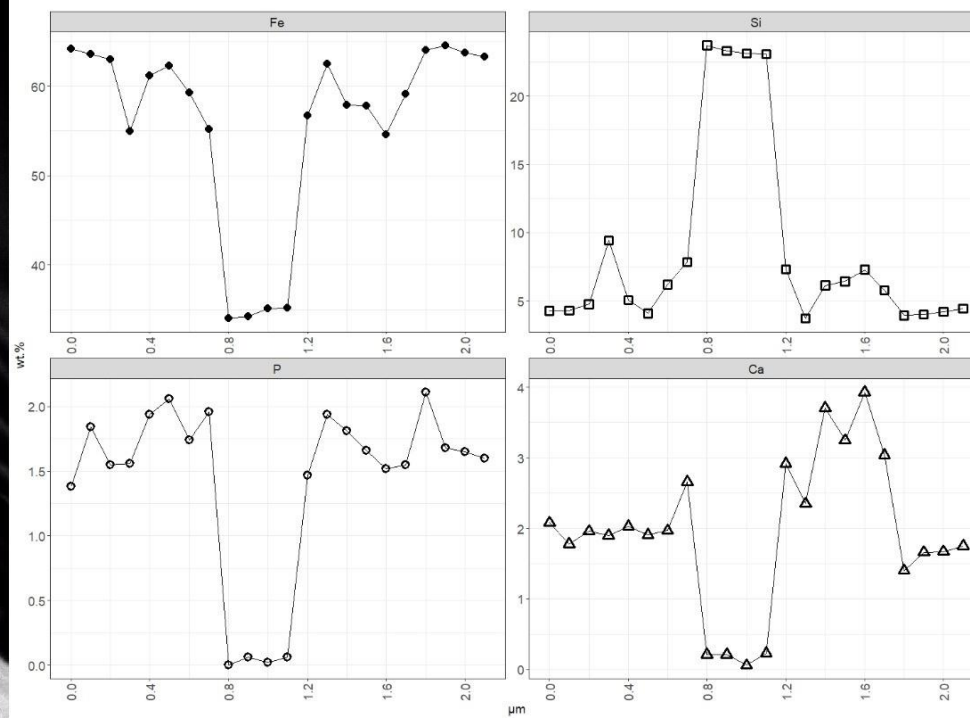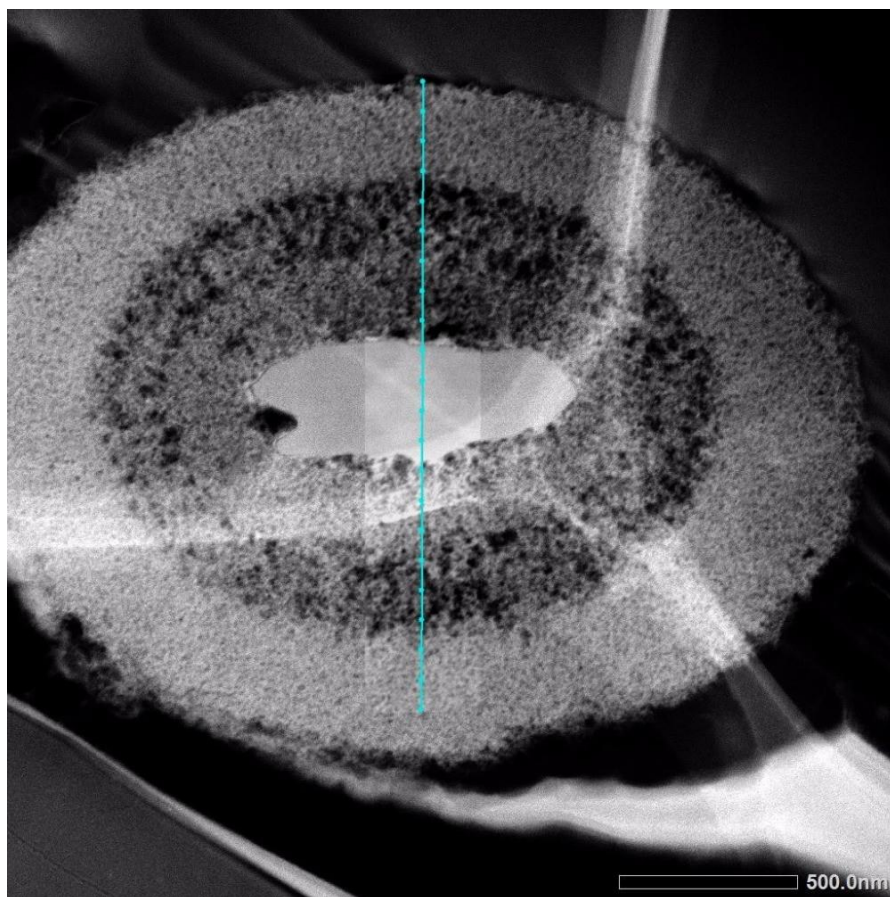
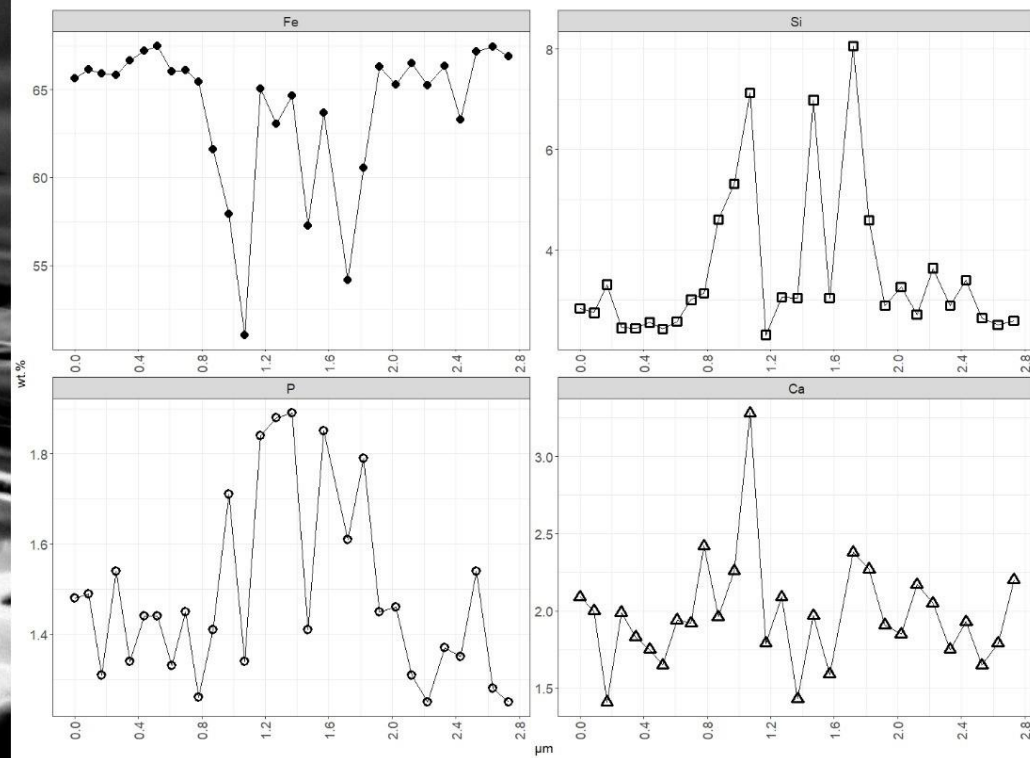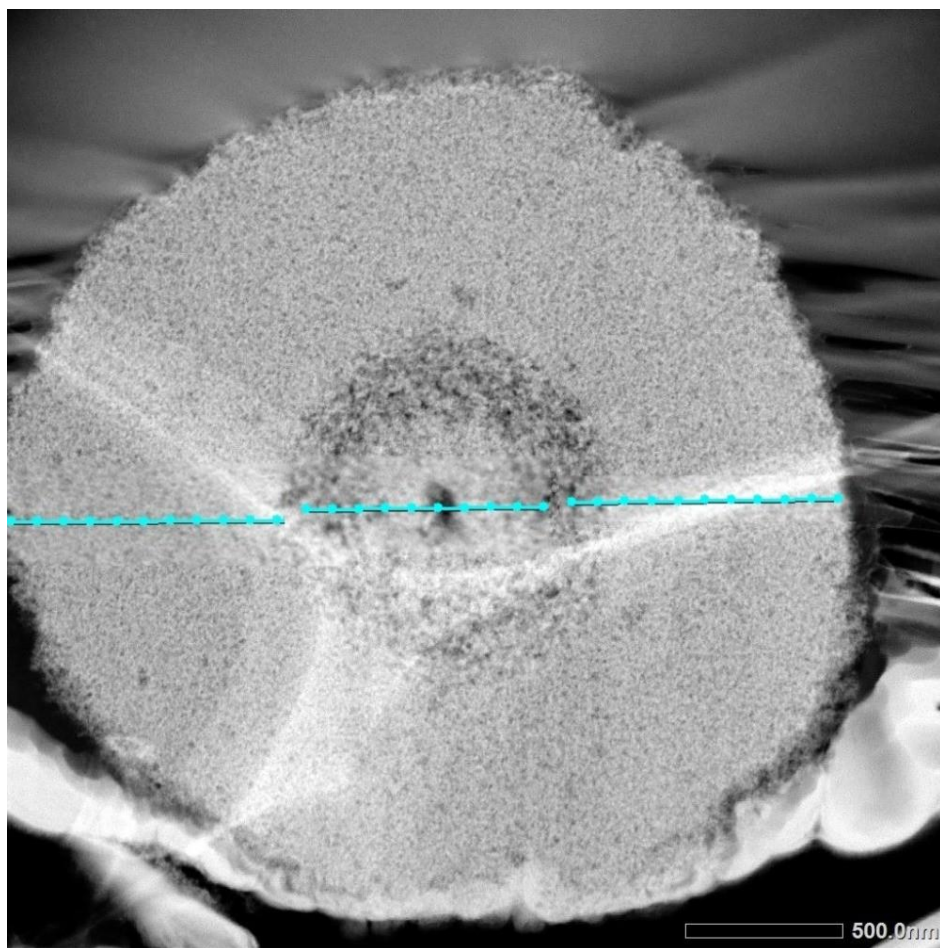Figure A9: Internal morphology of patient H AFB1 and line profile of Fe, Si, P, and Ca.

Figure A10: Internal morphology of patient H AFB2 and line profile of Fe, Si, P, and Ca.

Figure A11: Internal morphology of patient H AFB3 and line profile of Fe, Si, P, and Ca.

Figure A12: Internal morphology of patient H AFB4 and line profile of Fe, Si, P, and Ca.

Figure A13: Internal morphology of patient A AFB1 and line profile of Fe, Si, P, and Ca.

Figure A14: Internal morphology of patient A AFB2 and line profile of Fe, Si, P, and Ca
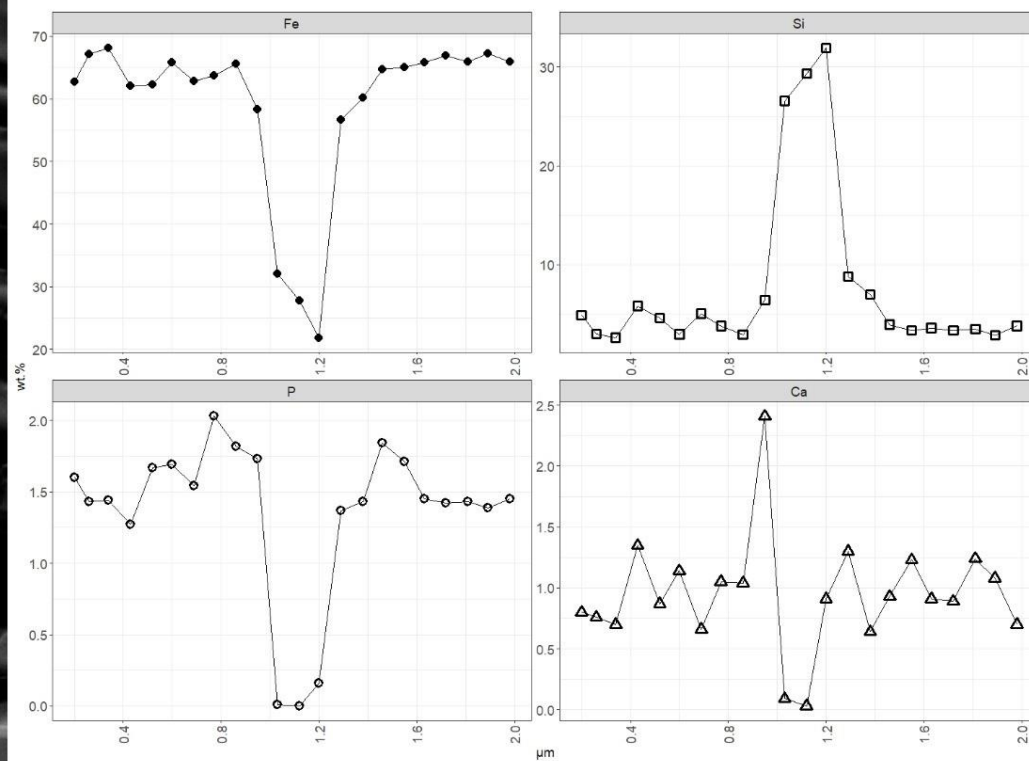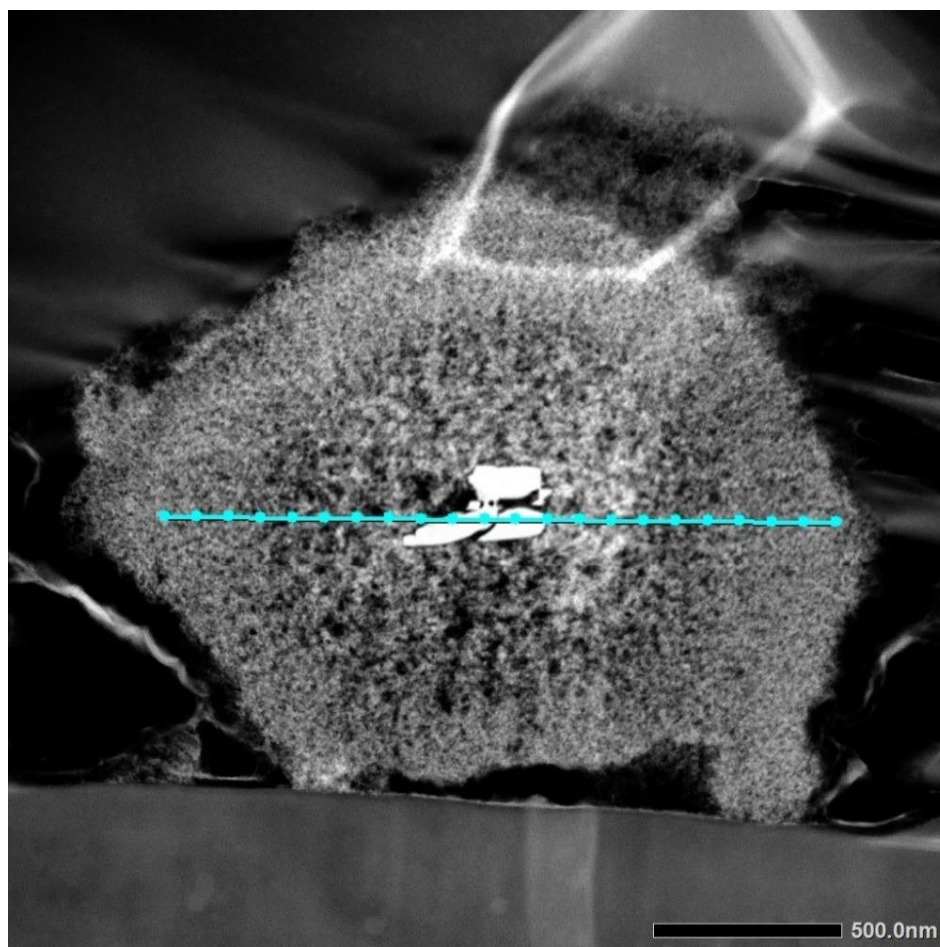
Figure A15: Internal morphology of patient A AFB3 and line profile of Fe, Si, P, and Ca.